ISTANBUL TECHNICAL UNIVERSITY ★ GRADUATE SCHOOL

CALCULATING RADAR RANGE PROFILE BY TIME DOMAIN PROCESSING WITH PHYSICAL OPTICS

M.Sc. THESIS

Ece YAZAREL

Electronics and Communication Engineering

Telecommunication Engineering Programme

JULY 2024

ISTANBUL TECHNICAL UNIVERSITY ★ GRADUATE SCHOOL

CALCULATING RADAR RANGE PROFILE BY TIME DOMAIN PROCESSING WITH PHYSICAL OPTICS

M.Sc. THESIS

Ece YAZAREL
(504201345)

Electronics and Communication Engineering

Telecommunication Engineering Programme

Thesis Advisor: Prof. Dr. Selçuk PAKER

JULY 2024

İSTANBUL TEKNİK ÜNİVERSİTESİ ★ LİSANSÜSTÜ EĞİTİM ENSTİTÜSÜ

FİZİKSEL OPTİK YÖNTEMİYLE ZAMAN DOMENİNDE SİNYAL İŞLEME KULLANILARAK RADAR MENZİL PROFİLİNİN HESAPLANMASI

YÜKSEK LİSANS TEZİ

Ece YAZAREL
(504201345)

Elektronik ve Haberleşme Mühendisliği Anabilim Dalı

Telekomünikasyon Mühendisliği Programı

Tez Danışmanı: Prof. Dr. Selçuk PAKER

TEMMUZ 2024

Ece YAZAREL, a M.Sc. student of ITU Graduate School student ID 504201345 successfully defended the thesis entitled "CALCULATING RADAR RANGE PROFILE BY TIME DOMAIN PROCESSING WITH PHYSICAL OPTICS", which she prepared after fulfilling the requirements specified in the associated legislations, before the jury whose signatures are below.

Thesis Advisor :	**Prof. Dr. Selçuk PAKER** Istanbul Technical University	....
Jury Members :	**Prof. Dr. Funda AKLEMAN YAPAR** Istanbul Technical University	....
	Prof. Dr. Çağatay ULUIŞIK Atlas University	....

Date of Submission : **24 May 2024**
Date of Defense : **11 July 2024**

To my spouse,

FOREWORD

It is with great gratitude and a sense of accomplishment that I present this thesis, which delves into the complexities of Radar Range Profile calculation through Time Domain Processing and the Physical Optics (PO) method. The path to completing this work has been marked by both challenges and moments of profound learning, as I pursued my passion for electromagnetic engineering and embraced the opportunity to innovate in this fascinating field. The development of this thesis was far from a solitary effort. I owe my deepest thanks to my academic advisor, Prof. Dr. Selçuk Paker, whose expertise and mentorship provided invaluable guidance throughout this journey. His encouragement and insights have not only shaped the direction of this research but also played a pivotal role in my growth as a researcher. To my family and friends, I extend heartfelt thanks for their unwavering support and patience, which provided me with strength and motivation during both the highs and the challenges of this endeavor. A special and heartfelt thank you goes to my husband, who has always trusted and supported me, not only during the thesis stage but throughout every aspect of my life. His unwavering belief in my abilities, encouragement, and love have been my constant source of strength and inspiration. I also wish to express my deepest gratitude to my aunt Ayşe, who has been a guiding light in my life since I was a child. My journey into academia and my passion for problem-solving began with her guidance as she introduced me to the beauty of mathematics by solving special problems together. Her encouragement and wisdom sparked my curiosity and laid the foundation for my academic pursuits, which ultimately led to this moment. This thesis represents more than an academic milestone; it is a testament to perseverance, curiosity, and the pursuit of understanding. My hope is that the insights and methodologies developed here will contribute to the field of electromagnetic engineering, advancing our ability to design better radar systems and improve stealth technology. Looking ahead, I am excited by the possibilities that this work opens for future exploration in radar technology and related fields. May the findings presented in these pages serve as a stepping stone for future innovations and deepen our understanding of Radar Cross Section (RCS) calculations and their applications.

July 2024 Ece YAZAREL

TABLE OF CONTENTS

ABBREVIATIONS

FEM	: Finite Element Method
PO	: Physical Optics
GO	: Geometric Optics
GTD	: Geometric Theory of Diffraction
HH	: Horizontal-Horizontal
HRRP	: High Resolution Range Profile
HV	: Horizontal-Vertical
LFM	: Linear Frequency Modulation
MoM	: Method of Moment
PEC	: Perfectly Electrical Conductor
PTD	: Physical Theory of Diffraction
PRF	: Pulse Repetition Frequency
RCS	: Radar Cross Section
ROC	: Receiver Operating Characteristics
SAR	: Synthetic Aperture Radar
SBR	: Shooting and Bouncing Ray
SNR	: Signal to Noise Ratio
VH	: Vertical-Horizontal
VV	: Vertical-Vertical

SYMBOLS

$\boldsymbol{\varepsilon_r}$	: Relative Permittivity, Dielectric Constant
$\boldsymbol{\mu_r}$	: Relative Magnetic Permeability
$\boldsymbol{\sigma}$	: Radar Cross Section Area
E_s	: Scattered Electric Field Vector
E_i	: Incident Electric Field Vector
$\boldsymbol{R}$	: Distance Between the Target and Observation Point
$\boldsymbol{E_{i\theta}}$	: Incident Electric Field's Theta Component
$\boldsymbol{E_{i\phi}}$	: Incident Electric Field's Phi Component
$\boldsymbol{E_{s\theta}}$	: Scattered Electric Field's Theta Component
$\boldsymbol{E_{s\phi}}$	: Scattered Electric Field's Phi Component
J_S	: Surface Current Density Vector
$\boldsymbol{\hat{n}}$	: Unit Surface Normal
H_i	: Incident Magnetic Field Vector
$\boldsymbol{\vec{r}_n}$	: Position Vector of the nth Triangle Surface Corner
$\boldsymbol{\hat{a}_x, \hat{a}_y, \hat{a}_z}$	: Cartesian Coordinate System Unit Vectors
$\boldsymbol{\hat{a}_r, \hat{a}_\theta, \hat{a}_\phi}$	: Spherical Coordinate System Unit Vectors
$\boldsymbol{x_n, y_n, z_n}$	: Cartesian Coordinates of the nth Triangle Surface Corner
$\boldsymbol{l_1, l_2, l_3}$	: Edge Vectors of the Triangle Surface
$\boldsymbol{\theta_i, \phi_i}$	: Incidence Angles of the Plane Wave
$\boldsymbol{\vec{k}_i}$	: Propagation Vector of the Plane Wave
$\boldsymbol{k}$	: Wave Number
$\boldsymbol{u_i, v_i, w_i}$	: Direction Cosines of the Incident Wave
$\boldsymbol{\lambda}$	: Wavelength
$\boldsymbol{x', y', z'}$	: Cartesian Coordinates of the Source Point
$\boldsymbol{x, y, z}$	: Cartesian Coordinates of the Observation Point
$\boldsymbol{\vec{r}'}$	: Position Vector of the Source Point
A_s	: Magnetic Vector Potential
M_s	: Electric Vector Potential
$\boldsymbol{\eta_0}$	: Intrinsic Impedance
$\boldsymbol{J_x, J_y, J_z}$	: Magnitudes of Cartesian Coordinates of Surface Current
$\boldsymbol{\vec{k}}$	: Wave Vector
$\boldsymbol{u, v, w}$	: Direction Cosines of the Wave Vector
$\boldsymbol{x'', y'', z''}$	: Local Coordinate Axes
$\boldsymbol{\alpha}$	: Rotation angle of x and y axis
$\boldsymbol{\beta}$	: Rotation angle of x and z axis
$\boldsymbol{\vec{D}'_\alpha}$	: Rotation Matrix for α angle
$\boldsymbol{\vec{D}'_\beta}$	: Rotation Matrix for β angle

$\boldsymbol{E^+}$	: Forward Propagating Wave
$\boldsymbol{E^-}$	: Backward Propagating Wave
$\boldsymbol{n}$	: Refractive Index
$\boldsymbol{S}$	: Scattering Matrix
$\boldsymbol{T}$	: Transmission Coefficient
$\boldsymbol{P_d}$	: Probability of Detection
$\boldsymbol{P_{fa}}$	: Probability of False Alarm
$\boldsymbol{R_{MAX}}$	: Maximum Unambiguous Range
$\boldsymbol{c}$	: Speed of Light
$\boldsymbol{\Delta R}$	: Range Resolution
$\boldsymbol{B}$	: Pulse Bandwidth
$\boldsymbol{\tau}$	: Pulse Width
$\boldsymbol{F_S}$	: Sampling Rate
$\boldsymbol{N}$	: Number of Pulses
$\boldsymbol{k}$	: Boltzmann Constant
$\boldsymbol{P_t}$	: Peak Transmit Power
$\boldsymbol{P_n}$	: Peak Noise Power at the Receiver
$\boldsymbol{G_t}$	: Transmitter Gain
$\boldsymbol{G_r}$	: Receiver Gain

LIST OF TABLES

Page

LIST OF FIGURES

Page

CALCULATING RADAR RANGE PROFILE BY TIME DOMAIN PROCESSING WITH PHYSICAL OPTICS

SUMMARY

This thesis provides an in-depth exploration of the concept of Radar Cross Section (RCS) analysis. RCS is a critical metric in radar technology, used to measure the detectability of a target by quantifying the electromagnetic energy scattered by the target and reflected back to the radar system. This study examines the theoretical foundations, computational methods, and practical applications of RCS, offering an approach that aims to bridge the gap between theoretical knowledge and real-world implementations. The thesis contributes significantly to areas such as radar system design, radar signal processing, and stealth technology evaluation.

The study begins with the theoretical foundations of the RCS concept. RCS is influenced by numerous factors, including the size, shape, material properties, and orientation of the object, as well as the radar operating frequency. The scattering mechanisms that affect RCS are categorized into specular reflection, diffuse scattering, edge diffraction, and multiple scattering. Each mechanism impacts RCS differently depending on the geometry and electromagnetic properties of the target. Additionally, the behavior of RCS is described across three main regions: the Rayleigh region (where the object's size is much smaller than the radar wavelength), the Resonance region (where the object's size is comparable to the radar wavelength), and the Optical region (where the object's size is much larger than the radar wavelength). These classifications provide a fundamental framework for understanding how the interaction between geometry and radar frequency affects the visibility of a target.

The second part of the thesis focuses on computational methods used for RCS analysis. These methods are divided into two main categories: high-frequency and low-frequency techniques. High-frequency techniques include Physical Optics (PO), Geometric Optics (GO), the Geometric Theory of Diffraction (GTD), and the Shooting and Bouncing Rays (SBR) method. These techniques are based on optical approximations and are computationally efficient for modeling large targets. However, they are limited in accurately modeling diffraction and multiple scattering effects. On the other hand, low-frequency techniques, such as the Method of Moments (MoM) and the Finite Element Method (FEM), provide accurate full-wave solutions for small targets or resonant cases but come with high computational costs for large targets. The choice of method depends on factors such as the target's size, radar frequency, and the desired level of accuracy.

To improve the accuracy of RCS computations, this thesis introduces two algorithms: a mesh refinement algorithm and a shadowing algorithm. The mesh refinement algorithm ensures that triangular surfaces in 3D models meet specific size constraints

based on the radar wavelength, enhancing the accuracy of RCS predictions for targets with complex geometries. In regions with high curvature or intricate details, surfaces are iteratively subdivided to provide a more detailed representation. The shadowing algorithm accurately identifies and models the shadowed regions of the target, which do not contribute to radar returns. By combining these two algorithms, the thesis provides a more accurate and reliable framework for RCS computations, particularly for targets with complex geometries.

One of the key contributions of this thesis is the transition from traditional frequency-domain analysis to time-domain simulations, offering a different perspective for analyzing target-radar interactions. Most conventional methods assume continuous wave (CW) radar operations, which do not accurately reflect the pulse-based structure of modern radar systems. To address this limitation, this study integrates physical optics principles with time-domain simulations. This approach enables more realistic modeling of radar pulse behavior. By storing the reflectivity contributions of illuminated mesh elements in detail, the interaction between radar pulses and the target can be analyzed dynamically and spatially. This transition significantly enhances the ability to simulate real-time radar operations, accounting for target movement and temporal variations in radar returns.

The thesis further strengthens this framework through advanced signal processing techniques. Matched filtering maximizes the signal-to-noise ratio (SNR), facilitating the detection of weak targets and improving range resolution. Range normalization compensates for signal attenuation over distance, ensuring consistent detection sensitivity across different ranges. Coherent integration accumulates signal energy across multiple radar pulses, enabling the detection of weaker targets. These techniques allow for the generation of high-resolution range profiles (HRRPs), which provide detailed information about the physical dimensions and reflective properties of targets by isolating the strongest reflections within a predefined range window.

The practical applicability of the proposed methodologies has been tested through simulations of different targets. First, a PEC missile target was analyzed at operating frequencies of 2 GHz and 4 GHz. The RCS results were validated against those obtained from the commercial FEKO software, demonstrating a high level of accuracy. The missile's structural features, scattering behavior, and high-resolution range profile were examined from multiple perspectives, and the proposed approach achieved a target dimension estimation with an accuracy of 0.24 meters.

Additionally, the F-22 aircraft was also analyzed as part of the validation process. RCS results were compared with FEKO simulations, showing excellent agreement and verifying the accuracy of the proposed techniques. The HRRP analysis accurately estimated the dimensions and range of the F-22, demonstrating the applicability of the framework to complex geometries. Signal processing steps, such as matched filtering, range normalization, and coherent integration, were consistently applied across all targets, ensuring reliable differentiation between target reflections and noise.

Lastly, the Chengdu J-20 aircraft, with its larger dimensions and complex geometry, was analyzed at 4 GHz. The RCS results obtained for this aircraft were consistent with FEKO simulations, further validating the robustness of the proposed methodologies. This case study highlights the framework's ability to handle large-scale targets and intricate geometries, as well as its effectiveness in extracting detailed range profiles of the aircraft.

The thesis concludes by emphasizing the contributions of these methodologies to RCS analysis and radar signal processing. The integration of mesh refinement and shadowing algorithms with time-domain simulations addresses significant challenges in modeling complex geometries and real-time radar interactions. The proposed techniques have a wide range of applications, including radar system design, stealth technology evaluation, and electromagnetic wave analysis. By combining theoretical principles with computational innovations, this thesis establishes a strong foundation for future research and practical advancements in radar technology.

FİZİKSEL OPTİK YÖNTEMİYLE ZAMAN DOMENİNDE SİNYAL İŞLEME KULLANILARAK RADAR MENZİL PROFİLİNİN HESAPLANMASI

ÖZET

Bu tez, Radar Kesit Alanı (RCS) analizi kavramına derinlemesine bir bakış sunmaktadır. RCS, radar teknolojisinde bir hedefin radarla tespit edilebilirliğini ölçmek için kullanılan kritik bir metriktir. Temel olarak, RCS bir hedef tarafından saçılan elektromanyetik enerjinin radar sistemine geri yansıyan miktarını ifade eder. Bu çalışmada, RCS'nin teorik temelleri, hesaplama yöntemleri ve pratik uygulamaları incelenmiş; teorik bilgiler ile gerçek dünya uygulamaları arasındaki boşluğu doldurmayı amaçlayan bir yaklaşım sunulmuştur. Tez, radar sistem tasarımı, radar sinyal işleme ve gizlilik teknolojilerinin değerlendirilmesi gibi önemli alanlarda katkılar sağlamaktadır.

Çalışma, RCS kavramının teorik temelleriyle başlamaktadır. RCS; bir nesnenin boyutu, şekli, malzeme özellikleri, radar dalgalarına göre yönelimi ve radarın çalışma frekansı gibi birçok faktörden etkilenir. RCS'nin oluşumunda etkili olan saçılma mekanizmaları, speküler yansıma, difüz saçılma, kenar kırınımı ve çoklu saçılma olarak kategorize edilmiştir. Her bir mekanizma, hedefin geometrisine ve elektromanyetik özelliklerine bağlı olarak farklı şekillerde RCS'yi etkiler. Ayrıca, RCS'nin davranışı, üç ana bölgeye ayrılarak açıklanmıştır: Rayleigh bölgesi (nesnenin boyutunun radar dalga boyundan çok daha küçük olduğu durum), Rezonans bölgesi (nesnenin boyutunun radar dalga boyuna yakın olduğu durum) ve Optik bölge (nesnenin boyutunun radar dalga boyundan çok daha büyük olduğu durum). Bu sınıflandırmalar, bir hedefin geometrisi ve radar frekansı arasındaki etkileşimin radar görünürlüğünü nasıl etkilediğini anlamak için temel bir çerçeve sağlar.

Tezin ikinci kısmı, RCS analizi için kullanılan hesaplama yöntemlerine odaklanmaktadır. Hesaplama yöntemleri, yüksek frekanslı ve düşük frekanslı teknikler olarak iki ana kategoriye ayrılmıştır. Yüksek frekanslı teknikler, Fiziksel Optik (PO), Geometrik Optik (GO), Geometrik Kırınım Teorisi (GTD) ve Çarpan ve Sıçrayan Işınlar (SBR) yöntemlerini içerir. Bu teknikler, büyük hedefleri modellemek için optik yaklaşımlara dayanır ve hesaplama açısından oldukça verimlidir. Ancak, kırınım ve çoklu saçılma gibi etkileri doğru bir şekilde modelleme konusunda sınırlıdırlar. Buna karşılık, Düşük Frekanslı Teknikler, Momentler Yöntemi (MoM) ve Sonlu Elemanlar Yöntemi (FEM) gibi yöntemleri içerir. Bu teknikler, küçük hedefler veya rezonans durumlar için tam dalga çözümleri sağlayarak yüksek doğruluk sunar, ancak büyük hedefler için hesaplama maliyetleri oldukça yüksektir. Hangi yöntemin kullanılacağına, hedefin boyutu, radar frekansı ve istenen doğruluk düzeyi gibi faktörler doğrultusunda karar verilir.

Bu tezde, hesaplamaların doğruluğunu iyileştirmek amacıyla RCS hesaplamasına ek olarak iki adet algoritma geliştirilmiştir: ağ (mesh) iyileştirme algoritması ve gölgeleme algoritması. Ağ iyileştirme algoritması, üç boyutlu modellerdeki üçgen yüzeylerin, radar dalga boyuna dayalı olarak belirli boyut sınırlamalarına uygun hale getirilmesini sağlar. Bu yöntem, karmaşık geometrilere sahip hedeflerin RCS tahmin doğruluğunu artırır. Yüksek eğrilik veya karmaşık detayların olduğu bölgelerde, daha detaylı bir temsil sağlamak için yüzeyler iteratif olarak bölünür. Gölgeleme algoritması ise hedefin gölgeli bölgelerini doğru bir şekilde tanımlayarak ve modelleyerek, radar dönüşlerine katkıda bulunmayan bu bölgeleri hesaba katar. Bu iki algoritmanın kombinasyonu, karmaşık geometrilere sahip hedefler için RCS hesaplama sürecini daha doğru ve güvenilir hale getirir.

Bu tezin önemli katkılarından biri, geleneksel frekans alanı analizlerinden zaman alanı simülasyonlarına geçerek hedef ile radar etkileşimini analiz etmek için farklı bir bakış açısı sunmasıdır. Çoğu geleneksel yöntem, sürekli dalga (CW) radar operasyonlarını varsayarak çalışır ve bu durum modern radar sistemlerinin darbe tabanlı yapısını doğru bir şekilde yansıtmaz. Bu sorunu ele almak için tezde, fiziksel optik prensipleri zaman alanı simülasyonlarıyla birleştirilmiştir. Bu yöntem, radar darbelerinin davranışını daha gerçekçi bir şekilde modellemeyi mümkün kılar. Aydınlanan ağ elemanlarının yansıtıcılık katkıları detaylı bir şekilde depolanarak, hedef ile radar darbeleri arasındaki etkileşim dinamik ve mekânsal olarak çözülmüş bir şekilde analiz edilmiştir. Bu geçiş, hedef hareketi ve radar geri dönüşlerindeki zamana bağlı değişiklikler gibi gerçek zamanlı radar operasyonlarını simüle etme kabiliyetini önemli ölçüde artırır.

Tez, bu çerçeveyi ileri sinyal işleme teknikleriyle daha da güçlendirmektedir. Eşleşmiş filtreleme, zayıf hedeflerin tespit edilmesini kolaylaştırarak sinyal-gürültü oranını (SNR) en üst düzeye çıkarır ve menzil çözünürlüğünü artırır. Menzil normalizasyonu, radar sinyalinin mesafe boyunca zayıflamasını telafi ederek, değişen menzil aralıklarında eşit algılama hassasiyeti sağlar. Koherent entegrasyon, birden fazla radar darbesi boyunca sinyal enerjisini biriktirerek, daha zayıf hedeflerin tespit edilmesine olanak tanır. Bu teknikler, yüksek çözünürlüklü menzil profilleri (HRRP'ler) oluşturulmasını sağlar. HRRP'ler, önceden tanımlanmış bir menzil penceresi içindeki en güçlü yansımaları izole ederek, hedeflerin fiziksel boyutları ve yansıtıcı özellikleri hakkında ayrıntılı bilgiler sunar.

Önerilen yöntemlerin pratik uygulanabilirliği, farklı hedeflerin simülasyonlarıyla test edilmiştir. İlk olarak, bir PEC füze hedefi, 2 GHz ve 4 GHz çalışma frekanslarında analiz edilmiştir. Bu analizlerde elde edilen RCS sonuçları, ticari FEKO yazılımından elde edilen sonuçlarla karşılaştırılmış ve yüksek bir doğruluk düzeyi sergilenmiştir. Füzenin yapısal özellikleri, saçılma davranışı ve yüksek çözünürlüklü menzil profili çeşitli açılardan incelenmiş, bu yaklaşımla hedefin fiziksel boyutlarının 0.24 metre hassasiyetle tahmin edilebildiği görülmüştür.

Ek olarak, daha büyük boyutlara ve karmaşık bir geometriye sahip olan F-22 uçağı ele alınmıştır. Uçak için elde edilen RCS sonuçları, FEKO simülasyonlarıyla karşılaştırılmış ve önerilen yöntemlerin doğruluğu test edilmiştir. HRRP analizi, uçağın boyutlarını ve menzilini doğru bir şekilde tahmin ederek, bu çerçevenin karmaşık geometrilere ve büyük ölçekli hedeflere uygulanabilirliğini göstermiştir.

Eşleşmiş filtreleme, menzil normalizasyonu ve koherent entegrasyon gibi sinyal işleme adımları her iki hedefte tutarlı bir şekilde uygulanarak, hedef yansımaları ile gürültü arasında güvenilir bir ayrım yapılmasını sağlamıştır.

Son olarak, daha karmaşık bir geometriye sahip olan Chengdu J-20 uçağı, 4 GHz çalışma frekansında analiz edilmiştir. Bu analizde elde edilen RCS sonuçları, FEKO simülasyonları ile tutarlılık göstermiş ve önerilen yöntemlerin sağlamlığı doğrulanmıştır. Chengdu J-20'nin detaylı menzil profilleri çıkarılmış, önerilen yaklaşımın büyük ölçekli hedefler üzerindeki uygulanabilirliği bir kez daha gösterilmiştir.

Tez, bu yöntemlerin RCS analizi ve radar sinyal işleme alanlarına katkılarını vurgulayarak sonuçlanmaktadır. Ağ iyileştirme ve gölgeleme algoritmalarının zaman alanı simülasyonlarıyla entegrasyonu, karmaşık geometrilerin ve gerçek zamanlı radar etkileşimlerinin modellenmesinde önemli zorlukları ele alır. Önerilen teknikler, radar sistem tasarımı, gizlilik teknolojisi değerlendirmesi ve elektromanyetik dalga analizi gibi çeşitli alanlarda geniş bir uygulama yelpazesine sahiptir. Bu tez, teorik prensipleri hesaplama yenilikleriyle birleştirerek, radar teknolojisi alanında gelecekteki araştırmalara ve pratik ilerlemelere sağlam bir temel oluşturmuştur.

1. INTRODUCTION

The concept of Radar Cross Section (RCS) is a cornerstone in the field of electromagnetic engineering, with profound implications in both military and civilian sectors. It quantifies how objects reflect radar signals, playing a critical role in stealth technology and in the detection and tracking of objects in aerospace and other domains. Traditional RCS calculations rely heavily on frequency-domain analysis; however, these methods often fall short in capturing transient phenomena and wideband responses. This limitation has driven a need for more dynamic approaches, and integrating time-domain processing with the Physical Optics (PO) method has emerged as a promising solution. This thesis presents a comprehensive exploration of Radar Range Profile calculations using this innovative methodology [1]

Chapter 2 provides a theoretical foundation, outlining the fundamentals of RCS, including its historical context, basic principles, and its vital role in electromagnetic applications. This chapter emphasizes the importance of accurate RCS calculations and discusses the limitations of traditional methods, highlighting the need for more versatile computational frameworks. [2]

In Chapter 3, the focus shifts to the application of the Physical Optics method, particularly its implementation on triangular facets. This chapter addresses the complexities of modeling and analyzing electromagnetic wave interactions with intricate geometries, including the development of mesh refinement algorithms. Additionally, it explores the challenges of shadowing in RCS calculations and demonstrates how refined meshes improve precision and computational efficiency, forming a robust basis for further analyses.

Chapter 4 builds on this framework by investigating the interaction of electromagnetic waves with various materials. This chapter delves into the calculation of reflection and transmission coefficients for dielectric materials, offering critical insights into how material properties influence wave behavior. These discussions extend the applicability of PO, allowing for more realistic and nuanced RCS models.

The methodologies discussed reach their culmination in Chapter 5, where the core computational techniques are explored in detail. This chapter introduces the time-domain signal processing techniques employed in this thesis, demonstrating their integration with PO to account for range-dependent losses and transient effects. The development and implementation of algorithms such as matched filtering and time-varying gain corrections are highlighted, showcasing their role in enhancing the accuracy of radar simulations.

Chapter 6 validates the methodologies through practical applications, including simulations involving real-world targets such as missiles and advanced aircraft. This chapter not only highlights the robustness of the proposed approach but also compares its effectiveness with traditional methods, demonstrating clear advantages in accuracy and computational efficiency. The findings open new avenues for research and practical applications in both military and civilian radar technologies.

This thesis aims to make a significant contribution to the field of electromagnetic engineering by advancing the methodologies used for Radar Range Profile calculations. By combining Physical Optics with time-domain techniques, this study addresses existing limitations, improves accuracy, and provides a versatile framework for future innovations in radar technology and stealth applications. The insights and tools developed herein lay the groundwork for continued exploration and advancement in electromagnetic wave analysis.

2. RCS THEORY

Radar Cross Section (RCS) is a pivotal concept in radar technology, representing the measure of an object's detectability by radar systems. This metric quantifies the extent of electromagnetic energy that an object scatters back toward the radar. Formulated as the ratio of the scattered power in the radar's direction to the power density of the incident wave, the RCS equation is given as:

$$\sigma = \lim_{R\to\infty} \frac{4\pi R^2 \left|\vec{E}_S\right|}{\left|\vec{E}_I\right|} \tag{2.1}$$

Here, σ denotes the RCS, R is the distance from the object to the radar, E_S is the scattered field, and E_I is the incident electromagnetic wave. The RCS, expressed in square meters, is influenced by several factors including the object's size, material, shape, orientation, and the frequency of the radar signal, each contributing to how the object reflects or scatters radar signals [1].

2.1 Scattering Mechanisms Influencing RCS

There are different scattering mechanisms as shown in Figure 2.1.

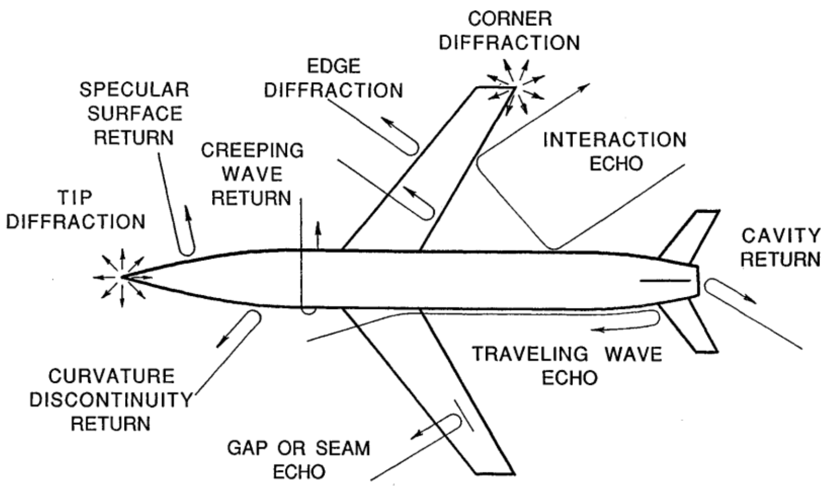

Figure 2.1 : Different scattering mechanisms.

2.1.1 Specular reflection

This mechanism occurs predominantly with smooth surfaces, where radar waves are reflected in a single, predictable direction, much like a mirror. The efficiency of specular reflection is highly dependent on the angle of incidence and the surface orientation relative to the radar. It plays a major role in determining the RCS for objects with large, flat, or uniformly curved surfaces.

2.1.2 Diffuse scattering

When radar waves encounter rough surfaces, the energy is scattered in multiple directions. This scattering reduces the predictability of the signal return and can significantly influence the RCS over a wide range of viewing angles. Diffuse scattering becomes more prominent as the surface irregularities approach the wavelength of the radar signal.

2.1.3 Edge diffraction

Edge diffraction occurs in objects with sharp edges or discontinuities. Radar waves bend or diffract around these edges, which contributes to the RCS even when the radar's line of sight is not directly aligned with the surface. This phenomenon is critical for understanding RCS in objects with complex geometric features.

2.1.4 Multiple scattering

In complex structures with multiple reflective surfaces, radar waves may undergo successive reflections and scattering events within the object. This interaction creates a compounded effect on the RCS, leading to intricate patterns that are highly sensitive to the object's geometry and the radar signal's frequency and angle of incidence.

2.2 Regions of RCS Definition

RCS varies across different regions, defined based on the size of the object D relative to the wavelength λ of the radar signal:

Rayleigh Region $(D << \lambda)$: Here, the object is much smaller than the wavelength. The RCS is proportional to the size of the object to the fourth power and inversely proportional to the wavelength to the fourth power, often applicable to small particles.

Resonance Region $(D \approx \lambda)$: The size of the object is comparable to the wavelength. In this region, the RCS can fluctuate significantly with changes in wavelength or object dimensions due to the complex interplay of various scattering mechanisms.

Optical Region $(D >> \lambda)$: When the object is substantially larger than the wavelength, RCS is primarily influenced by the object's geometric shape and orientation. Techniques in geometric and physical optics are used to analyze RCS in this region.

These regions and their characteristics are illustrated in Figure 2.2, providing a visual representation of the relationship between object size and wavelength across the Rayleigh, Resonance, and Optical regions.

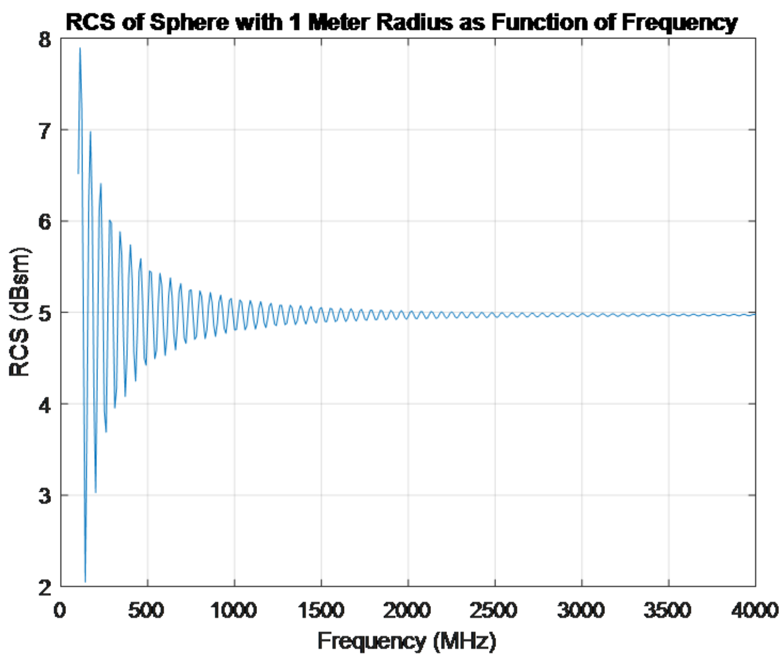

Figure 2.2 : RCS of a sphere with 1 meter radius for different frequencies.

2.3 RCS Calculation Methods

The methods used to calculate Radar Cross Section (RCS) can be broadly categorized into high-frequency techniques, which leverage optical-based approximations, and low-frequency techniques, which focus on full-wave solutions to electromagnetic problems. Each approach offers distinct advantages and limitations, making them suitable for specific scenarios depending on factors like the object's size, operational frequency, and the required level of accuracy.

2.3.1 High frequency techniques

High-frequency techniques are particularly effective for analyzing large, electrically significant objects where the wavelength of the incident wave is much smaller than the object's dimensions. These methods approximate the behavior of electromagnetic waves using principles borrowed from optics, making them computationally efficient for high-frequency scenarios. However, their accuracy can degrade when applied to objects with fine features or when the object's size becomes comparable to the wavelength.

2.3.1.1 Physical optics (PO)

Physical Optics simplifies the problem by assuming the incident field over the scatterer behaves as if it were illuminated by a plane wave. This assumption allows for efficient computation of the surface currents and scattered fields. PO is widely recognized for its balance between computational efficiency and accuracy, particularly for electrically large objects where detailed full-wave solutions become impractical. However, PO has limitations in capturing diffraction effects, making it less suitable for objects with sharp edges or intricate features.

2.3.1.2 Geometric optics (GO) and Geometric theory of diffraction (GTD)

Geometric Optics treats electromagnetic waves as rays and is most effective for smooth surfaces with large radii of curvature compared to the wavelength. It is computationally efficient and provides accurate results for objects with simple geometries [3]. However, GO falls short in scenarios involving diffraction, where edge effects cannot be neglected. The Geometric Theory of Diffraction (GTD), introduced by Keller, extends GO by incorporating diffraction effects from edges, corners, and tips. GTD improves accuracy in cases where GO's assumptions break down, but it still relies heavily on the geometric characteristics of the object.

2.3.1.3 Physical theory of Diffraction (PTD)

The Physical Theory of Diffraction builds upon PO by addressing its limitations in modeling diffraction effects. PTD includes contributions from diffracted fields generated at edges, which PO tends to neglect. This enhancement makes PTD more accurate for objects with sharp edges or complex geometrical features, though it comes at the cost of increased computational effort [4].

2.3.1.4 Shooting and bouncing rays (SBR)

SBR combines aspects of Geometric Optics and Physical Optics to handle multiple reflections and shadowing effects in complex geometries. In this approach, rays are traced as they bounce off the object's surfaces, with the phase and amplitude of the electric field computed at each bounce. SBR is particularly useful for analyzing intricate structures, such as aircraft and ships, where multiple scattering plays a significant role [5]. While SBR provides a powerful hybrid approach, its accuracy depends on the quality of ray tracing and the complexity of the geometry, and it can be computationally demanding for large-scale problems.

2.3.2 Low frequency techniques

Low-frequency techniques are based on full-wave solutions to Maxwell's equations, providing high accuracy by directly solving the electromagnetic problem. These methods are better suited for smaller objects or scenarios where the wavelength is comparable to the object's dimensions. However, they can be computationally intensive, particularly for high-frequency or large-scale problems.

2.3.2.1 Method of moments (MoM)

MoM involves solving integral equations derived from Maxwell's equations using Green's function. By converting these integral equations into systems of linear equations, MoM allows for matrix-based solutions. It is highly accurate for objects with complex geometries and provides detailed field distributions. However, its computational cost increases significantly with the size of the object or the frequency, as the matrix size grows with the number of unknowns. This makes MoM less suitable for electrically large objects [6].

2.3.2.2 Finite element method (FEM)

FEM discretizes the geometry of the problem into small elements, solving the boundary value problem using partial differential equations. It is highly versatile and capable of modeling inhomogeneous materials and complex boundary conditions [7]. FEM excels in low-frequency scenarios where precision is paramount, such as analyzing antennas or small-scale objects. However, the method's computational demands can be prohibitive for large objects or high-frequency applications, as the number of elements required increases dramatically.

3. PHYSICAL OPTICS METHOD

The physical Optics (PO) method is a high-frequency approximation technique, highly effective in situations where the target's size is substantially larger than the radar operation frequency. This method is especially relevant for target geometries lacking sharp edges and corners, making it apt for scenarios dominated by specular reflections. In the Physical Optics approach, the focus is on providing fast and reasonable results by simplifying the scattering problem while still maintaining a degree of accuracy.

A key step in applying the PO method involves discretizing the target geometry. This requires the development of a mesh structure that accurately reflects the target's surface characteristics. The essence of the PO approach lies in calculating the radiation integral across each discrete element of this mesh, such as triangular facets. By computing the surface current contributions for each of these elements and then superimposing them, the PO method effectively determines the total scattered field from the scatterer. Since the incident field is known, the scattered field thus calculated can be directly used for RCS computation.

One of the fundamental assumptions of the PO method is that current is induced only on the parts of the object that are illuminated by the radar signal. However, this assumption also leads to a significant limitation, particularly near shadow boundaries. In these regions, the abrupt transition to zero current reduces the accuracy of the PO method. Furthermore, the PO method tends to lose its accuracy as the observation point moves away from the specular reflection region, especially in cases involving complex scattering phenomena.

Another critical aspect of the PO method is its treatment of various scattering mechanisms. The method does not account for certain mechanisms such as surface waves, diffraction effects, and multiple reflections. This exclusion can lead to discrepancies in the calculated RCS, particularly in more complex scenarios where these effects play a significant role.

Despite these limitations, the PO method is frequently favored for RCS calculations, especially in high-frequency settings involving electrically large targets. Its appeal lies in its computational efficiency — the method simplifies the calculation process, thereby reducing the demand for high computational power. This makes it an attractive option for practical applications, particularly when a balance between computational load and result accuracy is essential.

In addition, the Physical Optics method addresses a specific challenge faced by the Geometric Optics (GO) method related to ray tracing on flat surfaces. GO requires an infinite number of reflection points for accurate modeling, a requirement that is unfeasible in practical scenarios. The PO method overcomes this by correlating the induced surface current on the illuminated parts of the object with the incoming magnetic field intensity. In shadow regions, it simplifies the model by assuming zero current, thereby providing a more manageable and efficient approach to RCS calculation. The PO approximation can be summarized with the formula below :

$$J_s = \begin{cases} 2\hat{n} \times H_i, & \text{illuminated region} \\ 0, & \text{shadowed region} \end{cases} \tag{3.1}$$

3.1 Derivation of Scattered Fields

In a homogeneous medium, the time-harmonic electric and magnetic fields must satisfy Maxwell's equations. These equations describe the relationship between electric and magnetic fields, currents, and charges. For the time-harmonic case, Maxwell's equations are expressed as:

$$\nabla \times E = -M - j\omega\mu H \tag{3.2}$$

$$\nabla \times H = J + j\omega\varepsilon E \tag{3.3}$$

In this context, E and H denote the electric and magnetic fields, respectively, while J represents the electric current density, and M corresponds to the magnetic current density. The medium's properties are characterized by μ (permeability) and ε (permittivity), with ω representing the angular frequency. These equations encapsulate the core principles that describe the behavior of electromagnetic waves.

In regions devoid of sources (where $J = M = 0$), these governing equations simplify significantly. Under these conditions, the electric and magnetic fields can be reformulated using auxiliary vector potentials: A, the magnetic vector potential, and F, the electric vector potential.

To facilitate analysis, the magnetic field H is commonly defined in terms of the magnetic vector potential A as follows:

$$H = \frac{1}{\mu}\nabla \times A \tag{3.4}$$

To ensure Maxwell's equations are satisfied, the magnetic field H is represented in terms of the vector potential A. This approach simplifies the problem, allowing focus on solving for A. Using this representation, the electric field E can be expressed as follows:

$$E = -\nabla\phi_e - j\omega A \tag{3.5}$$

where ϕ_e is an electric scalar potential that accounts for divergences in A. The connection between A and ϕ_e can be further clarified using the Lorenz condition:

$$\nabla \cdot A = -j\omega\mu\varepsilon\phi_e. \tag{3.6}$$

By incorporating the Lorenz condition into Maxwell's equations, we arrive at a key equation for A:

$$\nabla^2 A + k^2 A = -\mu J \tag{3.7}$$

where $k^2 = \omega^2\mu\varepsilon$ represents the square of the wave number. This equation, often referred to as the vector wave equation, describes how A propagates in a homogeneous medium. Once A is determined, the magnetic field H can be calculated, and subsequently, E can be derived using the earlier expressions.

In the special case where $k = 0$, corresponding to static conditions, and $J \neq 0$, the wave equation simplifies to:

$$\nabla^2 A = -\mu J \tag{3.8}$$

This is a form of Poisson's equation. A well-known example of a Poisson equation describes the relationship between scalar electric potential ϕ and charge density q:

$$\nabla^2\phi = -\frac{q}{\varepsilon} \tag{3.9}$$

The solution to equation (3.9) is given by:

$$\phi = \frac{1}{4\pi\varepsilon}\iiint_V \frac{q}{r}dV' \tag{3.10}$$

where r is the distance from a point on the charge density to the observation point. Drawing an analogy, the solution to equation (3.10) takes a similar form:

$$A = \frac{\mu}{4\pi}\iiint_V \frac{J}{r}dV' \tag{3.11}$$

Equation (3.11) provides the solution under static conditions. For time-varying fields, the solution is extended by incorporating the time-harmonic factor e^{-jkr}, which modifies the expression as:

$$A = \frac{\mu}{4\pi}\iiint_V \frac{Je^{-jkr}}{r}dV' \tag{3.12}$$

When the source is located at a position given by primed coordinates (x', y', z'), the vector potential A at a point of observation (x, y, z) is expressed as:

$$A(x,y,z) = \frac{\mu}{4\pi}\iiint_V \frac{J(x',y',z')e^{-jkR}}{R}dV' \tag{3.13}$$

where R represents the distance between the source point (x', y', z') and the observation point (x, y, z). If the source currents J and M are distributed over a surface rather than a volume, the expressions simplify into surface integrals:

$$A = \frac{\mu}{4\pi}\iint_S \frac{J_S(x',y',z')e^{-jkR}}{R}ds' \tag{3.14}$$

$$F = \frac{\varepsilon}{4\pi}\iint_S \frac{M_S(x',y',z')e^{-jkR}}{R}ds' \tag{3.15}$$

In scenarios where the observation point lies in the far-field region, the distance R between the source and observation points can be approximated as being nearly parallel to the distance r from the origin to the observation point. Mathematically, the relationship is given by [8]:

$$R = \left[r^2 + (r')^2 - 2rr'\cos\psi\right]^{1/2} \tag{3.16}$$

and in practice, R is often approximated as:

$$R = \begin{cases} r - r'\cos\psi & \text{for phase-dependent effects,} \\ r & \text{for amplitude-dominated variations.} \end{cases} \tag{3.17}$$

Where, ψ is the angle between vectors $\hat{r}$ and $\hat{r}'$ as shown in the Figure 3.1.

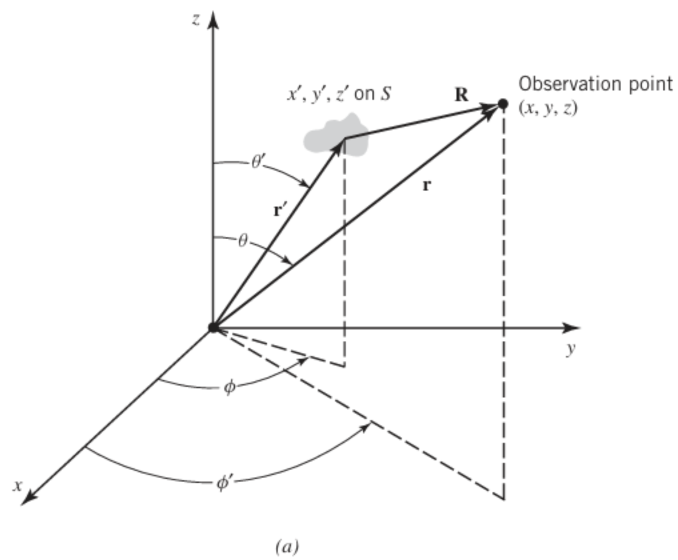

Figure 3.1 : Source and observation points in coordinate system.

By substituting these approximations into the surface integrals for vector potentials, the expressions for far-field observations simplify to:

$$A \approx \frac{\mu e^{-jkr}}{4\pi r} N, \quad F \approx \frac{\varepsilon e^{-jkr}}{4\pi r} L \tag{3.18}$$

where:

$$N = \iint_S J_S e^{jkr'\cos\psi}, ds', \quad L = \iint_S M_S e^{jkr'\cos\psi} ds' \tag{3.19}$$

In the far-field region, only the angular components of the electric and magnetic fields—denoted as θ and ϕ—are significant, while the radial components are negligible. The primary field components can thus be expressed as:

$$E \approx -j\omega A, \quad H \approx -j\omega F \tag{3.20}$$

The radial components of the electric and magnetic fields contribute negligibly in far-field conditions, as the dominant θ- and ϕ-components primarily dictate the field behavior. The E- and H-fields in this region exhibit orthogonality to each other and the radial direction, consistent with plane wave properties. These fields are further linked by the intrinsic impedance of the medium. The governing relations for the fields in terms of the vector potentials A and F are given by:

$$E = -\frac{1}{\varepsilon}\nabla \times F, \quad H = \frac{1}{\mu}\nabla \times A \tag{3.21}$$

The far-field expressions for the E- and H-fields can be parameterized based on the spherical components. The angular components relate to the vector potentials and medium impedance as follows:

$$E_\theta \approx -j\omega\eta\phi, \quad E_\phi \approx +j\omega\eta\theta \tag{3.22}$$

$$H_\theta \approx +j\omega\frac{A_\phi}{\eta}, \quad H_\phi \approx -j\omega\frac{A_\theta}{\eta} \tag{3.23}$$

The resultant far-field components, derived from the above relations, are expressed as:

$$E_r \approx 0, \quad E_\theta \approx -j\omega\left(A_\theta + \eta\phi\right), \quad E_\phi \approx -j\omega\left(A_\phi - \eta\theta\right) \tag{3.24}$$

$$H_r \approx 0, \quad H_\theta \approx \frac{j\omega}{\eta}\left(A_\phi - \eta\theta\right), \quad H_\phi \approx -\frac{j\omega}{\eta}\left(A_\theta + \eta\phi\right) \tag{3.25}$$

The potentials in far-field conditions are defined as:

$$A_\theta = \frac{\mu e^{-jkr}}{4\pi r}N_\theta, \quad A_\phi = \frac{\mu e^{-jkr}}{4\pi r}N_\phi, \tag{3.26}$$

$$F_\theta = \frac{\varepsilon e^{-jkr}}{4\pi r}L_\theta, \quad F_\phi = \frac{\varepsilon e^{-jkr}}{4\pi r}L_\phi \tag{3.27}$$

By substituting these potentials into the field equations, the explicit far-field components become:

$$E_r \approx 0, \quad E_\theta \approx -\frac{jke^{-jkr}}{4\pi r}\left(L_\phi + \eta N_\theta\right), \quad E_\phi \approx \frac{jke^{-jkr}}{4\pi r}\left(L_\theta - \eta N_\phi\right) \tag{3.28}$$

$$H_r \approx 0, \quad H_\theta \approx \frac{j\omega}{\eta}\frac{e^{-jkr}}{4\pi r}\left(N_\phi - \frac{L_\theta}{\eta}\right), \quad H_\phi \approx -\frac{j\omega}{\eta}\frac{e^{-jkr}}{4\pi r}\left(N_\theta + \frac{L_\theta}{\eta}\right) \tag{3.29}$$

To compute the field components, the terms N_θ, N_ϕ, L_θ, and L_ϕ must be derived. Choosing the most suitable coordinate system can significantly simplify these evaluations. For objects with geometries that align well with rectangular coordinates, the surface integrals can be expressed as:

$$N = \int_S J_s e^{jkr'} \cos\psi \, ds' = \int_S \left(\hat{a}_x J_x + \hat{a}_y J_y + \hat{a}_z J_z\right) e^{jkr'\cos\psi} \, ds' \tag{3.30}$$

$$L = \int_S M_s e^{jkr'} \cos\psi \, ds' = \int_S \left(\hat{a}_x M_x + \hat{a}_y M_y + \hat{a}_z M_z\right) e^{jkr'\cos\psi} \, ds' \tag{3.31}$$

To transition from rectangular to spherical components, the following coordinate transformation can be applied:

$$\begin{bmatrix} \hat{a}_x \\ \hat{a}_y \\ \hat{a}_z \end{bmatrix} = \begin{bmatrix} \sin\theta\cos\phi & \cos\theta\cos\phi & -\sin\phi \\ \sin\theta\sin\phi & \cos\theta\sin\phi & \cos\phi \\ \cos\theta & -\sin\theta & 0 \end{bmatrix} \begin{bmatrix} \hat{a}_r \\ \hat{a}_\theta \\ \hat{a}_\phi \end{bmatrix} \tag{3.32}$$

This transformation makes it possible to isolate the θ- and ϕ-components as follows:

$$N_\theta = \int_S \left(J_x \cos\theta\cos\phi + J_y \cos\theta\sin\phi - J_z \sin\theta\right) e^{jkr'\cos\psi} \, ds' \tag{3.33}$$

$$N_\phi = \int_S \left(-J_x \sin\phi + J_y \cos\phi\right) e^{jkr'\cos\psi} \, ds' \tag{3.34}$$

$$L_\theta = \int_S \left(M_x \cos\theta\cos\phi + M_y \cos\theta\sin\phi - M_z \sin\theta\right) e^{jkr'\cos\psi} \, ds' \tag{3.35}$$

$$L_\phi = \int_S \left(-M_x \sin\phi + M_y \cos\phi\right) e^{jkr'\cos\psi} \, ds' \tag{3.36}$$

For surfaces lying primarily in the x-y plane, the term $r'\cos\psi$, representing the projection of $\hat{r}'$ in the radial direction, can be rewritten as:

$$r'\cos\psi = x'\sin\theta\cos\phi + y'\sin\theta\sin\phi \tag{3.37}$$

3.2 Application of Physical Optics Approximation

The Physical Optics (PO) method provides a streamlined approach for estimating scattered fields by focusing on the illuminated regions of the scatterer's surface and approximating the induced surface currents. This allows for efficient computation of the scattered fields without the need to solve Maxwell's equations over the entire scatterer's volume.

The first step in this method involves determining the induced surface current density, J_S, which is approximated as:

$$J_S \approx 2\hat{n} \times H_i \tag{3.38}$$

where $\hat{n}$ represents the outward unit normal to the surface, and H_i is the tangential magnetic field component of the incident wave. This approximation is valid for perfect conductors and is applied only to the regions illuminated by the incident wave. In shadowed regions, where the incident wave does not reach, the surface current density J_p is considered zero.

For far-field conditions, the radial components of the electric and magnetic fields are negligible compared to the angular components. Under these assumptions, the incident electric and magnetic fields can be expressed as:

$$E_i = \left(E_{i\theta}\hat{a}_\theta + E_{i\phi}\hat{a}_\phi\right) e^{jk\cdot R} \tag{3.39}$$

$$H_i = \frac{\hat{a}_r \times E_i}{\eta_0} = \frac{1}{\eta_0}\left(E_{i\phi}\hat{a}_\theta - E_{i\theta}\hat{a}_\phi\right) e^{jk\cdot R} \tag{3.40}$$

where k is the wave number and R is the distance between the source and observation points, and $\eta_0 = \sqrt{\mu/\varepsilon}$ is the intrinsic impedance of the medium. Here, $E_{i\theta}$ and $E_{i\phi}$ denote the angular components of the incident electric field, while R accounts for the relative position between the source and observation points.

For far field condition, the distance between the source and observation point, $|\hat{r} - \hat{r}'|$, can be approximated as:

$$|\hat{r} - \hat{r}'| \approx r - \hat{r}' \cdot \hat{a}_r \tag{3.41}$$

This simplifies the phase term to:

$$\frac{e^{-jk|\hat{r}-\hat{r}'|}}{|\hat{r}-\hat{r}'|} \approx \frac{e^{-jkr}}{r} e^{jk\hat{r}'\cdot\hat{a}_r} \tag{3.42}$$

Using this approximation, the incident electric and magnetic fields become:

$$E_i = \left(E_{i\theta}\hat{a}_\theta + E_{i\phi}\hat{a}_\phi\right) e^{-jkr} e^{jk\hat{r}'\cdot\hat{a}_r} \tag{3.43}$$

$$H_i = \frac{\hat{a}r \times E_i}{\eta_0} = \frac{1}{\eta_0}\left(E_{i\phi}\hat{a}_\theta - E_{i\theta}\hat{a}_\phi\right) e^{-jkr} e^{jk\hat{r}'\cdot\hat{a}_r} \tag{3.44}$$

The surface current density, J_S, can then be derived using equations (3.38) and (3.44), yielding:

$$J_S = \frac{2}{\eta_0}\left(E_{i\phi}\hat{a}_\theta - E_{i\theta}\hat{a}_\phi\right) e^{-jkr} e^{jk\hat{r}'\cdot\hat{a}_r} \tag{3.45}$$

The scattered field can be computed by combining the approximations for the incident fields and current densities. This results in:

$$E_s \approx \frac{-j\omega\mu e^{-jkr}}{4\pi r} \iint_S J_S e^{jk\hat{r}'\cdot\hat{a}_r} ds' \tag{3.46}$$

For monostatic case, equivalently:

$$E_s \approx \frac{-jk\eta_0}{4\pi r} \iint_S \left(\hat{a}_x J_x + \hat{a}_y J_y + \hat{a}_z J_z\right) e^{2jkr'\cdot\hat{a}_r} ds' \tag{3.47}$$

3.3 Triangulation of the Target Geometry (Meshing)

In scattering problems, meshing is essential because it enables the numerical evaluation of surface integrals over complex geometries. The scattered field depends on induced surface currents, which are distributed across the surface of the target. Since real-world geometries often cannot be represented by simple mathematical functions, the surface is discretized into triangular elements. Triangular meshing is particularly effective for representing arbitrary shapes and provides a practical framework for applying Physical Optics approximations. It ensures efficient numerical integration, supports illumination testing, and allows flexible and accurate modeling of the target's geometry. Figure 3.2 illustrates a triangular mesh element, where the vertices are indexed counterclockwise. The position vectors of the vertices in Cartesian coordinates are:

$$\vec{r}_n = x_n\hat{a}_x + y_n\hat{a}_y + z_n\hat{a}_z \tag{3.48}$$

The edge vectors of the triangle are calculated as:

$$\vec{l}_1 = \vec{r}_2 - \vec{r}_1, \quad \vec{l}_2 = \vec{r}_3 - \vec{r}_2, \quad \vec{l}_3 = \vec{r}_1 - \vec{r}_3. \tag{3.49}$$

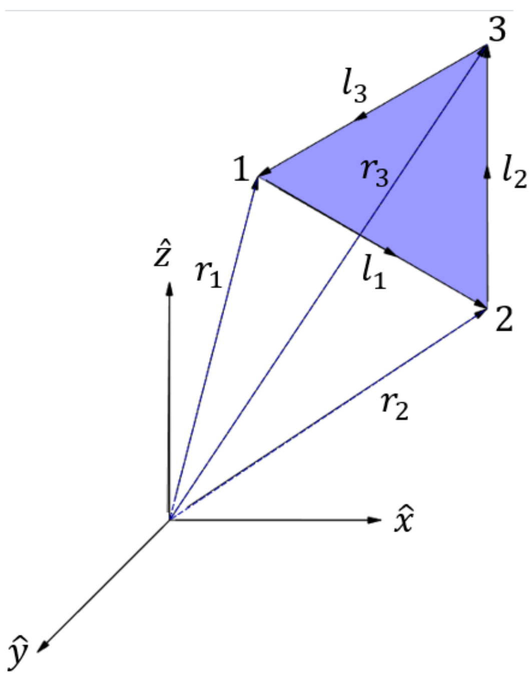

Figure 3.2 : Triangular surface element.

To test whether a triangular surface is illuminated, the angle between the unit normal $\hat{n}$ of the surface and the propagation vector of the incident plane wave $-\hat{k}_i$ is considered. If the cosine of this angle is positive, the surface is illuminated; otherwise, it lies in the shadow region. This condition can be expressed as:

$$-\hat{k}_i \cdot \hat{n} > 0 \tag{3.50}$$

In practical terms, this involves evaluating the scalar product of $-\hat{k}_i$ and $\hat{n}$.

Figure 3.3 shows the geometric relationship between the surface normal and the incident wave. For a plane wave incident at angles θ_i and ϕ_i relative to the radar's origin, the propagation vector $\hat{k}_i$ is:

$$\hat{k}_i = -\left(u_i\hat{a}_x + v_i\hat{a}_y + w_i\hat{a}_z\right) \tag{3.51}$$

where the direction cosines are given by:

$$u_i = \sin\theta_i \cos\phi_i, \quad v_i = \sin\theta_i \sin\phi_i, \quad w_i = \cos\theta_i. \tag{3.52}$$

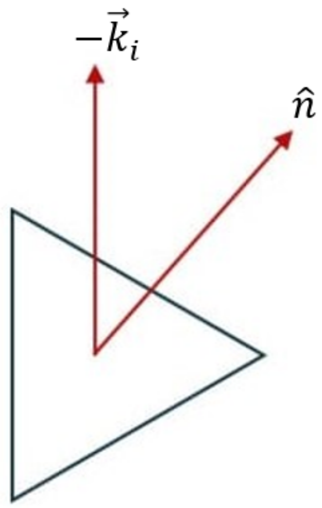

Figure 3.3 : Relationship between surface normal and incident Wave.

The unit normal $\hat{n}$ of a triangular surface is computed using the cross product of two edge vectors:

$$\hat{n} = \frac{\vec{l}_1 \times \vec{l}_2}{|\vec{l}_1||\vec{l}_2|} \tag{3.53}$$

This calculation assumes that the vertices of the triangle are indexed counterclockwise, consistent with the right-hand rule, where the thumb points in the direction of the surface normal.

The area A of the triangular surface can also be determined using the cross product of the edge vectors:

$$A = \frac{|\vec{l}_1 \times \vec{l}_2|}{2} \tag{3.54}$$

For each illuminated triangle, the scattered field contribution is calculated based on the source point at the triangle's center. The total scattered field at the observation point is obtained by summing the scattered field contributions of all illuminated triangular elements. This summation integrates the effects of the geometry and illumination conditions, ensuring an accurate representation of the target's scattering characteristics.

By focusing on illuminated regions and ensuring precise meshing, the Physical Optics method provides an efficient and robust approach for solving scattering problems, especially in the high-frequency regime where surface discretization significantly impacts RCS calculations.

3.4 Solution of The Integral Equation

In the integral expressions for $\vec{A}_s$ and $\vec{E}_s$, the exponential term represents the phase shift of the wave due to its travel from the source to the target surface and then from the target surface to the observation point. This phase shift is crucial for accurately modeling the scattering behavior of the target. This term, therefore, can be analyzed alone to efficiently calculate the scattering field for monostatic case as:

$$\iint_A e^{2jk\hat{r}' \cdot \hat{a}_r} dA \tag{3.55}$$

One of the challenges in computing this integral arises from its oscillatory nature, especially at high frequencies. The oscillation is due to the exponential term containing the wave number k, which varies rapidly with small changes in the phase. Standard numerical integration techniques like Simpson's rule or Newton-Cotes formulas are not effective for such integrals due to the high-frequency oscillations [2].

To address this, the Ludwig method is adapted for approximating the integral I [9]. The equation (3.55) can be represented in a more general form as :

$$I = \int\int_S A(u,v)e^{jkB(u,v)}\,du\,dv \tag{3.56}$$

Here, S represents the surface integration domain, while u and v denote the corresponding integration variables. The function Ae^{jkB} depends on the field incident on the aperture or object. The total result is computed by summing I_c over all triangular cells. Consequently, equation (3.56) can be expressed as:

$$I = \sum_{c=1}^{N_c} I_c \tag{3.57}$$

where N_c refers to the total count of integration cells, and I_c denotes the result obtained from integrating over the c-th cell. To determine I_c, it is presumed that the integrand's amplitude and phase can be separately represented through planar function approximations of the form:

$$A_c(u,v) = A_u u + A_v v + A_0 \tag{3.58}$$

$$B_c(u,v) = B_u u + B_v v + B_0 \tag{3.59}$$

respectively. In the equations above, u and v denote Cartesian coordinates, with the subscript c emphasizing that the interpolation coefficients are specific to each cell. To simplify the analytical evaluation of a surface integral over a triangular cell, the local coordinate system p and q is often employed. Using this coordinate system, the integral I_c can be expressed as:

$$I_c = \int_0^1 \int_0^{1-p} C_c(p,q)e^{jD_c(p,q)}\,dq\,dp \tag{3.60}$$

where $C_c(p,q)$ and $D_c(p,q)$ are functions of the local coordinates p and q. where

$$C_c(p,q) = 1, \tag{3.61}$$

$$D_c(p,q) = D_p p + D_q q + D_o. \tag{3.62}$$

In the above equations, D coefficients are given by:

$$D_p = k(B_{c,1} - B_{c,3}), \quad D_q = k(B_{c,2} - B_{c,3}), \quad D_o = kB_{c,3}, \tag{3.63}$$

For a detailed representation, it can be further expand as :

$$D_p = k_0\left[(x_{c,1} - x_{c,3})(u_i + u) + (y_{c,1} - y_{c,3})(v_i + v) + (z_{c,1} - z_{c,3})(w_i + w)\right] \tag{3.64}$$

$$D_q = k_0\left[(x_{c,2} - x_{c,3})(u_i + u) + (y_{c,2} - y_{c,3})(v_i + v) + (z_{c,2} - z_{c,3})(w_i + w)\right] \tag{3.65}$$

$$D_o = k_0\left[x_{c,3}(u_i + u) + y_{c,3}(v_i + v) + z_{c,3}(w_i + w)\right] \tag{3.66}$$

The free-space wave number k_0 and the coordinates $x_{c,i}$, $y_{c,i}$, and $z_{c,i}$ of each node of the facet are used in this computation. In a monostatic radar configuration, the direction cosines for the incident and scattered fields are equal due to the nature of the setup. The components of the direction cosines are expressed as:

$$u = \sin\theta\cos\phi, \quad v = \sin\theta\sin\phi, \quad w = \cos\theta \tag{3.67}$$

$$u_i = u, \quad v_i = v, \quad w_i = w \tag{3.68}$$

- u, v, and w are the direction cosines of the scattered field.
- u_i, v_i, and w_i are the direction cosines of the incident field, which are equal to u, v, and w in the monostatic case.
- θ and ϕ represent the angular coordinates of the scattering direction in spherical coordinates.

The integral I_c can subsequently be computed analytically, resulting in:

$$I_c = 2S_c e^{jD_o}\left\{ e^{jD_p}\left[\frac{1}{D_p(D_q - D_p)}\right] - e^{jD_q}\left[\frac{1}{D_q(D_q - D_p)}\right] - \frac{1}{D_p D_q}\right\} \tag{3.69}$$

where S_c is the area of the triangular cell (in the u and v coordinates).

where S_c represents the area of the triangular cell in the u and v coordinates.

The I_c expression in equation (3.69) contains removable singularities that cause numerical difficulties when $|D_p|$, $|D_q|$, or $|D_q - D_p|$ approach small values. To address these cases, simple and effective expressions can be derived by expanding the term e^{jD_c} from equation (3.60) into a Taylor series around the relevant small parameter and performing term-by-term analytical integration of the resulting series:

- If $|D_p| < L_t$ and $|D_q| \geq L_t$ (no restrictions on $|D_q - D_p|$):

$$I_c = 2S_c \frac{e^{jD_o}}{jD_q} \sum_{n=0}^{\infty} \frac{(jD_p)^n}{n!} \left\{ \frac{-1}{n+1} + e^{jD_q} G(n, -D_q) \right\} \tag{3.70}$$

- If $|D_p| < L_t$ and $|D_q| < L_t$ (no restrictions on $|D_q - D_p|$):

$$I_c = 2S_c e^{jD_o} \sum_{n=0}^{\infty} \sum_{m=0}^{\infty} \frac{(jD_p)^n (jD_q)^m}{(n+m+2)!} \tag{3.71}$$

- If $|D_p| \geq L_t$ and $|D_q| < L_t$ (no restrictions on $|D_q - D_p|$):

$$I_c = 2S_c e^{jD_o} e^{jD_p} \sum_{n=0}^{\infty} \frac{(jD_q)^n}{n!} \frac{1}{n+1} G(n+1, -D_p) \tag{3.72}$$

- If $|D_p| \geq L_t$, $|D_q| \geq L_t$, and $|D_q - D_p| < L_t$:

$$I_c = 2S_c \frac{e^{jD_o}}{jD_q} \sum_{n=0}^{\infty} \frac{[j(D_p - D_q)]^n}{n!} \left\{ -G(n, D_q) + e^{jD_q} \frac{1}{n+1}] \right\} \tag{3.73}$$

Where, G function is defined as :

$$G(n, w) = \int_0^1 s^n e^{jws} ds \tag{3.74}$$

The function $G(n, w)$ can be computed recursively using its defining relation:

$$G(n, w) = \frac{e^{jw} - nG(n-1, w)}{jw}, \quad \text{for } n \geq 1 \tag{3.75}$$

along with the initial value:

$$G(0, w) = \frac{e^{jw} - 1}{jw} \tag{3.76}$$

3.4.1 Coordinate transformations

In computational electromagnetics, accurately evaluating surface integrals is critical for analyzing electromagnetic scattering, radiation, and related phenomena. Here for the ease of understanding, the equation (3.47) is rewritten, which describes the scattering field integral :

$$E_s \approx \frac{-jk\eta_0}{4\pi r} \iint_S \left(\hat{a}_x J_x + \hat{a}_y J_y + \hat{a}_z J_z\right) e^{2jkr'\cdot\hat{a}_r}\, ds' \tag{3.77}$$

As it can be seen, this integral involves contributions from all three current density components, J_x, J_y, and J_z, which adds complexity to the computation, especially for arbitrary geometrical surfaces. However, the coordinate transformation process can significantly reduce this complexity by leveraging the alignment of local coordinate systems with surface geometries.

For example, if the integration surface lies entirely in the xy-plane, the current density component J_z becomes zero due to the absence of a z-directed component on the plane. While such simplifications are straightforward for planar surfaces aligned with global axes, they are generally not applicable to arbitrarily oriented triangle surfaces that form the facets of complex geometries.

By transforming from the global coordinate system (x,y,z) to a local coordinate system (x'',y'',z'') for each triangular surface, the local z'' is aligned with the surface normal of the triangle. This alignment ensures that the transformed current density component $J_{z''}$ vanishes because the current flows entirely within the plane of the surface. Consequently, the integral simplifies, requiring contributions only from the in-plane current density components $J_{x''}$ and $J_{y''}$ in the local coordinate system.

Transitioning between global and local coordinate systems involves two steps , as illustrated in Figure 3.4.

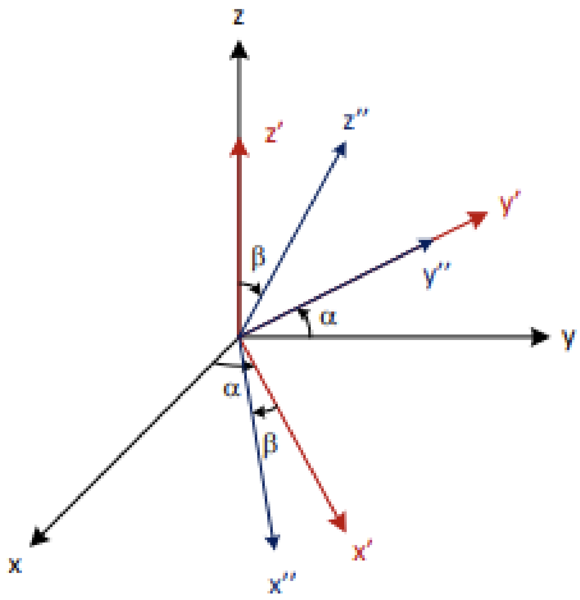

Figure 3.4 : Coordinate transformation from global to local coordinates.

1. First Transformation: Rotation in the xy-Plane The first step aligns the local coordinate system's z-axis with a specific direction in the global frame. This involves rotating the x and y axes by an angle α, while keeping the z-axis fixed, to form the intermediate system (x', y', z'). The angle α is computed as:

$$\alpha = \tan^{-1}\left(\frac{n_x}{n_y}\right) \tag{3.78}$$

where n_x and n_y are the x and y components of the unit normal vector of the surface.

The transformation matrix $\bar{D}'$ for this rotation is:

$$\bar{D}' = \begin{bmatrix} \cos\alpha & \sin\alpha & 0 \\ -\sin\alpha & \cos\alpha & 0 \\ 0 & 0 & 1 \end{bmatrix} \tag{3.79}$$

The intermediate coordinates (x', y', z') are obtained by:

$$\begin{bmatrix} x' \\ y' \\ z' \end{bmatrix} = \bar{D}' \begin{bmatrix} x \\ y \\ z \end{bmatrix} \tag{3.80}$$

2. Second Transformation: Rotation in the xz'-Plane The second step rotates the intermediate coordinates about the y'-axis by an angle β, aligning the local system (x'', y'', z'') with the desired orientation. The angle β is determined by:

$$\beta = \cos^{-1}\left(\hat{a}_z \cdot \hat{n}\right) \tag{3.81}$$

where $\hat{a}_z$ is the unit vector along the global z-axis, and $\hat{n}$ is the unit normal vector of the surface.

The corresponding transformation matrix $\bar{D}''$ is:

$$\bar{D}'' = \begin{bmatrix} \cos\beta & 0 & -\sin\beta \\ 0 & 1 & 0 \\ sin\beta & 0 & \cos\beta \end{bmatrix} \tag{3.82}$$

The final transformed coordinates (x'', y'', z'') are obtained by:

$$\begin{bmatrix} x'' \\ y'' \\ z'' \end{bmatrix} = \bar{D}'' \begin{bmatrix} x' \\ y' \\ z' \end{bmatrix} \tag{3.83}$$

Combined Transformation Combining the two transformations, the final coordinates are expressed as:

$$\begin{bmatrix} x'' \\ y'' \\ z'' \end{bmatrix} = \bar{D}''\bar{D}' \begin{bmatrix} x \\ y \\ z \end{bmatrix} \tag{3.84}$$

Inverse Transformation To revert to the global coordinate system after computations in the local frame, the inverse of the combined transformation matrix is applied:

$$\begin{bmatrix} x \\ y \\ z \end{bmatrix} = \left(\bar{D}''\bar{D}'\right)^{-1} \begin{bmatrix} x'' \\ y'' \\ z'' \end{bmatrix} \tag{3.85}$$

Vector and Direction Cosine Transformation In addition to transforming coordinates, unit vectors and direction cosines must also undergo the same transformations to ensure consistency in electromagnetic field and scattering integral calculations. This comprehensive approach ensures precise modeling of complex geometrical configurations.

4. ADDITIONAL METHODS TO IMPROVE RESULTS

4.1 Mesh Refinement Algorithm

The algorithm presented is designed for refining a mesh model, particularly useful in Radar Cross Section (RCS) analysis. Its primary objective is to ensure that each triangular facet in the model conforms to a specific area constraint, which is crucial for accurate electromagnetic wave scattering simulations. By refining the mesh, the algorithm enables the model to better represent the target's physical characteristics, especially under the specified radar frequency. This refinement enhances the fidelity of RCS predictions, particularly for targets with complex geometries.

The algorithm operates on a model provided in STL format. It begins by reading the STL file and extracting geometric data, including the coordinates of corner points and the connectivity matrix. Key parameters, such as the radar frequency, the speed of light, and the corresponding wavelength, are then defined. These parameters form the basis for calculating a maximum permissible area for each triangle in the mesh. It's worth noting that defining this area is critical, as it directly impacts the accuracy of RCS calculations larger triangles can introduce errors in regions with high curvature or intricate detail.

Initially, the algorithm visualizes the model before refinement. This visualization step is particularly helpful for understanding the model's baseline structure and identifying regions where large triangles could lead to inaccuracies. The triangulated mesh, with its orientation and distribution of facets, is displayed alongside the face normals and centers. From experience, this step provides a clear overview and highlights areas requiring refinement.

The core of the algorithm is an iterative refinement process, where the mesh is adjusted to ensure that no triangular facet exceeds the pre-determined maximum area. Larger facets are subdivided until they meet the area constraint.

This process is computationally intensive but necessary to achieve reliable RCS predictions. For instance, during testing, it is observed that regions with sharp edges required significantly more refinement than flat surfaces to avoid inaccuracies in scattering simulations.

Once refinement is complete, the algorithm recalculates key properties of the mesh, including facet areas, centers, and normals. The refined mesh is then saved as a new STL file. A final visualization step compares the refined mesh with its pre-refinement counterpart. This visual comparison is not just for verification but also to understand how the refinement process affects different regions of the model. Figures 4.1 and 4.2 illustrate this comparison, highlighting the significant improvement in the uniformity of triangle areas.

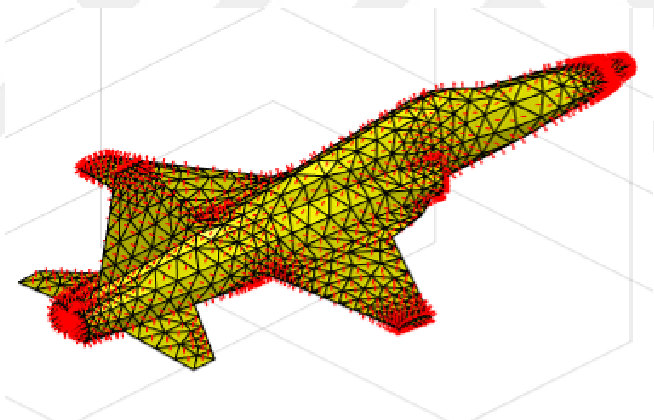

Figure 4.1 : Original mesh.

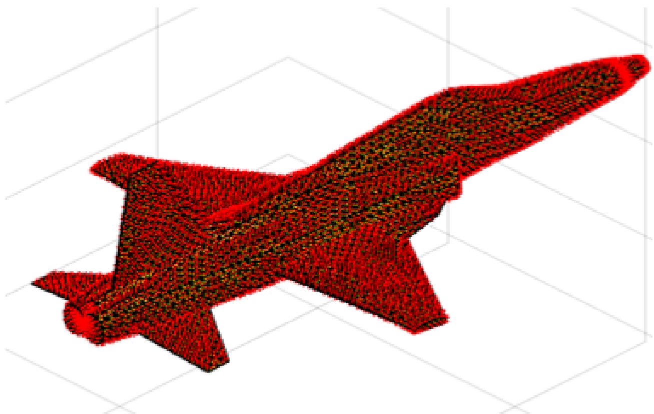

Figure 4.2 : Refined mesh.

The significance of this algorithm lies in its ability to optimize mesh models for RCS analysis. By ensuring that each facet adheres to a specific area constraint, the algorithm improves the precision of RCS predictions, particularly when the radar wavelength is comparable to the dimensions of the target's features. However, one limitation is the computational cost of refinement for very large models. During our implementation, we observed that refining models with millions of facets required significant memory and processing time, which could be a challenge for real-time applications.

In conclusion, this algorithm provides a systematic approach to refining 3D mesh models for RCS analysis. By tailoring the mesh geometry to the radar wavelength, it enhances the accuracy of electromagnetic wave interaction simulations. This is particularly important in applications like stealth technology and radar system design, where precision is paramount. As illustrated in Figures 4.3 and 4.4, the refinement process results in a much more uniform distribution of triangle areas, leading to more reliable RCS computations.

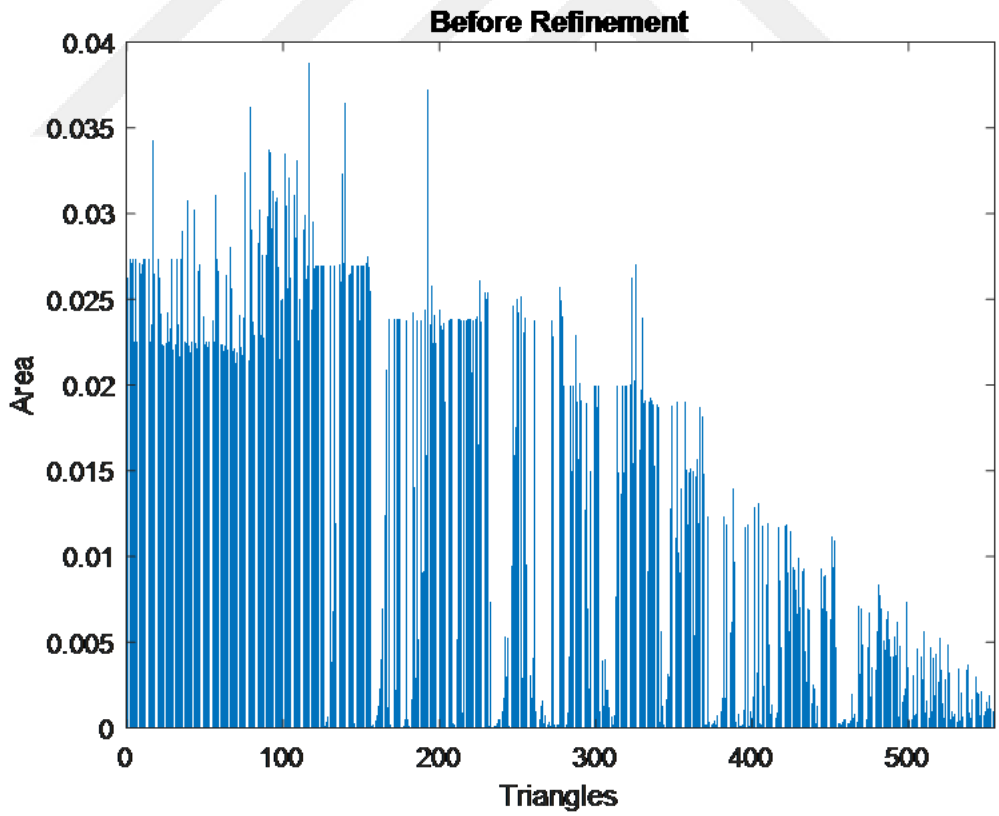

Figure 4.3 : Triangular mesh areas before refinement

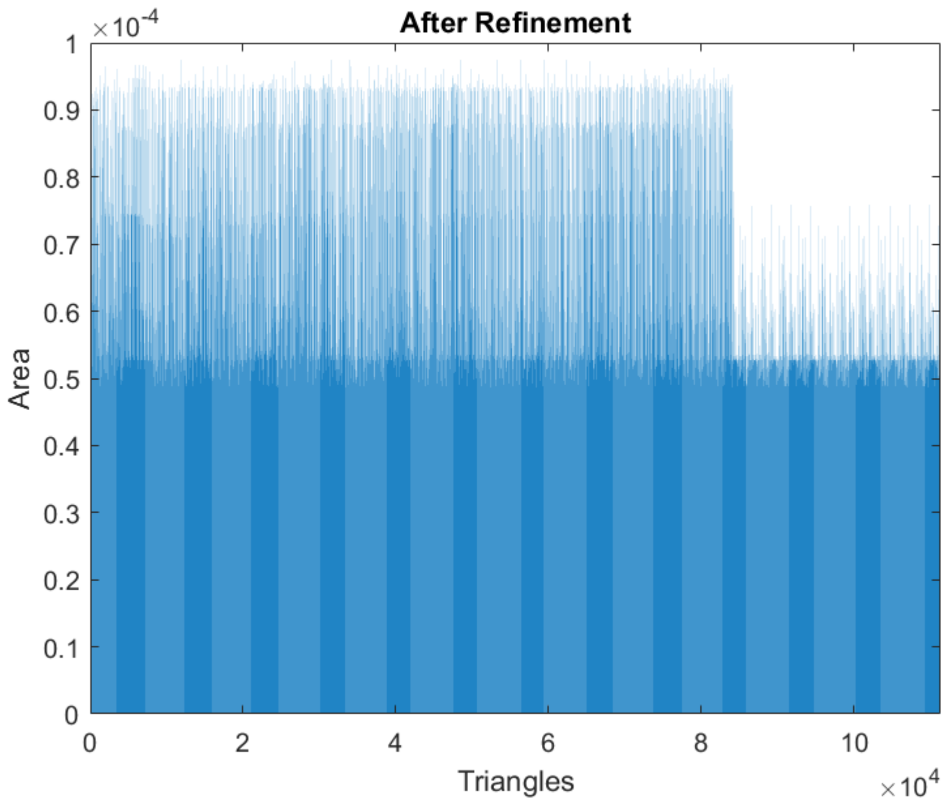

Figure 4.4 : Triangular mesh areas before refinement.

4.2 Shadowing Algorithm

Shadowing is a critical factor in Radar Cross Section (RCS) analysis, significantly influencing the detectability of objects by radar systems. It occurs when certain parts of a target are obscured, or shadowed, from the radar's perspective due to obstruction by other parts of the target. This creates shadow regions behind the target relative to the radar source, which do not contribute to the radar return.

The impact of shadowing on RCS measurements is substantial. Shadowed regions do not reflect radar signals back to the receiver, effectively reducing the target's perceived size and consequently its RCS. If shadowing effects are not accurately modeled, this can lead to underestimations of the target's RCS. Thus, precise modeling of shadowing is essential for realistic and reliable RCS predictions.

To address this challenge, computational techniques such as ray tracing and physical optics are employed to simulate radar wave interactions with an object's surface. For instance, ray tracing can map the trajectories of radar waves, distinguishing between illuminated and shadowed facets of a complex geometry. These techniques enable analysts to predict shadow regions and their impact on the overall RCS.

Shadowing is not merely a computational challenge but also a design consideration in stealth technology. Stealth designers intentionally shape objects to direct radar waves away from the receiver, creating shadow regions over high-reflectivity areas. This strategic manipulation minimizes the RCS, making the object less detectable to radar systems.

Despite its utility, shadowing analysis is inherently complex. The geometry of the target and the frequency of the radar wave can significantly alter shadowing patterns. Even minor variations in these parameters can lead to dramatic changes in RCS readings. Additionally, multipath effects—where radar waves reflected from illuminated parts of the target impinge on shadowed regions—add further complexity, necessitating advanced modeling techniques.

Understanding shadowing is vital for accurate RCS evaluation and plays a pivotal role in the development of radar-evading technologies. Advances in computational methods continue to improve the ability to model and mitigate shadowing effects, resulting in more nuanced approaches to RCS analysis and stealth design.

For this thesis, a shadowing algorithm is implemented to efficiently calculate the RCS of the proposed models. This algorithm ensures accurate representation of shadowed regions, enabling reliable RCS predictions and contributing to the overall fidelity of the analysis.

4.2.1 Algorithm development process

At the beginning of the algorithm, the decision of whether a face is illuminated or shadowed is made according to the dot product of the unit normal vector and the incident wave vector as mentioned before. While a positive result indicates that relevant face is illuminated and vice versa. Then, a series of mathematical tests are applied to this illuminated faces to eliminate the shadowed ones by another. [10]

As shown in the diagram in the Figure 4.5, all of the illuminated faces are judged whether they shadowing another illuminated face, which requires meeting some specific conditions.

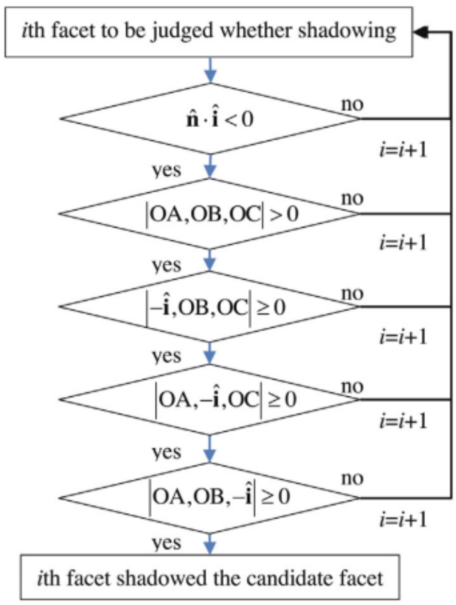

Figure 4.5 : The diagram of the shadowing algorithm.

For the first condition, the center of the shadowed facet must lie within the projection of the shadowing facet. This is confirmed using the determinant:

$$\det(\mathrm{OA}, \mathrm{OB}, \mathrm{OC}) = \mathrm{OA} \cdot (\mathrm{OB} \times \mathrm{OC}) > 0 \tag{4.1}$$

where $\mathrm{OA}, \mathrm{OB}, \mathrm{OC}$ are vectors from the shadowed facet's center to the vertices A, B, C of the shadowing facet, as depicted in the Figure 4.6.

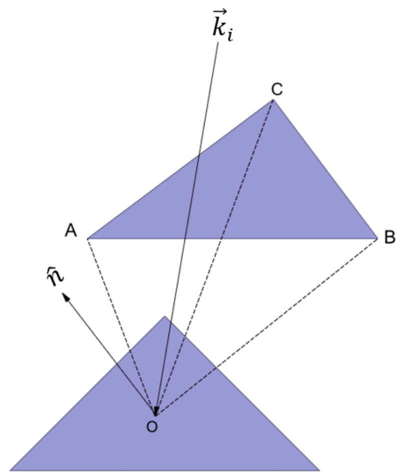

Figure 4.6 : Shadowing of one face on another face.

For the second condition, the radar propagation vector must puncture the shadowing facet, as verified by:

$$\text{-i}, \mathrm{OB}, \mathrm{OC} \geq 0, \quad \mathrm{OA}, \text{-i}, \mathrm{OC} \geq 0, \quad \mathrm{OA}, \mathrm{OB}, \text{-i} \geq 0 \tag{4.2}$$

These conditions collectively ensure that the shadowing relationship is accurately identified. Edge cases, such as when the radar vector intersects an edge of the shadowing facet, are handled by using $\geq$ instead of $>$, preventing erroneous exclusions.

The algorithm evaluates these conditions sequentially for computational efficiency. If any condition fails, the algorithm immediately skips to the next facet pair, saving processing time. This simplicity ensures compatibility with existing RCS analysis frameworks and makes the approach suitable for large-scale models.

The implementation of this method uses standard vector operations—cross products, dot products, and matrix determinants—which are computationally efficient and widely supported by mathematical software libraries.

By accurately determining shadowed regions, this algorithm enhances the reliability of RCS modeling, especially for complex geometries where shadowing significantly affects radar visibility. This capability is vital for advancing both military and civilian radar technology applications, such as stealth design and radar system optimization.

5. CALCULATING RCS AND RADAR RANGE PROFILE

Radar Cross Section (RCS) analysis is a crucial aspect in the field of radar signal processing and target detection. Traditionally, RCS data has been analyzed in the frequency domain, providing insights into the reflectivity characteristics of targets at various frequencies. However, in real-time scenarios, the direct application of raw frequency domain RCS data is not practically meaningful. This limitation arises from the fundamental operational principles of modern radar systems, which primarily function in the time domain.

Real-time radar systems detect targets by transmitting pulses and analyzing the reflected signals. These radars emit short bursts of energy, known as pulses, towards the target and measure the time delay and strength of the reflected signals to determine the target's range, velocity, and other characteristics. This time domain approach allows for dynamic and instantaneous assessment of the target, accommodating the rapid changes in the target's position and movement.

In contrast, frequency domain RCS data, which represents the target's reflectivity as a function of frequency, lacks the temporal resolution needed for real-time target detection. Frequency domain analysis typically assumes a continuous wave (CW) radar operation, which does not align with the pulse-based nature of most practical radar systems. While frequency domain RCS can provide valuable information about the reflectivity of a target's surface, it falls short in simulating real-time scenarios where the timing and sequence of reflected signals are critical.

In frequency domain analysis, the target is often modeled by splitting it into small elements, known as meshes. The RCS contributions from each of these small pieces are summed to provide a total reflectivity value from a specific point of view. This cumulative approach gives a single RCS value representing the overall reflectivity of the target, but it lacks the detailed spatial and temporal information that is crucial for real-time radar applications.

To bridge the gap in achieving meaningful RCS results in the time domain, this thesis introduces a novel technique leveraging physical optics principles alongside direct simulation of pulse-based radar operations. Unlike traditional methods that rely on summed RCS data, this approach stores distinct reflectivity contributions from each mesh element, enabling granular and detailed radar signal analysis. These contributions are then processed in the time domain to simulate radar pulse interactions with the target, providing a more accurate representation of real-time radar-target dynamics.

This method combines frequency domain reflectivity analysis with time-domain radar simulations to achieve a comprehensive understanding of the target's spatial and temporal radar interaction. By focusing on individual mesh contributions, the proposed technique transcends the limitations of total reflectivity values, offering a detailed view from a single observation point. This thesis delves into the theoretical framework, computational methodologies, and practical implications of this approach, validating its effectiveness through detailed simulations and analyses. Practical applications, such as radar system design and stealth technology assessment, underline the method's potential for advancing time-domain RCS analysis. The detailed steps of this method are explained in the following sections. Frequency domain analysis, already covered in other sections, is excluded here to maintain focus on the novel time-domain methodology.

5.1 Setting System Parameters

In radar system design, setting the correct parameters is crucial for achieving the desired performance in terms of detection capability, range resolution, and robustness against noise. Each parameter plays a significant role in determining the overall performance of the radar system [11]. This section outlines the key parameters that need to be configured and their importance in radar system design.

5.1.1 Probability of detection

The probability of detection P_d is the likelihood that the radar system will correctly detect the presence of a target. A higher P_d indicates a better detection capability. It is a critical parameter in radar system design because it directly affects the reliability of the radar in identifying targets.

A high P_d is essential for applications where missed detections could have serious consequences, such as in military or aviation radar systems. However, achieving a high P_d typically requires a higher signal-to-noise ratio (SNR) and may demand more sophisticated signal processing techniques or higher transmit power.

5.1.2 Probability of false alarm

The probability of false alarm (P_{fa}) is the likelihood that the radar system will incorrectly declare a target's presence when there is none. A lower P_{fa} is desired to minimize false detections, which can lead to unnecessary actions or incorrect decisions.

Balancing P_{fa} and P_d is a critical aspect of radar design. Lowering P_{fa} usually requires increasing the detection threshold, which can reduce P_d. Therefore, an optimal balance must be achieved based on the application's requirements. Achieving a high P_d while maintaining a low P_{fa} is crucial for reliable radar operation. These parameters determine the sensitivity and selectivity of the radar system. A radar system with a high P_d and low P_{fa} can reliably detect targets with minimal false detections, enhancing its effectiveness in critical applications.

5.1.3 Maximum unambiguous range

The maximum unambiguous range is the maximum distance at which the radar can accurately determine the range of a target without ambiguity. This range is determined by the pulse repetition frequency (PRF) of the radar system:

$$R_{\max} = \frac{c}{2 \times \mathrm{PRF}} \tag{5.1}$$

The maximum unambiguous range sets the limit for the radar's effective range measurement. It is vital for applications requiring long-range target detection, such as air traffic control and early warning systems. However, increasing the maximum range may require compromising on the *PRF* and, consequently, the update rate and velocity resolution. A higher *PRF* allows for faster updates and better velocity measurement but reduces the maximum unambiguous range. Conversely, a lower *PRF* increases the maximum unambiguous range but can lead to ambiguity in target range measurement and poorer velocity resolution.

5.1.4 Range resolution

Range resolution is the radar system's ability to distinguish between two closely spaced targets. It is determined by the bandwidth of the transmitted pulse [12]:

$$\Delta R = \frac{c}{2 \times B} \tag{5.2}$$

where B is the bandwidth of the pulse. A higher bandwidth results in better range resolution, allowing the radar to distinguish between closely spaced targets. High range resolution allows the radar to distinguish between closely spaced targets, providing detailed target information and reducing target masking. It is essential for imaging radar systems and applications requiring fine target discrimination, such as automotive radar and synthetic aperture radar (SAR).

5.2 Pulse Waveform Generation Parameters

In radar systems, the pulse waveform is a crucial element that determines the radar's performance in terms of range resolution, target detection, and robustness to noise and interference. The choice of waveform and its parameters directly impacts the radar system's ability to detect and resolve targets [13]. This section outlines the key parameters and their significance in generating the radar pulse waveform.

5.2.1 Pulse bandwidth (B)

The bandwidth of the radar pulse is a critical factor that affects the range resolution:

$$B = \frac{c}{2 \times \Delta R} \tag{5.3}$$

Where ΔR is the range resolution, c is the speed of light, and B is the bandwidth of the pulse. A wider bandwidth results in better range resolution, allowing the radar to distinguish between targets that are close to each other. This is essential for applications requiring precise target localization, such as imaging radar and automotive radar systems. However, generating and processing wideband signals requires more advanced hardware and signal processing capabilities.

5.2.2 Pulse width (τ)

The pulse width determines the duration of the radar pulse. It is inversely related to the pulse bandwidth:

$$\tau = \frac{1}{B} \tag{5.4}$$

The pulse width influences the energy of the transmitted pulse and, consequently, the signal-to-noise ratio (SNR). Longer pulses contain more energy, improving the SNR and detection performance, especially in low SNR environments. However, longer pulses can reduce range resolution and increase susceptibility to range ambiguities.

5.2.3 Pulse repetition frequency (PRF)

The pulse repetition frequency (PRF) defines the rate at which pulses are transmitted. It affects the maximum unambiguous range and the radar's ability to measure target velocity:

$$PRF = \frac{c}{2 \times R_{\max}} \tag{5.5}$$

A higher PRF improves Doppler resolution and allows for better velocity measurement, which is crucial for tracking fast-moving targets. However, it limits the maximum range. A low PRF extends the range but can introduce ambiguities in range measurement and degrade velocity resolution.

5.2.4 Sampling rate (F_S)

The sampling rate determines the rate at which the radar signal is sampled. It must be sufficiently high to capture the details of the pulse waveform and to prevent aliasing:

$$F_S \geq 2 \times B \tag{5.6}$$

Where F_S is the sampling rate, and B is the bandwidth of the pulse. A high sampling rate ensures accurate representation of the radar signal, preventing aliasing and preserving the signal's details. This is important for effective signal processing and accurate target detection.

In this simulation, the sampling rate is set to ten times the pulse bandwidth to ensure high fidelity in signal representation. This high sampling rate ensures that the radar signal is accurately captured and processed.

5.3 Radar System Parameters

5.3.1 Receiver operating characteristics (ROC) and (SNR) calculation

The Receiver Operating Characteristics (ROC) curve is a vital tool for analyzing the performance of radar systems. It provides a graphical representation of the trade-off between the probability of detection (P_d) and the probability of false alarm $(P_f a)$ across varying signal-to-noise ratios (SNRs). This curve is crucial for understanding how changes in SNR impact the radar system's ability to detect targets reliably while minimizing false alarms.

ROC curves help radar system designers to visualize and quantify the trade-offs between detection performance and false alarm rates [14]. A higher SNR generally improves the probability of detection but may also require higher transmit power or more advanced signal processing techniques. Conversely, lowering the SNR threshold can increase the false alarm rate, leading to potential operational issues. By plotting ROC curves as shown in the Figure 5.1 designers can determine the optimal operating point for a radar system, ensuring that it meets specific performance requirements while balancing power, complexity, and other constraints.

To generate ROC curves, the SNR is varied, and the resulting probabilities of detection and false alarm are plotted. This is done using statistical models of the radar signal and noise characteristics. The ROC curves show that to achieve a high P_d with a low $P_f a$, a high SNR is required. However, achieving such high SNR in practical scenarios may be challenging. Therefore, techniques like pulse integration, where multiple pulses are combined to improve the effective SNR, are employed. This can significantly reduce the required SNR for achieving the desired detection performance.

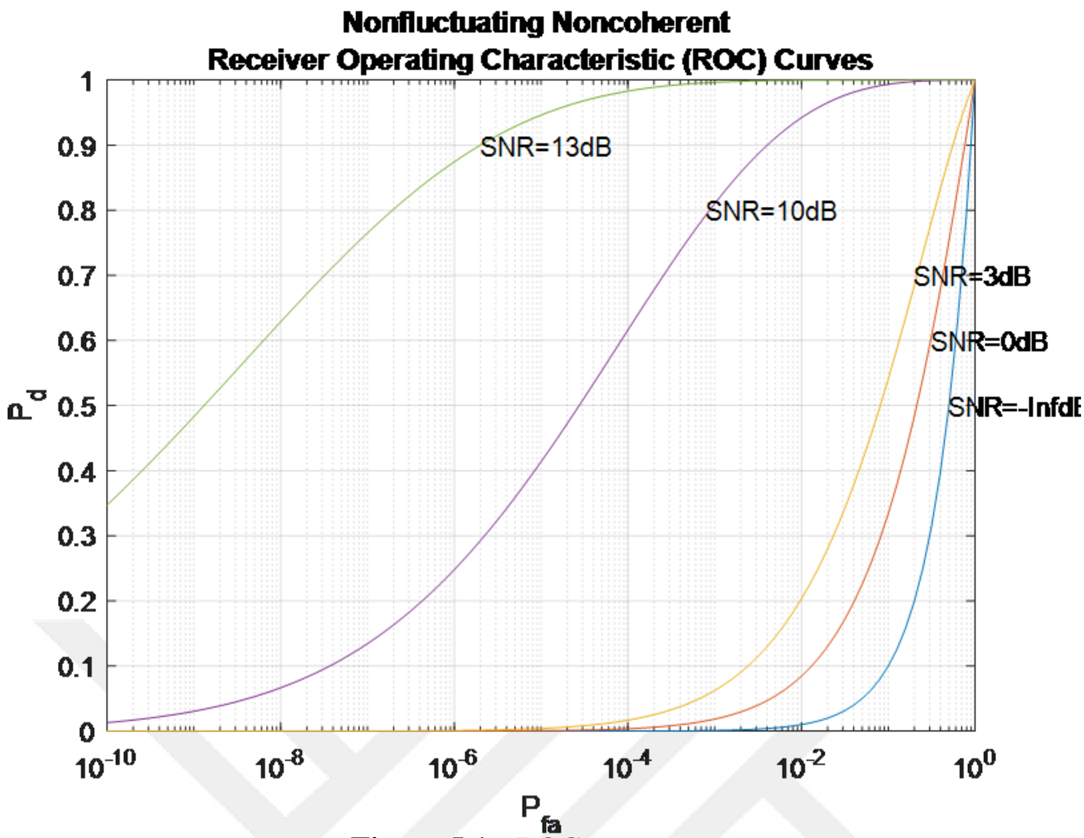

Figure 5.1 : ROC curve.

5.3.2 Shnidman's equation

Shnidman's equation is a powerful tool used in radar system design to relate the signal-to-noise ratio (SNR), probability of detection (P_d), probability of false alarm , and the number of integrated pulses [15]. This equation is particularly useful for systems using linear frequency modulation (LFM) waveforms due to its ability to account for the nonfluctuating nature of these signals and the coherence properties of pulse integration.

Shnidman's equation is given by:

$$\mathrm{SNR}_{\mathrm{min}} = \frac{Q^{-1}(P_d) - Q^{-1}(P_{fa})}{\sqrt{N}} \tag{5.7}$$

where SNR_min is the minimum required SNR for defined P_d and P_{fa} and N is the number of pulses.

Shnidman's equation is particularly advantageous for radar systems employing LFM waveforms because it effectively handles the coherent integration of multiple pulses. LFM waveforms are commonly used due to their high range resolution and robustness against noise.

By integrating multiple pulses, radar systems can achieve a higher effective SNR, reducing the required peak transmit power and improving detection performance.

5.3.3 Practical considerations for peak transmit power calculation

The peak transmit power is a critical parameter that directly influences the radar system's detection range and performance. The radar range equation is used to calculate the necessary peak power, considering factors such as maximum unambiguous range, required signal-to-noise ratio (SNR) at the receiver, pulse width, and target characteristics.

The peak transmit power can be calculated as:

$$P_t = \frac{(4\pi)^3 P_n R_{\max}^4 \mathrm{SNR}}{G_t G_r \sigma \lambda^2} \tag{5.8}$$

where P_t is the peak transmit power, P_n is the noise power at the receiver, $R_{\max}$ is the maximum unambiguous range,SNR is the required signal-to-noise ratio, G_t and G_r are the transmitter and receiver gains, σ is the radar cross-section (RCS) of the target and λ is the wavelength of the radar signal.

By integrating multiple pulses and optimizing the SNR using Shnidman's equation, the radar system can achieve better detection performance with reduced power requirements. This balance between power, SNR, and pulse integration is crucial for designing efficient and effective radar systems.

5.4 System Simulation and Signal Processing

This section outlines the steps involved in simulating a radar system, synthesizing radar signals, and processing these signals to analyze the system's performance. The code provided performs a comprehensive radar simulation, including signal transmission, propagation, reflection, reception, and subsequent signal processing.

5.4.1 Transmitter setup

The transmitter is configured with specific gain and peak power settings, which are crucial for determining the strength and quality of the transmitted radar pulses. The transmitter gain amplifies the radar signal before it is radiated by the antenna, while the peak power determines the maximum power of the radar pulse. The peak power is particularly important for extending the radar's detection range, as it influences the signal-to-noise ratio (SNR) at the receiver.

5.4.2 Antenna configuration

An isotropic antenna is defined for both transmission and reception. An isotropic antenna radiates power uniformly in all directions, simplifying the antenna design for this simulation. The antenna operates over a specified frequency range, ensuring effective transmission and reception of signals within the radar system's operational bandwidth. In this simulation, the antenna is stationary, which simplifies the analysis and focuses on the signal processing aspects of the radar system.

5.4.3 Platform and motion simulation

The positions and velocities of the sensor (radar) and targets are defined and updated during the simulation. This step is essential for accurately modeling the movement of both the radar platform and the targets. The radar sensor and targets are modeled using platforms that can have their positions and velocities updated dynamically. Although the sensor and targets are stationary in this particular simulation, the framework allows for modeling moving platforms and targets, providing flexibility for more complex scenarios.

5.4.4 Radiator and collector configuration

The radiator and collector are set up to handle the transmission and reception of signals through the antenna. The radiator directs the transmitted radar signal towards the targets. It takes into account the antenna's radiation pattern and ensures that the signal is appropriately shaped for effective transmission. The collector receives the reflected signals from the targets. It captures the signals returned from the target reflections, which are then processed to extract useful information about the target's location and velocity.

5.4.5 Target and channel modeling

The targets are modeled with specific radar cross-section (RCS) values, and the propagation channel is configured to simulate the transmission of radar pulses through free space. The targets are defined using the Swerling model, which characterizes statistical variations in RCS. This model is important for simulating realistic target behavior, as it accounts for fluctuations in the reflected signal strength. The free space channel models the two-way propagation of radar pulses. This involves simulating the travel of radar pulses from the radar to the targets and back, accounting for factors like signal attenuation and propagation delay.

5.4.6 Signal synthesis

Signal synthesis involves generating a data matrix that represents the received signals as a function of fast time and slow time. This matrix is critical for analyzing the radar's performance over multiple pulses. Linear Frequency Modulated (LFM) pulse signal is used for described radar signal processing system. The core of the signal synthesis involves a loop that simulates the transmission, reflection, and reception of radar pulses over multiple cycles.

5.4.6.1 Sensor and target position update

Positions are updated to reflect any motion of the sensor and targets. Target Angle Calculation: Angles of the targets relative to the sensor are calculated to determine the direction of transmission and reception.

5.4.6.2 Target angle calculation

Angles of the targets relative to the sensor are calculated to determine the direction of transmission and reception.

5.4.6.3 Pulse propagation and reflection

Radar pulses are transmitted towards the targets, propagate through the environment, reflect off the targets, and return to the radar.

5.4.6.4 Signal storage

The transmitted and reflected signals are stored for subsequent analysis. This step is crucial for comparing the transmitted signals with the received signals to extract information about the targets.

5.4.7 Noise power at receiver

Accurate calculation of noise power and setting an appropriate detection threshold are essential for distinguishing between actual target signals and noise. Based on the receiver's noise figure and bandwidth, the noise power is computed using the formula below:

$$P_n = kTB \tag{5.9}$$

where P_n is the noise power, k is Boltzmann's constant, T is the system temperature in Kelvin, B is the receiver bandwidth.

5.4.8 Matched filtering

Matched filtering is a signal processing technique used to maximize the SNR [16] of the received signal by convolving it with a time-reversed and conjugated copy of the transmitted waveform. This process enhances the detectability of the radar signals and significantly improves range resolution.

The matched filter is applied to optimize the detection of the transmitted radar pulse within the received signal. By maximizing the SNR, matched filtering helps in distinguishing the target echoes from the background noise, making it easier to detect the presence of targets. The matched filter is designed using the coefficients of the transmitted linear FM (LFM) waveform. This filter matches the shape of the transmitted pulse, which allows it to coherently integrate the energy of the pulse over its duration, resulting in a significant SNR improvement. The matched filter provides a processing gain that enhances the detection threshold. The received pulses are convolved with the matched filter, and the filter gain is accounted for to adjust the detection threshold. This step ensures that the radar system can reliably detect weak target signals. One of the effects of matched filtering is the introduction of a delay, which misaligns the peak SNR output with the true target locations. To correct this, the output of the matched filter is shifted forward, and zeros are padded at the end. This compensation ensures that the peaks in the filtered signal accurately correspond to the actual target positions, preserving the spatial integrity of the radar returns.

5.4.9 Range normalization with time-varying gain

After matched filtering, the received signal power is inherently range-dependent. Closer targets produce stronger returns, which can overshadow weaker signals from distant targets. To ensure a uniform detection threshold across all ranges, a time-varying gain is applied to normalize the signal. The application of range normalization is essential to compensate for the free space path loss, which causes signal attenuation over distance. By normalizing the received signals, the radar system can apply a consistent detection threshold, improving the reliability of target detection across all ranges. Range gates corresponding to each signal sample are calculated based on the propagation speed of the signal and the fast time grid. This calculation determines the exact distance at which each radar return is received, allowing for precise range estimation. The free space path loss for each range gate is computed, and a time-varying gain is applied to the received pulses. This step adjusts the signal strength as if all returns were from the same reference range, typically the maximum detectable range. This compensation ensures that the radar returns are consistent, regardless of the target's distance from the radar. The time-varying gain equalizes the received signal power across different ranges [17], allowing for the use of a constant detection threshold. This step is crucial for maintaining detection sensitivity across the entire range of the radar system, ensuring that distant targets are not missed due to weaker returns.

5.4.10 Coherent integration

integration further enhances the SNR by summing the complex-valued received signals over multiple pulses, improving the radar's ability to detect targets. Coherent integration is used to accumulate the signal energy over several pulses while maintaining phase coherence. This technique significantly improves the SNR [18] by averaging out the noise and reinforcing the target echoes. It is particularly effective for detecting weak signals that may not be discernible in a single pulse.

Coherent integration involves summing the complex-valued received pulses. This method preserves the phase information, allowing for constructive interference of the signal components, which enhances the overall SNR. By integrating over multiple pulses, the radar system can detect weaker targets and achieve better range resolution.

The integrated pulses are plotted against the detection threshold. This step demonstrates the improvement in SNR and the enhanced ability to detect targets after coherent integration. The visual comparison of integrated pulse power with the detection threshold illustrates the effectiveness of coherent integration in boosting the radar's detection performance.

Peaks in the integrated signal, corresponding to potential targets, are identified using a peak detection algorithm. The range estimates of these detected peaks are compared with the true target ranges to evaluate the accuracy of the radar system. This step is critical for validating the radar system's ability to accurately estimate target ranges and ensures that the integrated signals are correctly interpreted.

5.4.11 High resolution range profile

The High-Resolution Range Profile (HRRP) provides a detailed, high-resolution representation of a target's structure by coherently integrating the received radar pulses over multiple cycles. This integration preserves the phase information of the signal, enhancing the signal-to-noise ratio (SNR) and allowing for fine-grained analysis of the target [19]. To focus on the target of interest, a specific range window is defined. This window isolates the relevant portion of the HRRP that corresponds to the target, filtering out irrelevant background noise and other signals. The width of the range window is carefully selected based on the expected size of the target and the radar's resolution capabilities.

Estimating the physical dimensions of the target involves analyzing the HRRP to detect peaks that correspond to different reflective surfaces of the target. These peaks provide critical information about the target's size and shape.

The HRRP is segmented into range bins, each representing a specific distance from the radar. These bins help in mapping the time-domain reflections to spatial dimensions, making it easier to estimate the physical size of the target.

Peaks within the HRRP are detected using adaptive thresholding techniques. These peaks represent strong reflections from the target's surfaces and are indicative of distinct structural features. The detection algorithm uses parameters such as minimum peak height, prominence, and distance between peaks to ensure that only significant reflections are considered.

The thresholds for peak detection are dynamically calculated using statistical measures of the HRRP. Parameters like the interquartile range (IQR) help in setting robust thresholds that adapt to the noise characteristics and signal variations. This adaptive approach ensures that the peak detection is resilient to fluctuations in the signal.

Once the peaks are detected, the distances between the first and last significant peaks are used to estimate the physical dimensions of the target. This method leverages the fact that different parts of the target will reflect radar signals at different times, corresponding to their spatial separation.

The range estimate is determined by locating the first peak that exceeds the threshold. The corresponding range bin provides the estimated distance to the target. This method ensures that the most significant target reflection is accurately identified and measured.

6. APPLICATIONS

In this section, three targets are analyzed at different frequencies to demonstrate the effectiveness of the proposed methodology. Initially, the calculated RCS results, obtained by summing the contributions from all illuminated triangles (as done in traditional methods), are compared with results from a commercial software tool to validate the accuracy of the implementation. This validation ensures the reliability of the proposed calculation method by showing its agreement with established results.

Following this validation step, the focus shifts to a novel aspect of the methodology. Unlike traditional approaches that sum contributions to produce a single RCS value for a specific viewing angle, this work models individual illuminated triangles as independent scattering elements (or "targets") within the simulation. This approach allows for the simulation of a real-time radar system interacting with the target, where each triangle's RCS is treated as an individual source of scattered fields. The scattered fields from these triangles are then used to simulate the radar's received signal.

This approach effectively bridges the gap between classical RCS calculation and time-domain radar simulation. Instead of viewing the target as a single reflectivity source, this method captures the detailed spatial and temporal interactions between the radar and individual components of the target. By incorporating these individual contributions, the simulation mimics how a real-time radar system would process reflected signals in practice.

The subsequent steps, such as applying matched filtering, range normalization, and coherent integration, follow this fundamental distinction. These steps further process the received signal to enhance the signal-to-noise ratio and extract key radar features, such as high-resolution range profiles (HRRP) and target detection. The results of this process provide a clearer and more realistic representation of the radar's interaction with the target, illustrating the advantages of this method over traditional RCS calculations.

The parameters of the radar system modeled in this work are listed in Table 6.1

Table 6.1 : Radar system parameters.

Parameter	Value
Probability of Detection (P_d)	0.9
Probability of False Alarm (P_{fa})	10^{-6}
Maximum Unambiguous Range ($R_{\max}$)	9 km
Range Resolution (ΔR)	1 meter
Propagation Speed (c)	3×10^8 m/s
Pulse Bandwidth (B)	225 MHz
Pulse Width (τ)	890 μs
Pulse Repetition Frequency (PRF)	17 kHz
Sampling Rate (F_s)	2.25 GHz
Waveform	LFM
Noise Bandwidth (NB)	225 MHz
Receiver Gain (G_r)	30 dB
Receiver Noise Figure (NF)	0 dB
Transmitter Gain (G_t)	30 dB
Transmitter Peak Power	12 kW
Signal to Noise Ratio (SNR)	7.3900

6.1 PEC Missile

The analyses are performed for two different operation frequencies as 2GHz and 4GHz.

6.1.1 Analysis for 2GHz

The missile target, depicted in Figure 6.1, is characterized by its physical dimensions, including overall size, surface area, and the range of triangle areas used in the mesh. The detailed properties of the structure are listed in Table 6.2.

Table 6.2 : Missile parameters.

Parameter	Value
Model name	missile
Number of triangles	2690
Number of points	1347
X Size	7.72 m
Y Size	3 m
Z Size	7.72 m
Total area	24.9984 m^2
Max triangle area	0.019932 m^2
Min triangle area	3.3816×10^{-5} m^2

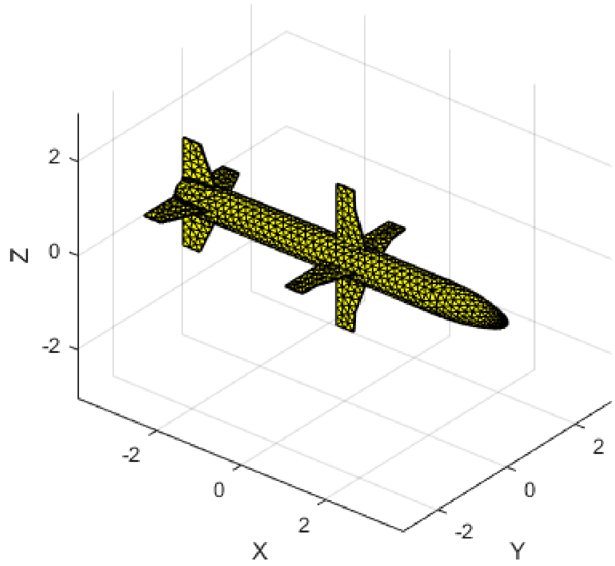

Figure 6.1 : Missile mesh model.

Two series of analyses were conducted for Radar Cross Section (RCS) results validation. For the first analysis, the azimuth angle (θ) was held constant at 90°, while the elevation angle (ϕ) was varied from 0° to 180°. The angular configuration for this case is depicted in Figure 6.2.

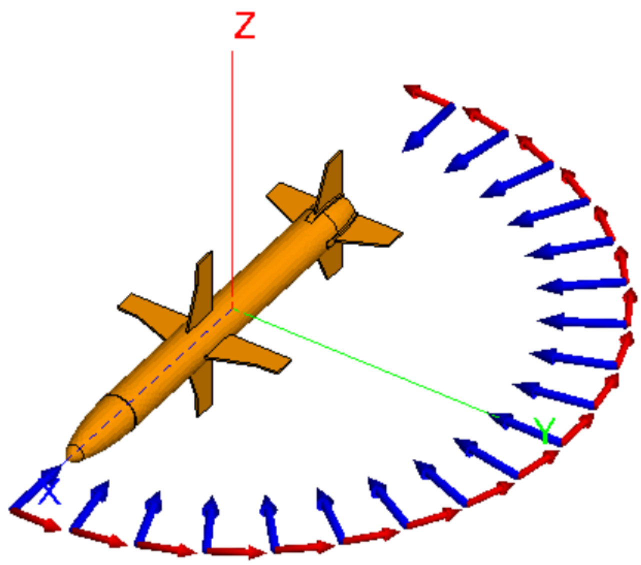

Figure 6.2 : θ=90°, ϕ=0° – 180°.

To validate the RCS results obtained from the proposed algorithm, the same analyses were performed using the commercial software FEKO. The RCS comparison results of first analysis for VV and HH polarizations are presented in Figures 6.3 and 6.4, corresponding to constant azimuth and varying elevation.

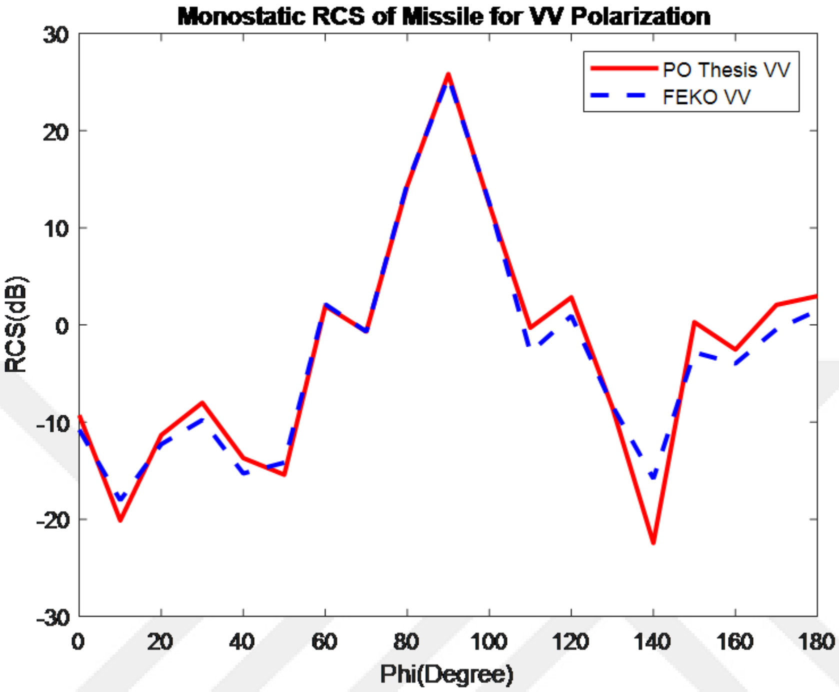

Figure 6.3 : Monostatic RCS of missile for VV polarization at different ϕ angles.

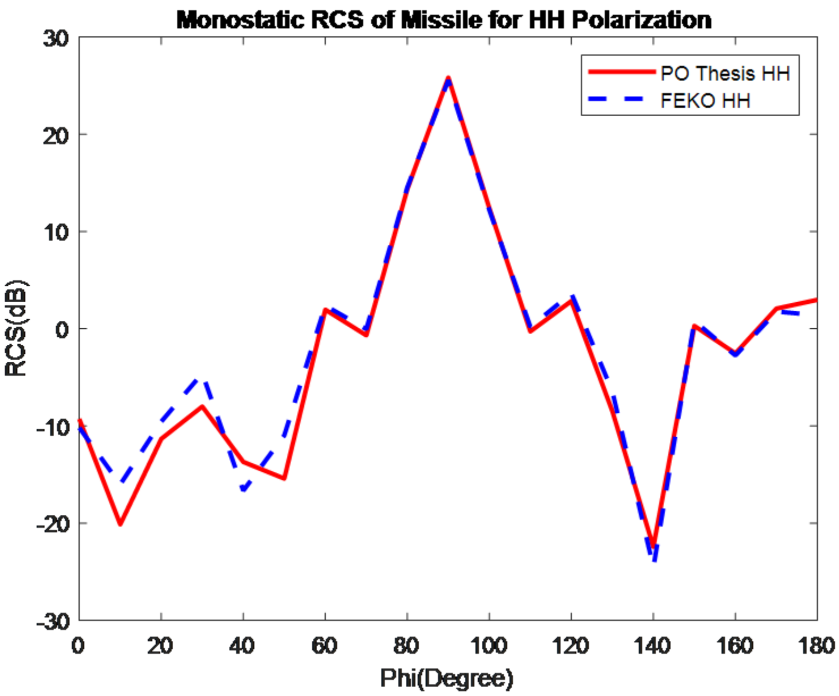

Figure 6.4 : Monostatic RCS of missile for HH polarization at different ϕ angles.

For second analysis, the elevation angle (ϕ) was held constant at 0°, and the azimuth angle (θ) was varied similarly from 0° to 180°. The angular configuration for this case is shown in Figure 6.5.

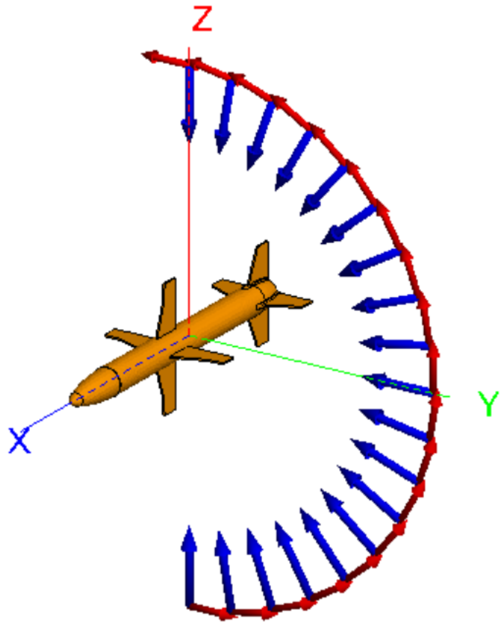

Figure 6.5 : ϕ=90°, θ=0° – 180°.

Similarly, the RCS comparison results of second analysis for HH and VV polarization are provided in Figures 6.6 and 6.7. These graphs demonstrate the agreement between the proposed algorithm and FEKO, validating the accuracy and reliability of the designed algorithm. Hence, the individual RCS of the triangles can be used as inputs for the defined radar system, which makes possible to obtain more informations about the target such as size and position.

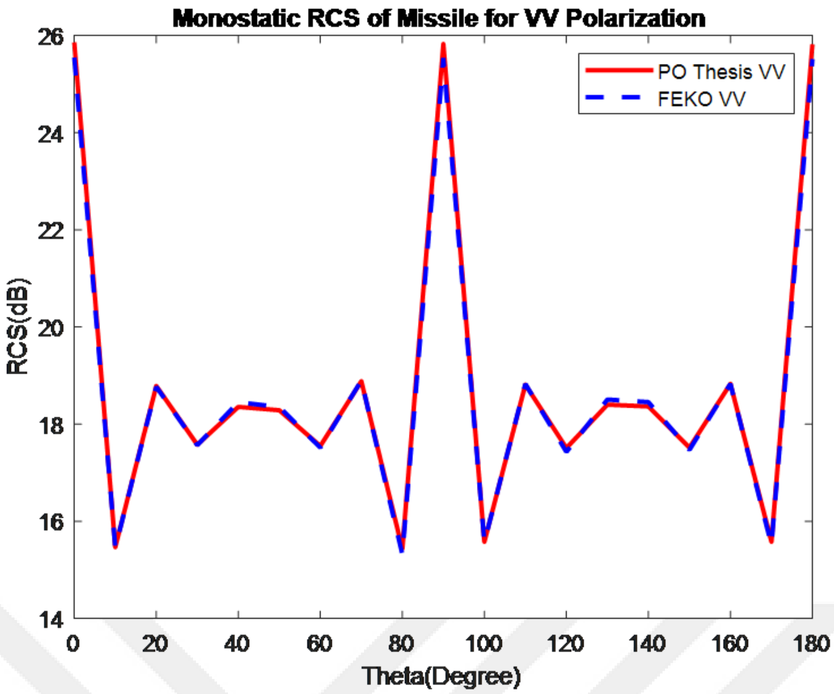

Figure 6.6 : Monostatic RCS of missile for VV polarization at different θ angles.

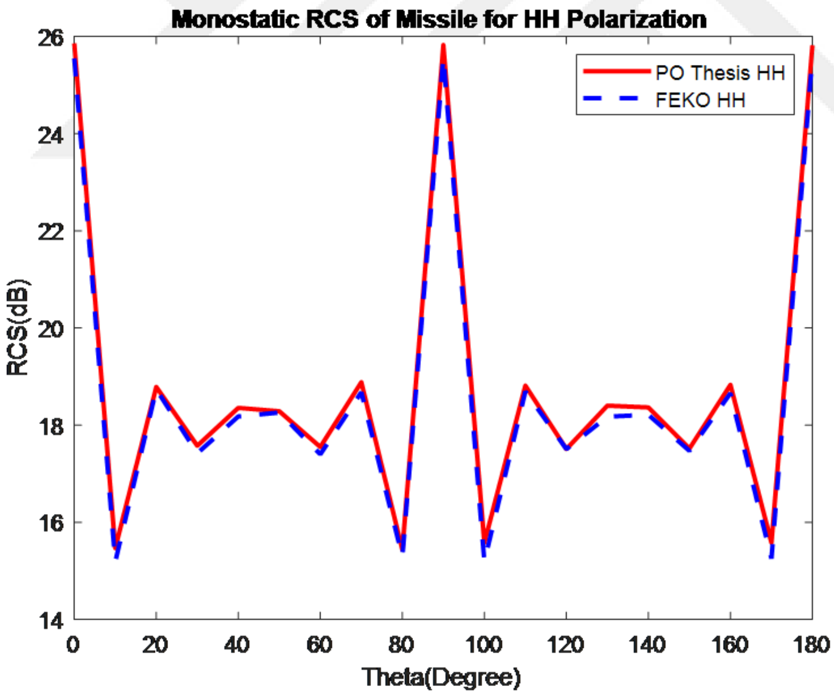

Figure 6.7 : Monostatic RCS of missile for HH polarization at different θ angles.

After validating the RCS analysis, the target can be further studied from a specific point of view to understand how it appears to radar from that angle. For example, setting $\theta = 90^\circ$ and $\phi = 0^\circ$ provides one such perspective. From this viewpoint, the Figure 6.8 illustrates the surface currents induced on the target, which are essential for understanding how the target scatters radar signals. The RCS values of the mesh elements that are seen from the chosen perspective can be further utilized to extract the radar range profile, providing detailed insight into the target's radar signature along this line of sight.

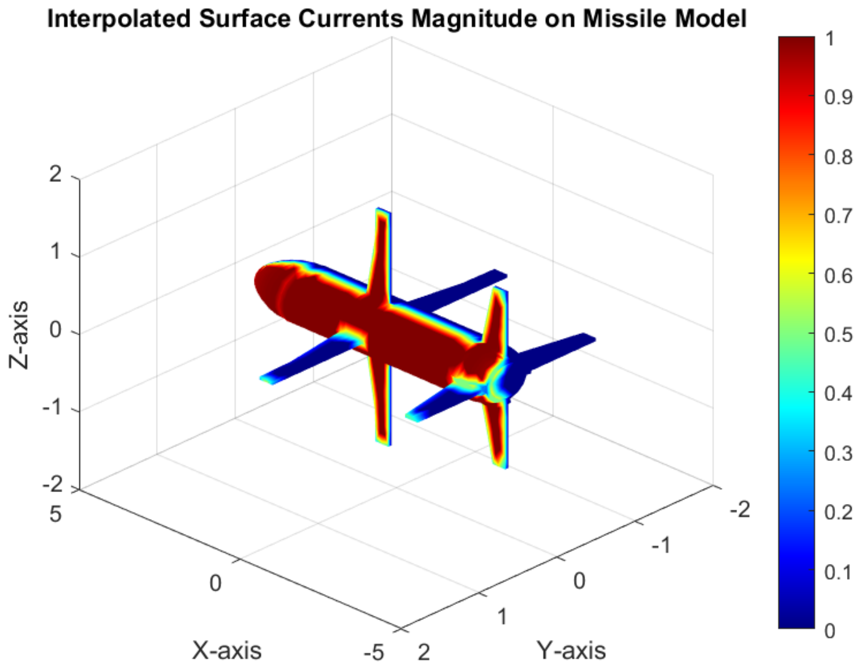

Figure 6.8 : Surface currents of missle.

Ten radar pulses are generated using a predefined waveform. These pulses are amplified by the transmitter, directed at the target by the radiator, and propagated through free space while accounting for the relative motion between the sensor and the target. This process simulates real radar operations, ensuring proper generation, amplification, direction, and propagation of pulses.

The transmitted pulses hit the target and are reflected based on the target's radar cross-section (RCS), which determines how much of the radar signal is scattered back. The reflected signals are captured by the radar's receiving antenna and processed by the receiver, which includes amplification and noise considerations. This processing ensures the received signals accurately represent the interaction between the transmitted pulse and the target, incorporating factors such as target reflectivity and signal attenuation during propagation. The resulting transmitted, reflected, and received signals are illustrated in the Figure 6.9

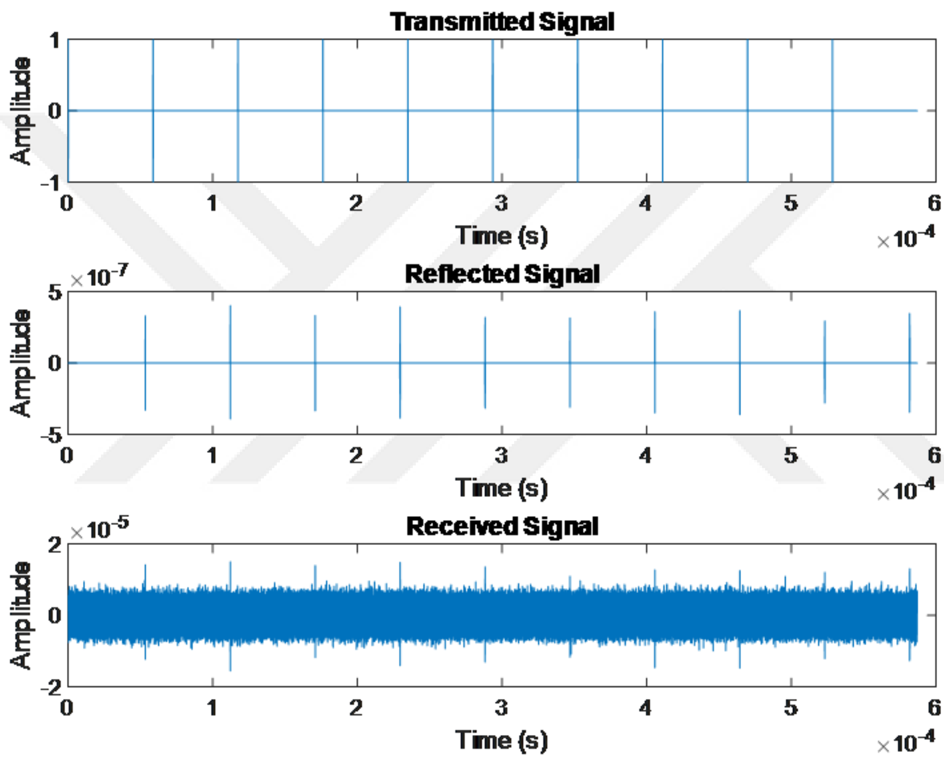

Figure 6.9 : Transmitted, reflected and received signals.

Figure 6.10 shows only first pulses for detailed examination. It can be seen that reflected signal has a time delay and gain loss comparing with transmitted signal, which is an expected issue.

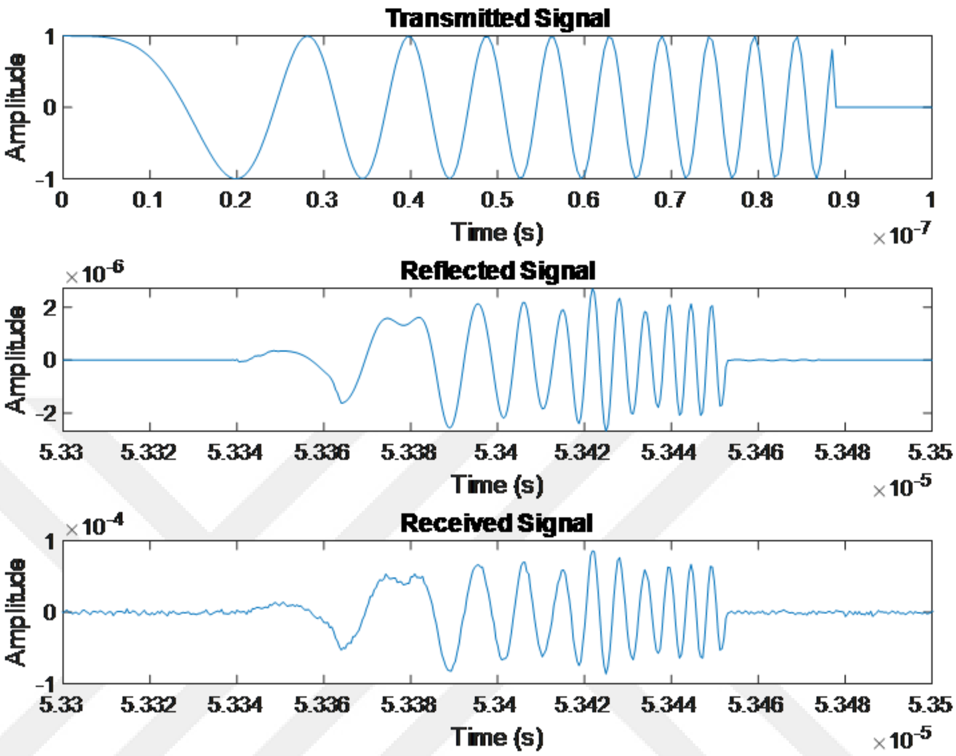

Figure 6.10 : First pulses that are transmitted, reflected and received.

The detector system is designed to determine whether a received signal corresponds to a real target or is just noise. It does this by comparing the signal power to a predefined threshold. In radar applications, this threshold is carefully set to ensure that the probability of false alarm (P_{fa}) remains below a predetermined level. This ensures reliable operation even in noisy environments. Assuming white Gaussian noise and coherent detection, the signal power threshold is calculated to be -105.3095 dBW. The first two received pulses, along with the applied threshold, are presented in the Figure 6.11.

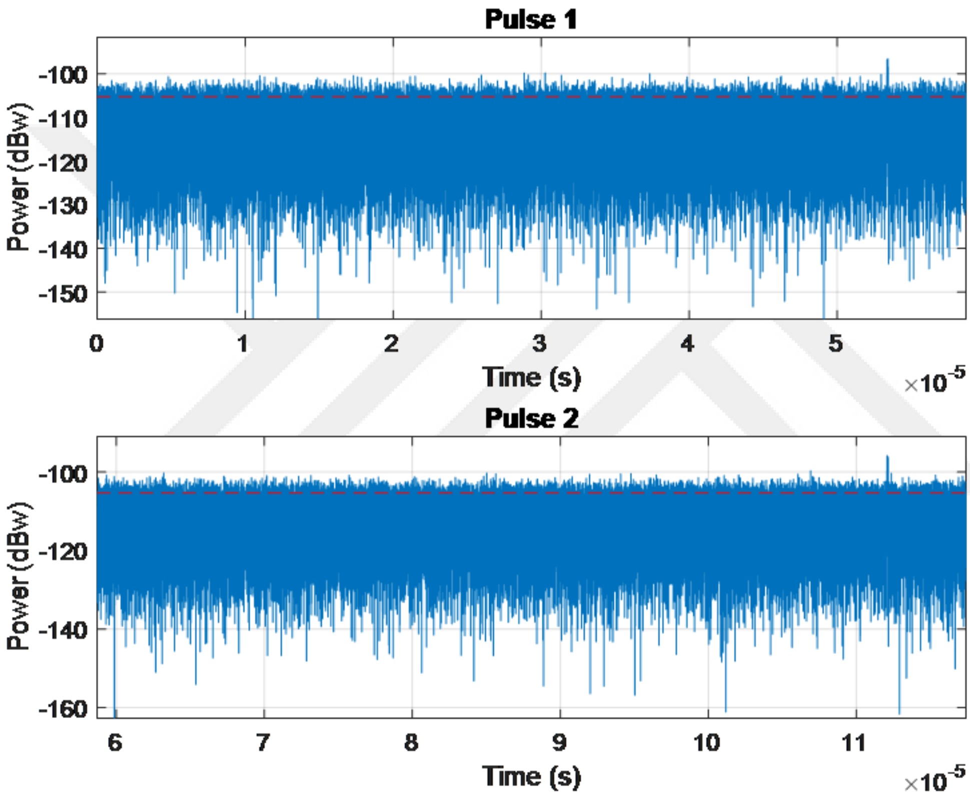

Figure 6.11 : The first two received pulses with applied threshold.

After receiving the pulses, a matched filter is applied to enhance the signal-to-noise ratio (SNR). This filter provides a processing gain, which also improves the detection threshold. The filter operates by convolving the received signal with a local, time-reversed, and conjugated copy of the transmitted waveform. The result of this process is an increased threshold, which is recalculated as -60 dBW. The first two received pulses, along with the applied new threshold, are presented in the Figure 6.12.

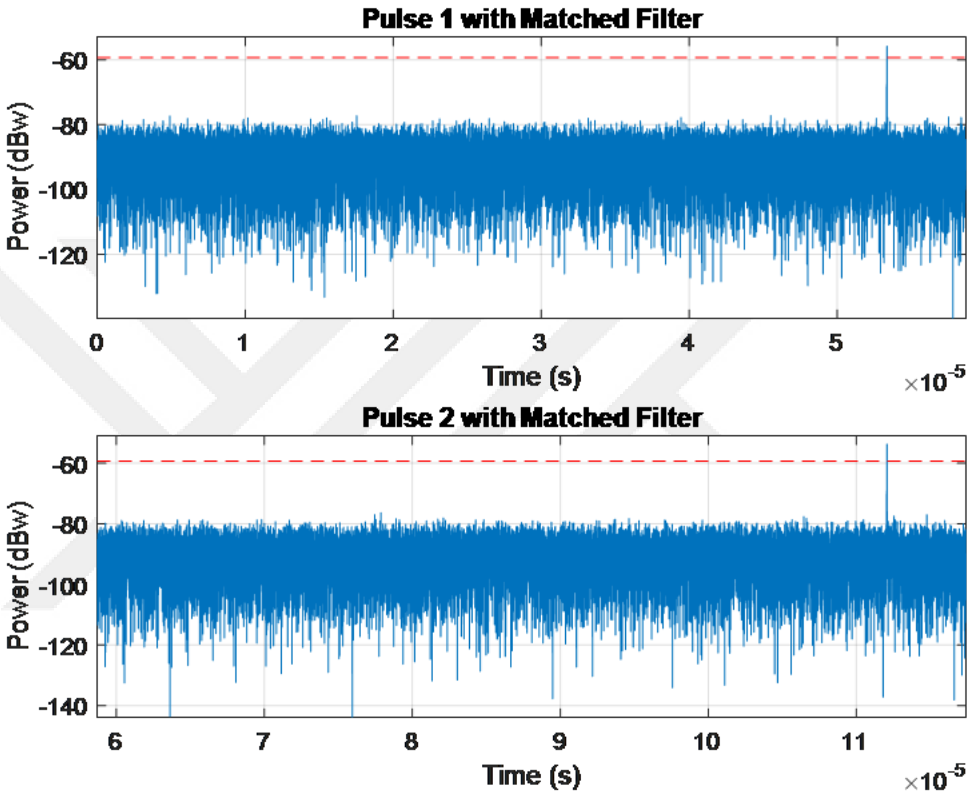

Figure 6.12 : Application of matched filter.

The matched filter improves the SNR significantly. However, since the received signal power decreases with increasing range, the return signal from a nearby target remains much stronger than that from a distant target. Noise from closer range bins can exceed the detection threshold, potentially masking signals from farther targets.

To address this imbalance and ensure equal detection sensitivity across all ranges, a process known as range normalization is applied. This compensation involves calculating the range gates corresponding to each signal sample and determining the free-space path loss for each range gate. Using this information, a time-varying gain is applied to the received pulses as shown in the Figure 6.13 This adjustment ensures that all target returns appear as if they originate from the same reference range, typically the maximum detectable range, effectively equalizing the signal strength across varying distances.

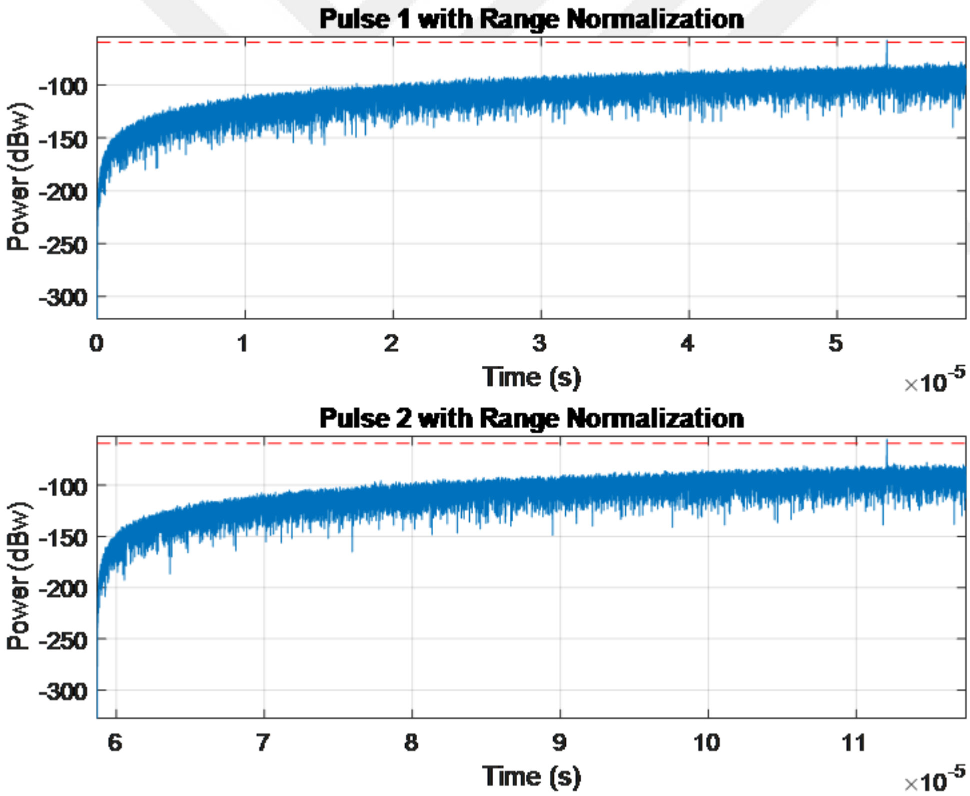

Figure 6.13 : Range normalization.

Then, coherent integration is applied to range-normalized pulses as shown in the Figure 6.14 to enhance the signal-to-noise ratio (SNR). After this process, only the segments of the signal that exceed the calculated detection threshold are selected for creating the High Resolution Range Profile (HRRP).

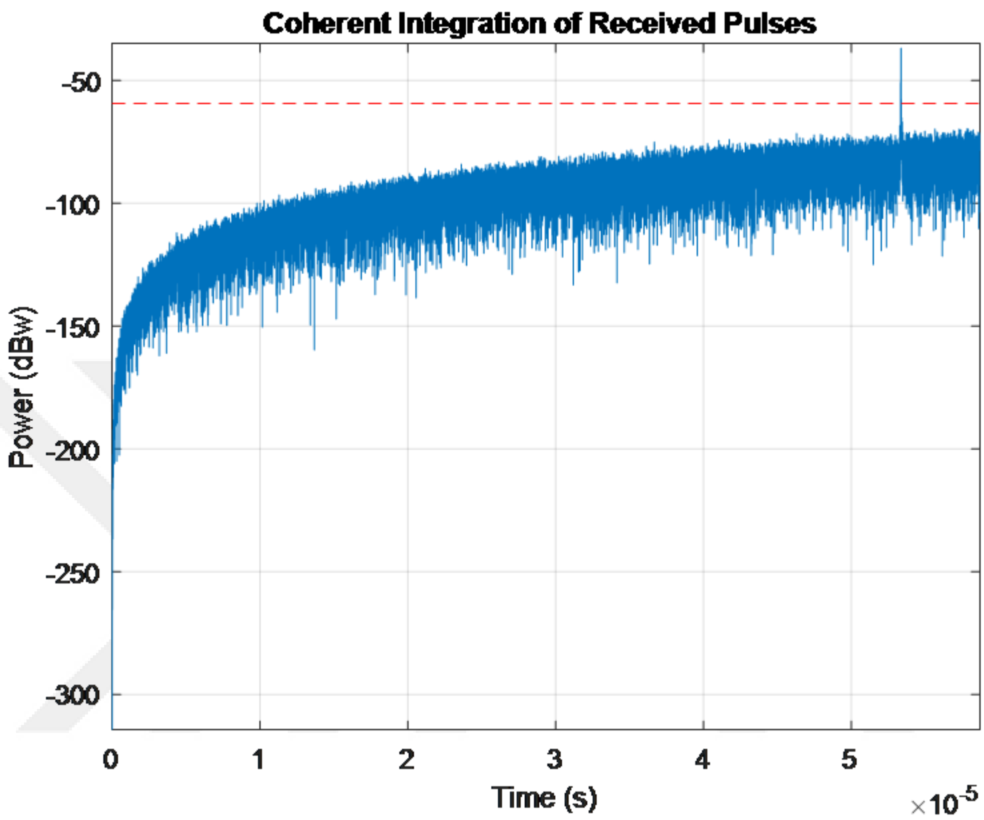

Figure 6.14 : Coherent integration of received pulses.

For detection of the range of the target, a uniform time grid is created based on the sampling rate and the pulse repetition frequency. This time grid represents the fast time within each pulse. The corresponding range bins are then calculated using the speed of light. These range bins represent the distance from the radar to the target for each sample in the integrated pulse. The largest peak above the threshold is dentified as the target's reflection. The figure Figure 6.15 shows the corresponding result. The range of the target is estimated based on the location of this peak in the range bins. The estimated target range is 7997.4 meters and real target range is 7997.3 meters.

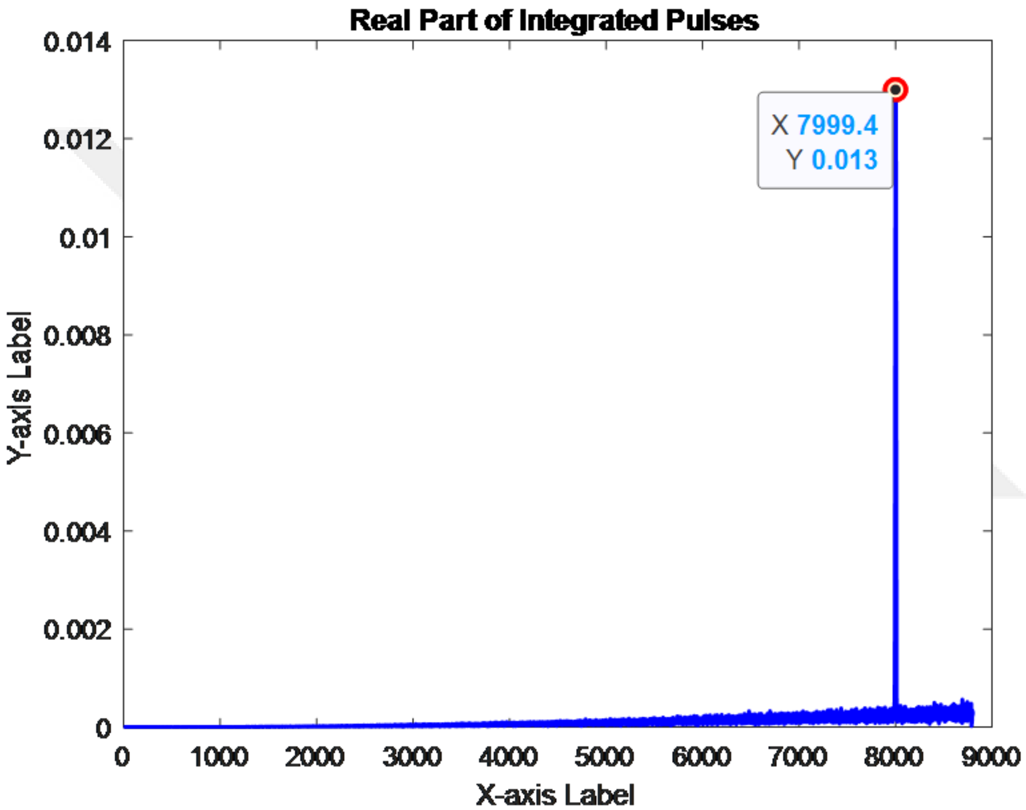

Figure 6.15 : Real part of the integrated pulses.

The HRRP is generated within a predefined range window, set to 50 meters, which specifies the segment of the integrated pulse to be analyzed. The number of samples in this range window is calculated based on the radar's sampling frequency (F_s) and the speed of light (c), ensuring that the HRRP accurately corresponds to the selected range window. To extract the HRRP, the maximum value of the absolute integrated pulse is identified, representing the most significant reflection likely originating from the target. The HRRP is centered around this peak value within the defined range window. By focusing on this peak-centered segment, the HRRP highlights the most prominent features of the target's reflections. The plotted HRRP for the target is given in the Figure 6.16.The estimated size of the target is calculated based on the distance between the detected peaks. The calculated physical size is approximately 8.2 meters. Which is a good result comparing with the actual size, 7.2 meters, and considering 1 meters range resolution.

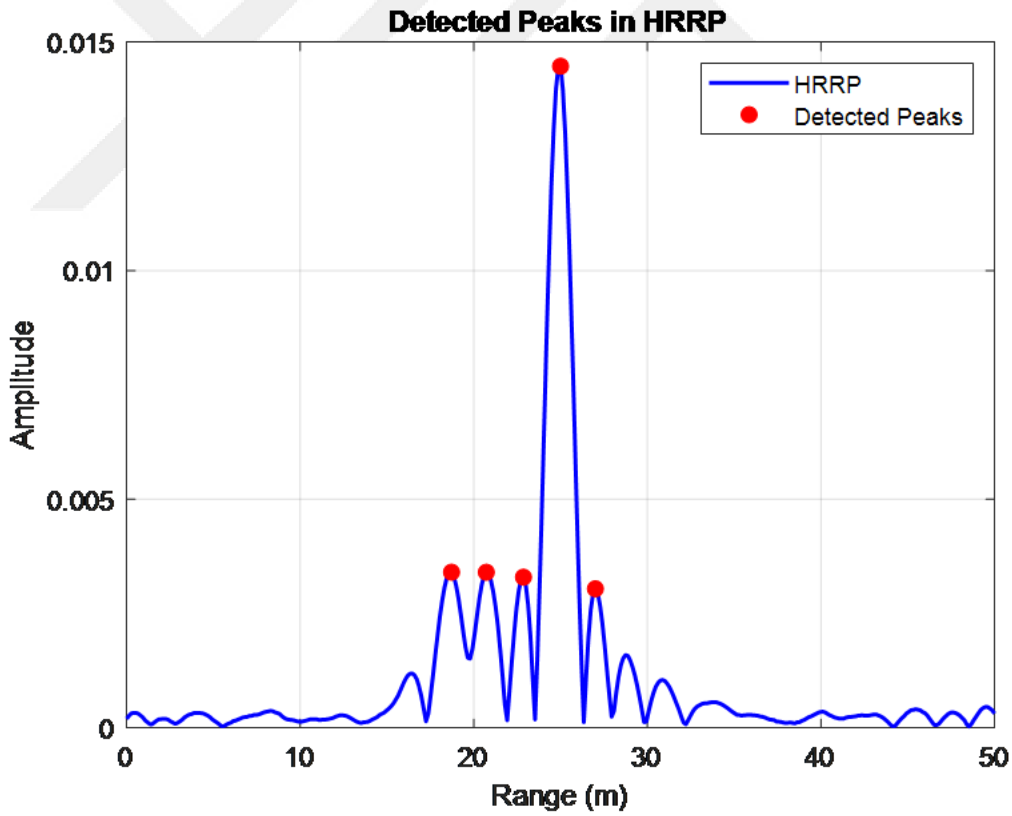

Figure 6.16 : Detected peaks in HRRP.

6.1.2 Analysis for 4GHz

For the 4 GHz analysis, a denser mesh was utilized for the missile geometry. The details of the mesh are shown in Figure 6.17, with key parameters summarized in Table 6.5.

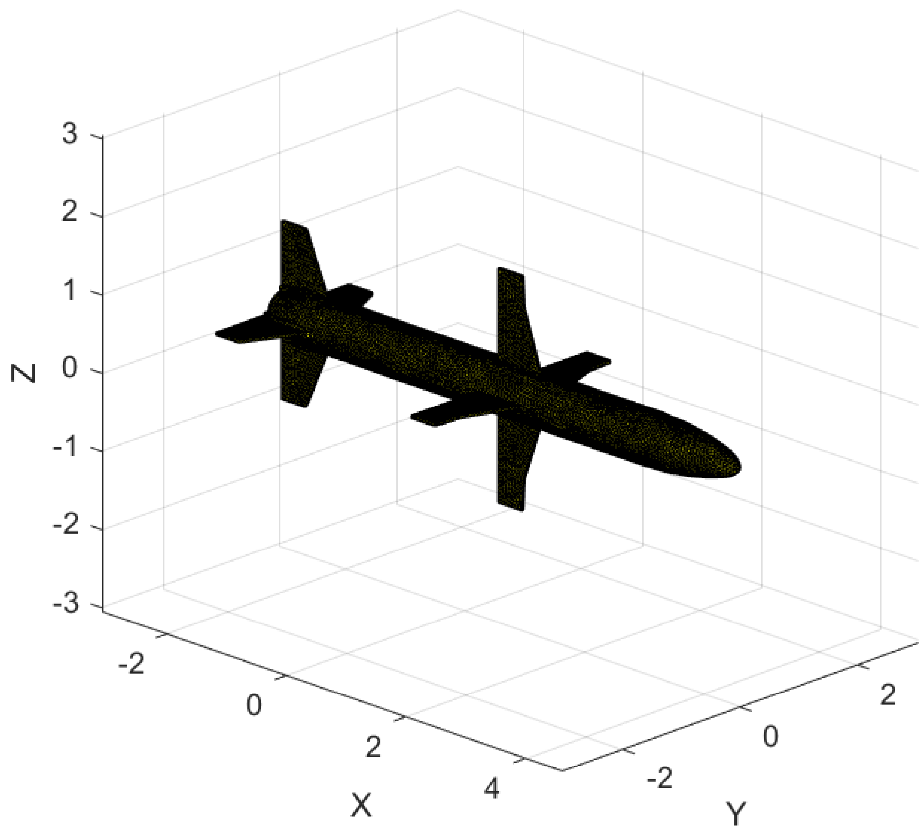

Figure 6.17 : Missile in a denser mesh.

Table 6.3 : Missile model properties 2.

Parameter	Value
Model name	Missile
Number of triangles	22934
Number of points	11469
X Size	7.72 m
Y Size	3 m
Z Size	7.72 m
Total area	24.9431 m^2
Max triangle area	0.00166 m^2
Min triangle area	$3.38158e-05$ m^2

The evaluation was conducted with a fixed elevation angle $\phi = 0°$ while varying the azimuth angle θ from $0°$ to $180°$. The angular configuration is depicted in Figure 6.18.

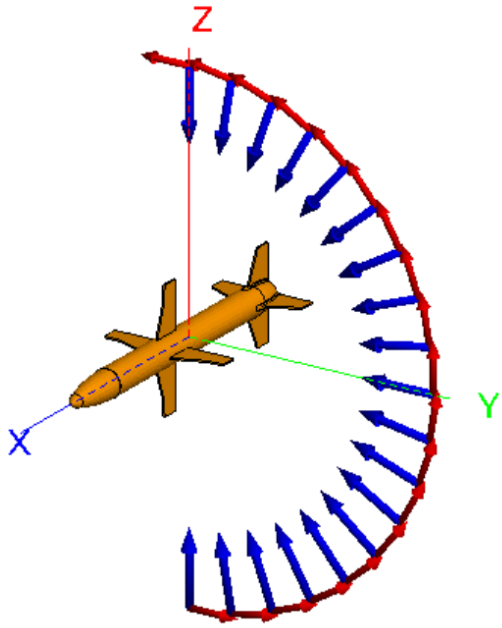

Figure 6.18 : ϕ=90°, θ=0° – 180°.

To validate the RCS results obtained from the proposed algorithm, a comparison was performed with the results from FEKO software under identical conditions for both VV and HH polarizations. Figures 6.19 and 6.20 present the RCS results for VV and HH polarizations, respectively.

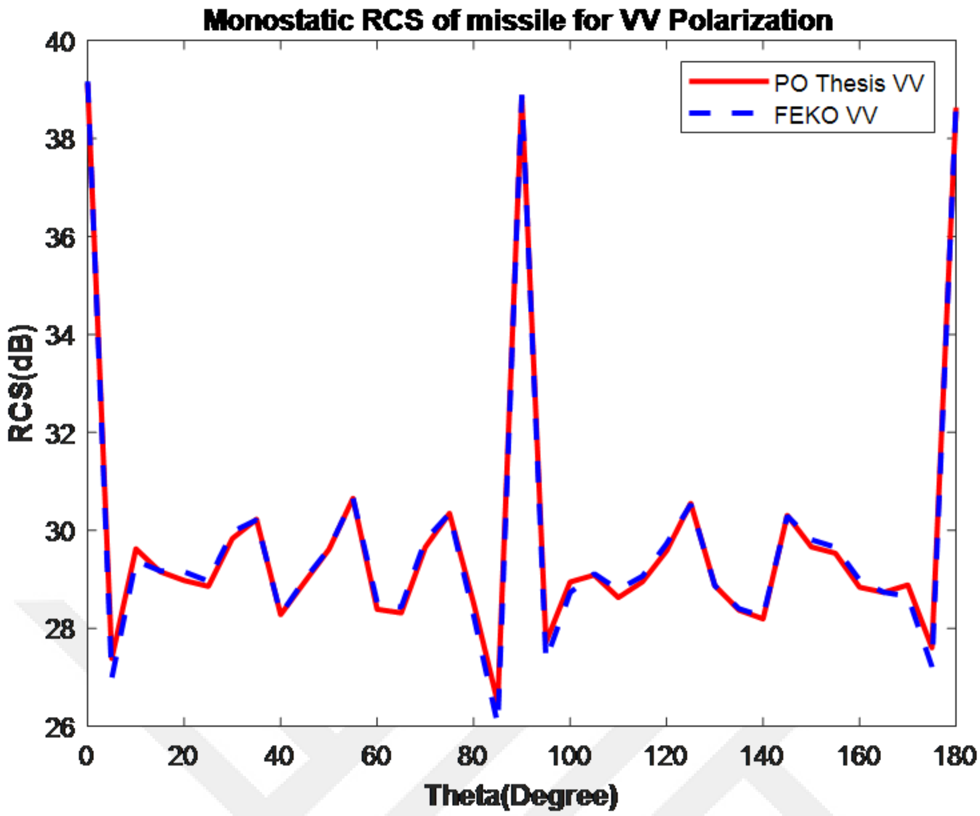

Figure 6.19 : Monostatic RCS of missile for VV polarization at different θ angles.

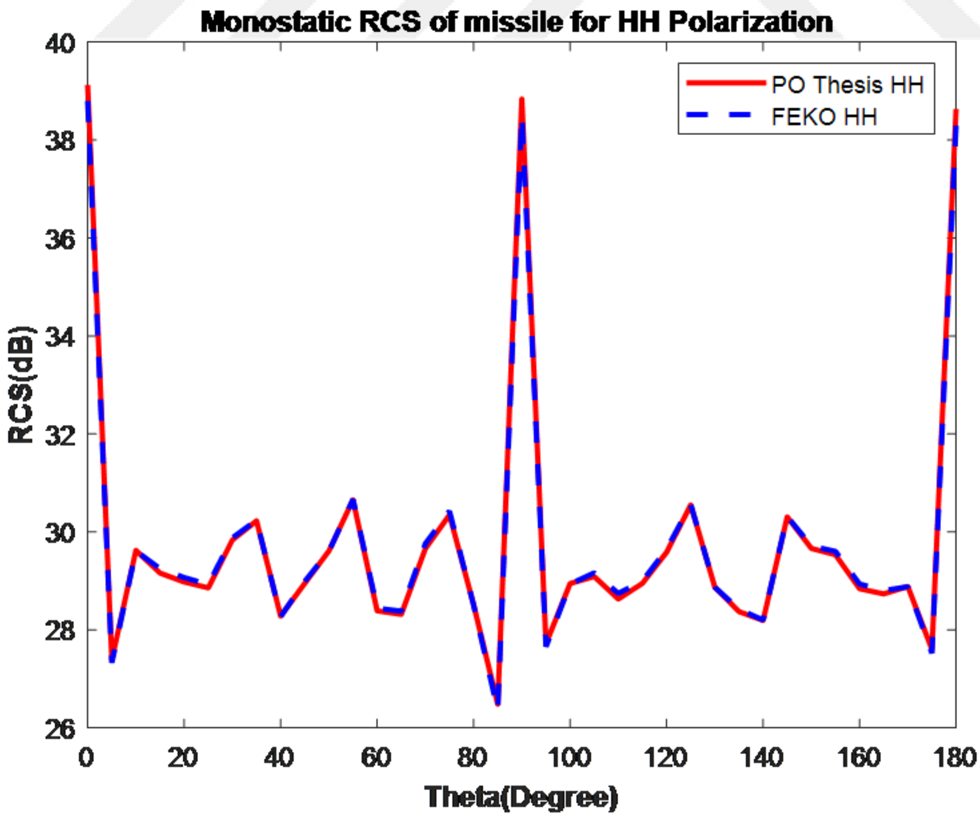

Figure 6.20 : Monostatic RCS of missile for HH polarization at different θ angles.

After validation, a detailed analysis was conducted from a specific viewing angle $\phi = 90°$, $\theta = 90°$. Figure 6.21 illustrates the induced surface currents, providing insight into the scattering characteristics of the target. The RCS values of individual mesh elements from this perspective were further analyzed to generate a radar range profile.

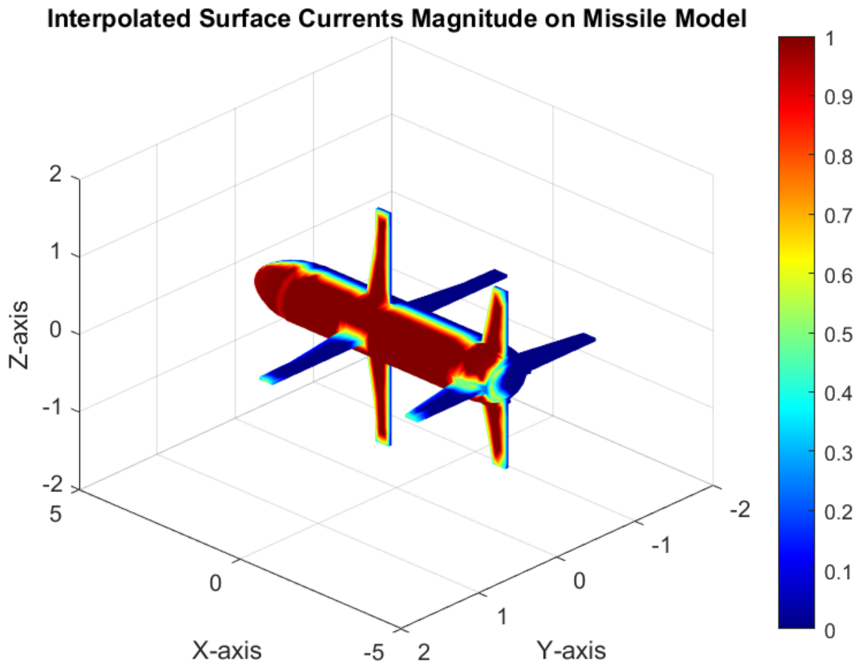

Figure 6.21 : Surface currents.

To simulate radar operation, five radar pulses were generated, amplified, and transmitted towards the target. These pulses interacted with the target based on its RCS, and the reflected signals were received, amplified, and processed, accounting for noise and signal attenuation. The transmitted, reflected, and received signals are shown in Figure 6.22, while Figure 6.23 focuses on the first transmitted pulse, highlighting the time delay and gain loss in the reflected signal.

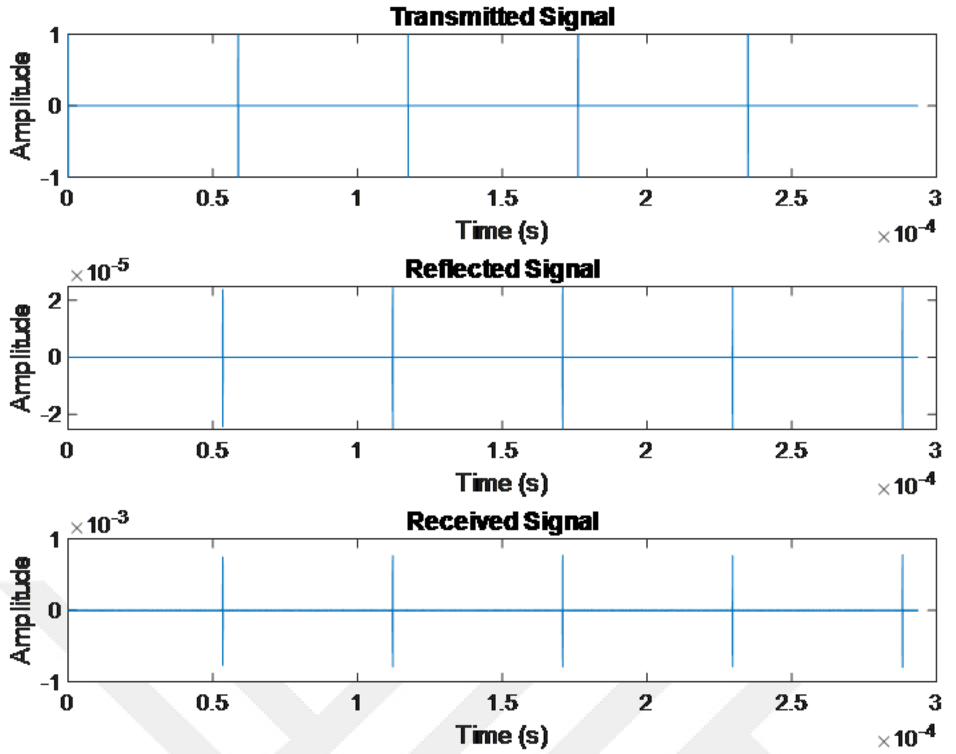

Figure 6.22 : Transmitted, reflected and received signals.

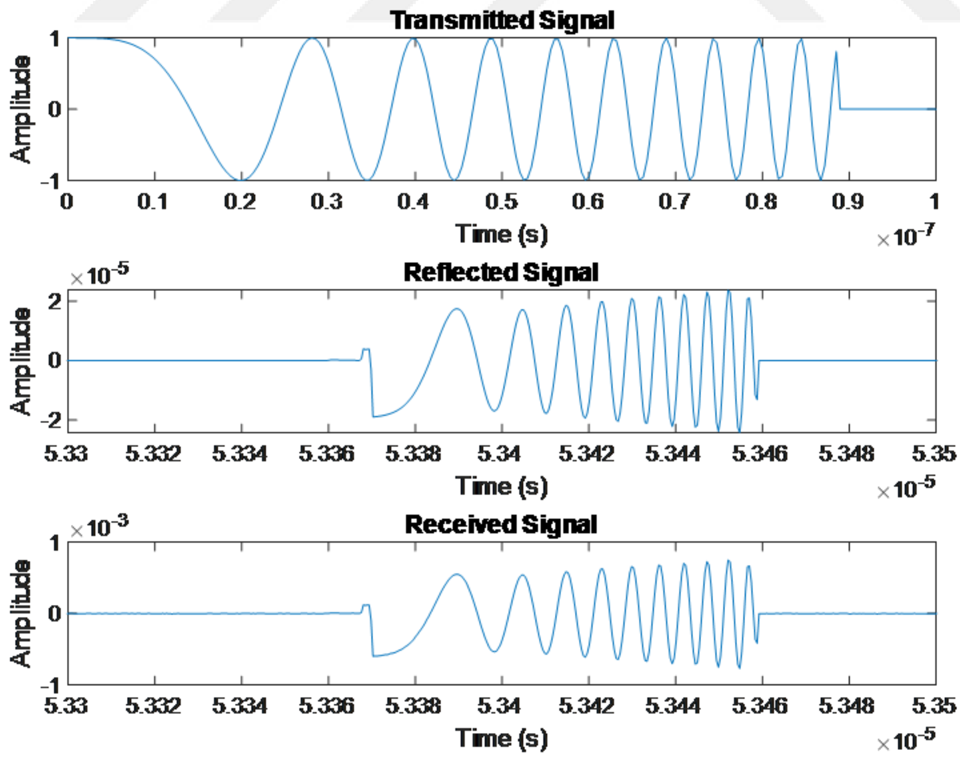

Figure 6.23 : First pulses that are transmitted, reflected and received.

The received signals were processed using a detection threshold to differentiate between noise and target reflections. Assuming noncoherent detection and white Gaussian noise, a threshold of -108.7 dBW was determined over 5 pulses. The first two received pulses, along with this threshold, are shown in Figure 6.24.

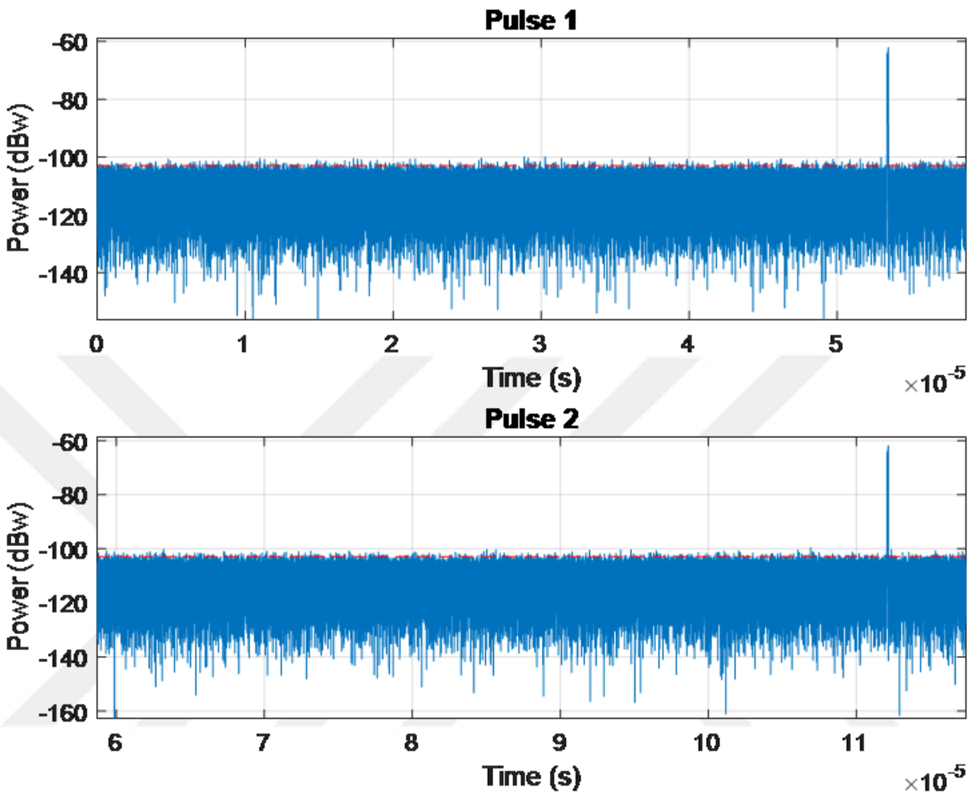

Figure 6.24 : The first two received pulses with applied threshold.

To enhance the signal-to-noise ratio (SNR), a matched filter was applied. This filter improved the detection threshold to -80 dBW The matched filter results are presented in Figure 6.25.

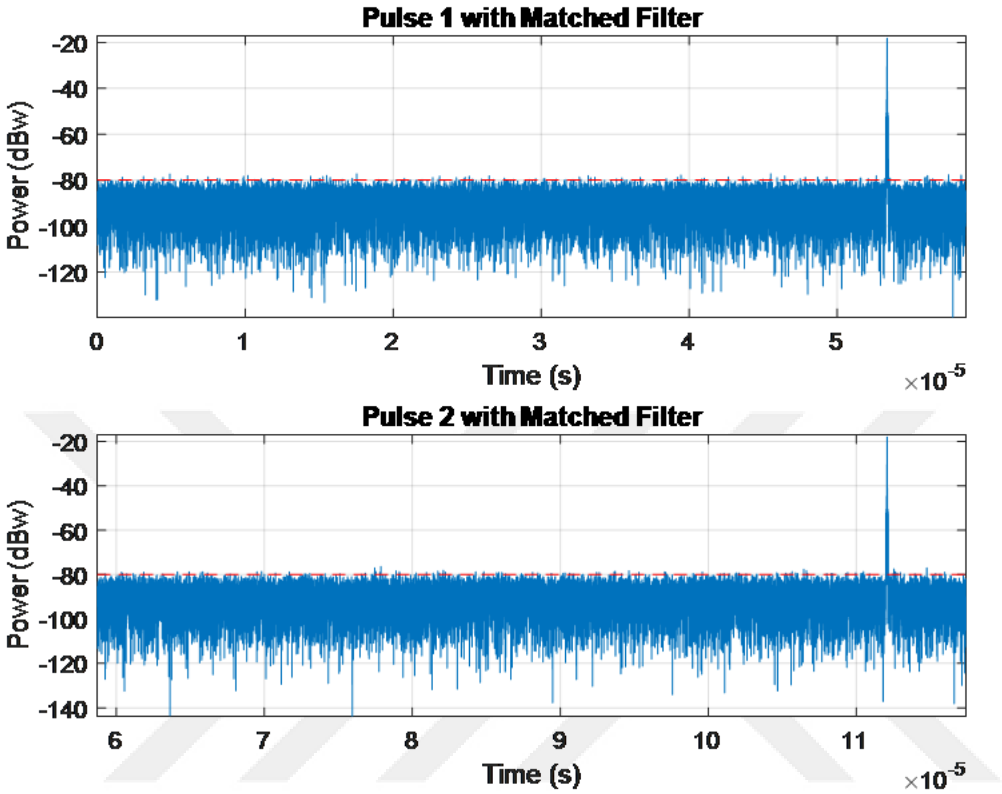

Figure 6.25 : Application of matched filter.

However, closer range bins exhibited stronger signal returns, potentially masking distant targets. To address this, range normalization was applied to equalize signal strengths across all ranges, as shown in Figure 6.26.

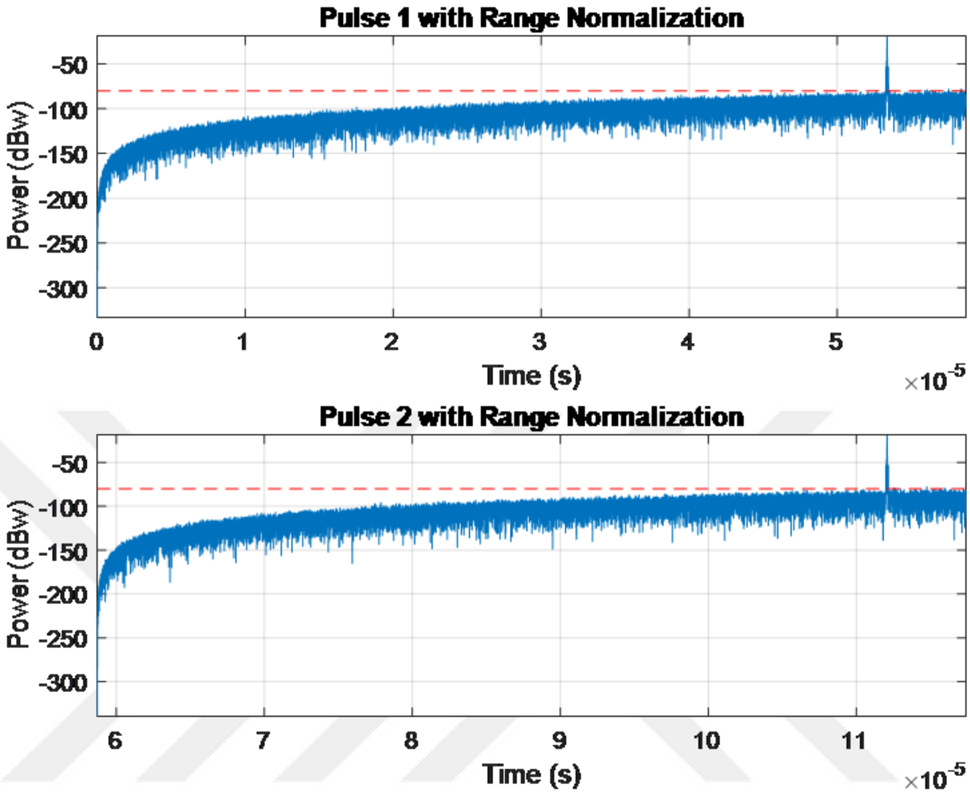

Figure 6.26 : Range normalization.

After normalization, coherent integration was performed on the range-normalized pulses to further improve SNR. The integrated results, shown in Figure 6.27, were then used to generate the High-Resolution Range Profile (HRRP). .

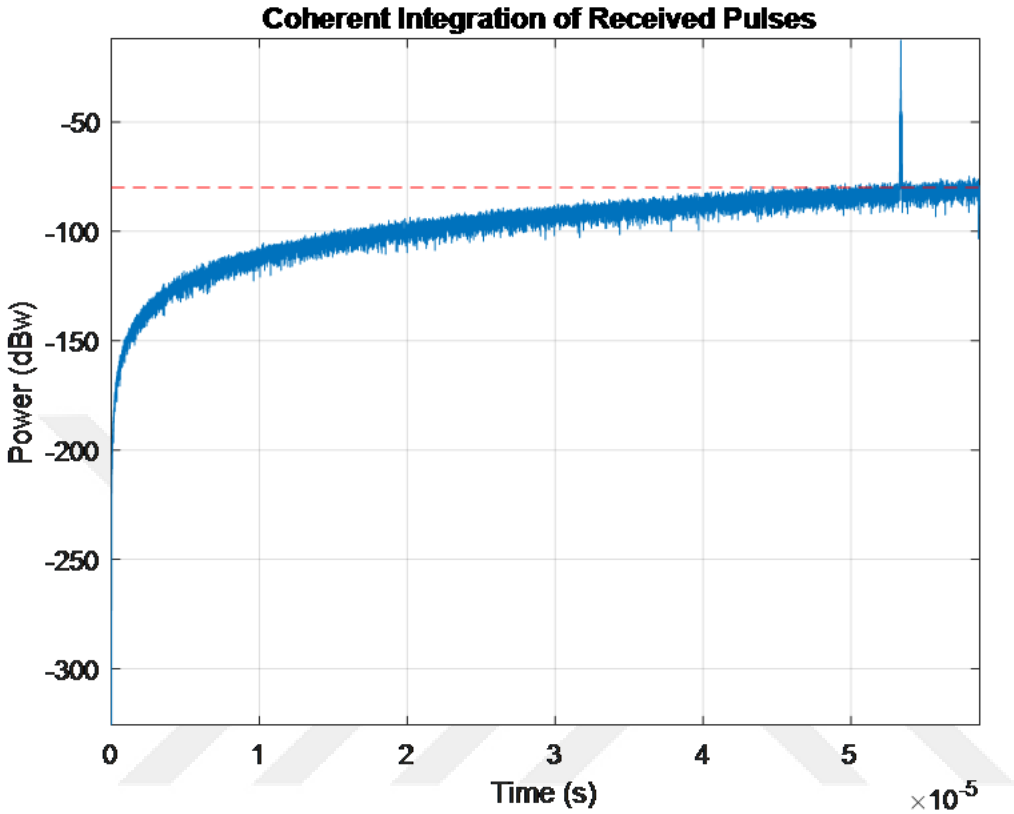

Figure 6.27 : Coherent integration of received pulses.

The real part of the integrated pulses are shown in the figure below. The estimated range of 7997.4 closely matches the actual range of 7997.3.

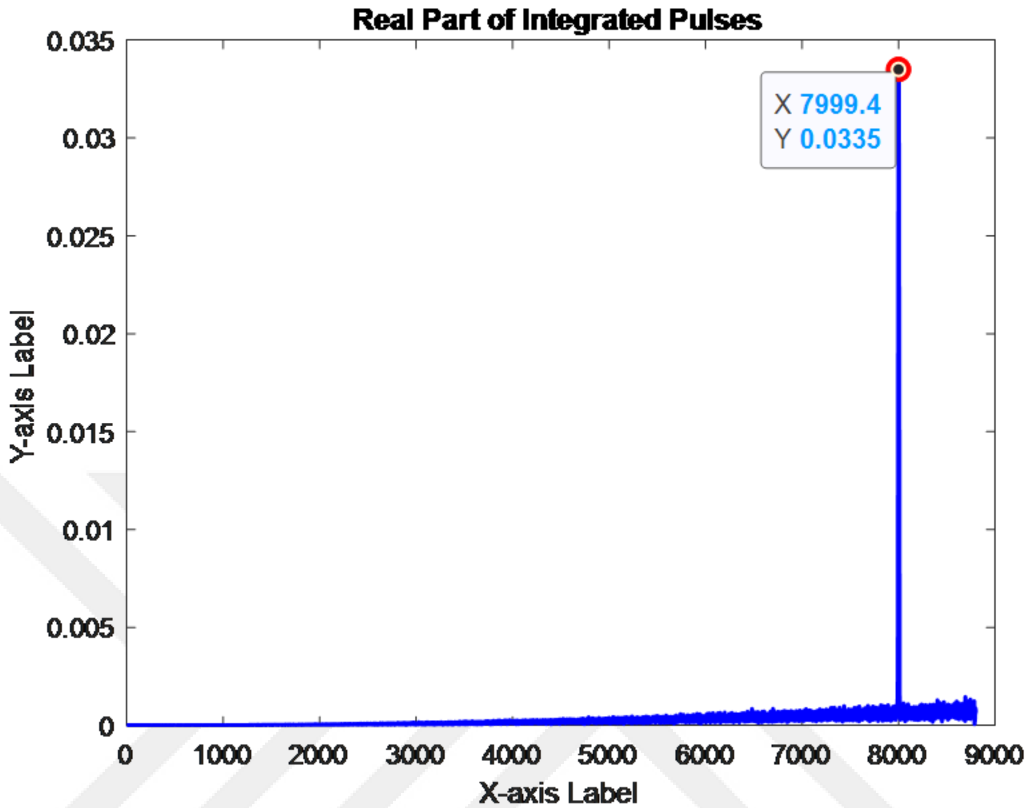

Figure 6.28 : High resolution range profile of the target.

The HRRP is shown in Figure 6.29, with the estimated target size determined as 7.1 meters, close to the actual size which is 7.3 meters.

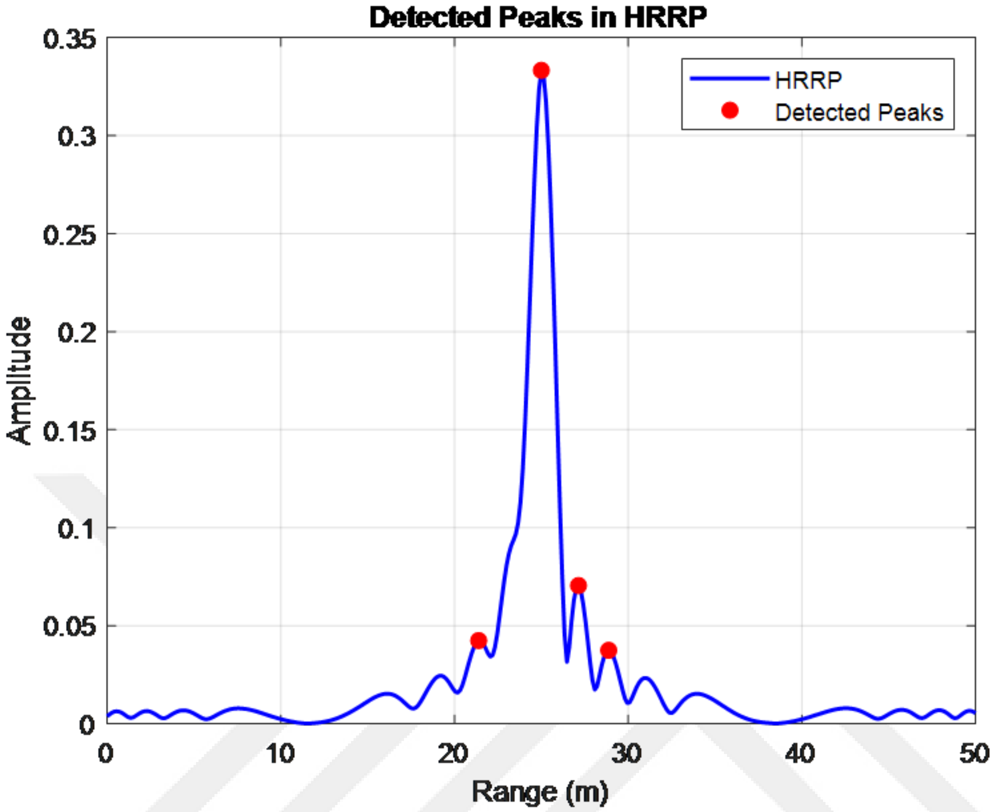

Figure 6.29 : High resolution range profile of the target.

6.2 F-22 Aircraft

The analyses are performed for two different operation frequencies as 2GHz and 4GHz. The F-22 Aircraft, depicted in Figure 6.30, is characterized by its physical dimensions, including overall size, surface area, and the range of triangle areas used in the mesh. The detailed properties of the structure are listed in Table 6.5.

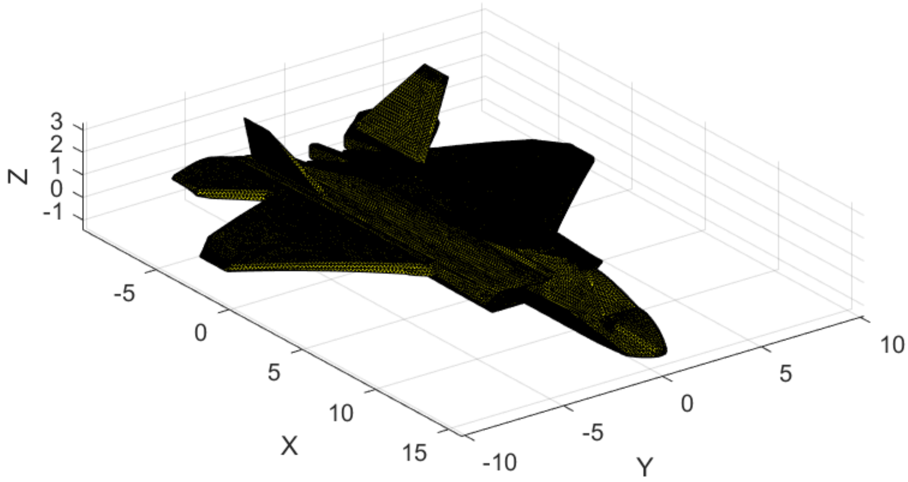

Figure 6.30 : F-22 Mesh.

Table 6.4 : F-22 model properties.

Parameter	Value
Model name	F-22 Aircraft
Number of triangles	51288
Number of points	1640
X Size	25.8636 m
Y Size	18.7219 m
Z Size	25.8636 m
Total area	549.6833 m^2
Max triangle area	0.02536 m^2
Min triangle area	$5.70618e - 05 \times 10^{-5}$ m^2

6.2.1 Analysis for 2 GHz

A comprehensive analysis was conducted to evaluate the electromagnetic response of the F-22 aircraft. In this analysis, the azimuth angle *theta* was fixed at 90°, while the elevation angle *phi* varied from 0° to 180° in increments of 10°. The corresponding angles that were scanned are shown in Figure 6.31.

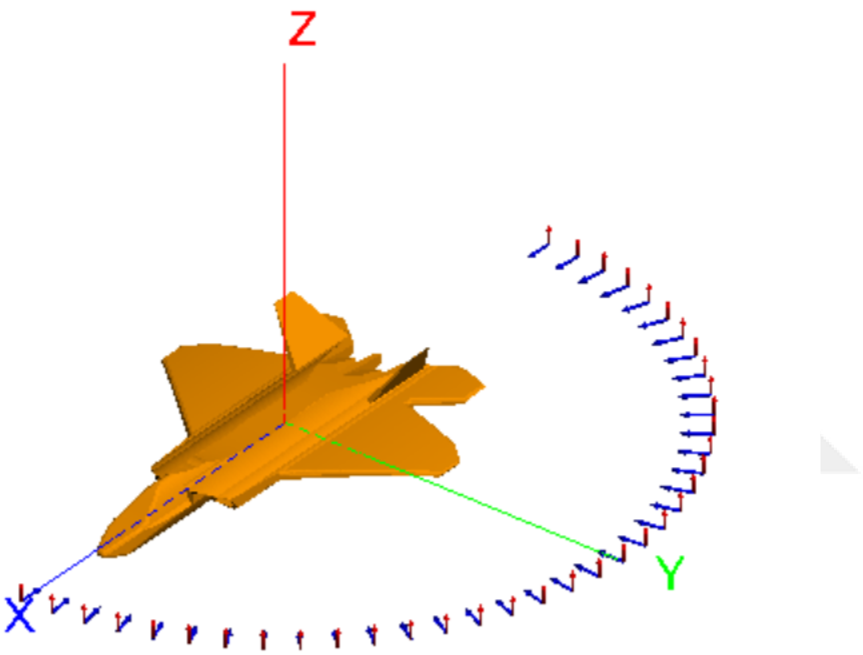

Figure 6.31 : ϕ=0°-180°, θ=90°.

The results of this analysis were compared with FEKO simulations. The comparisons are shown in Figure 6.32 for HH polarization and Figure 6.33 for VV polarization.

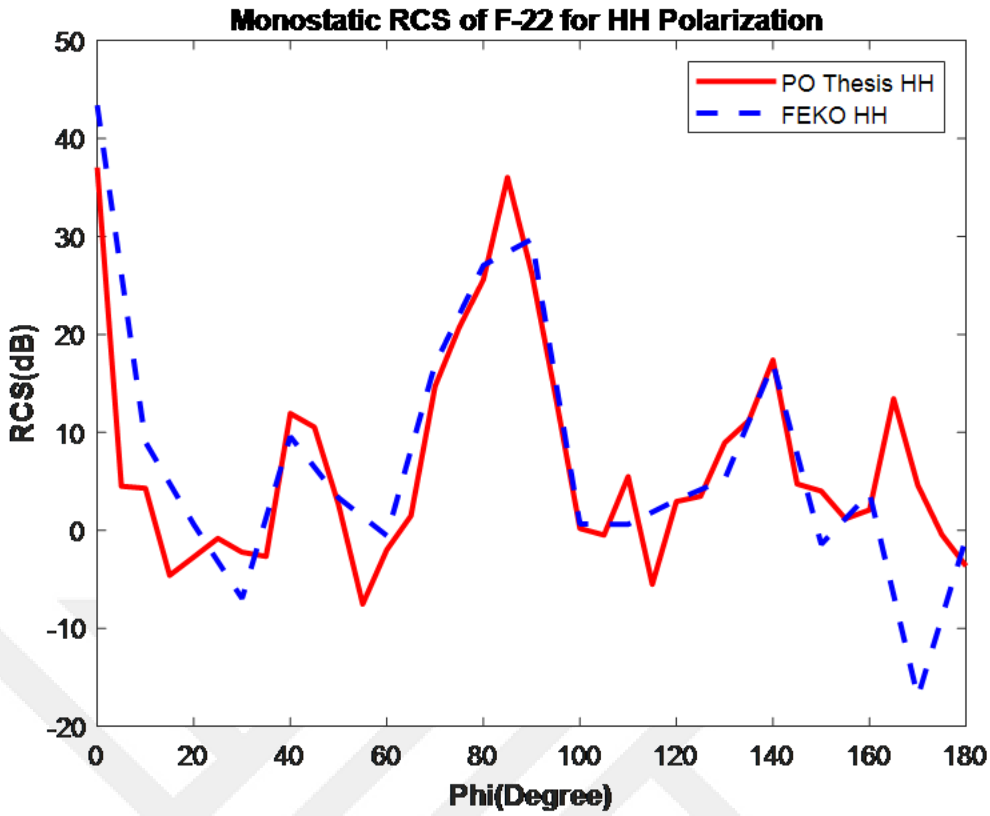

Figure 6.32 : Monostatic RCS of F-22 for HH polarization at different ϕ angles.

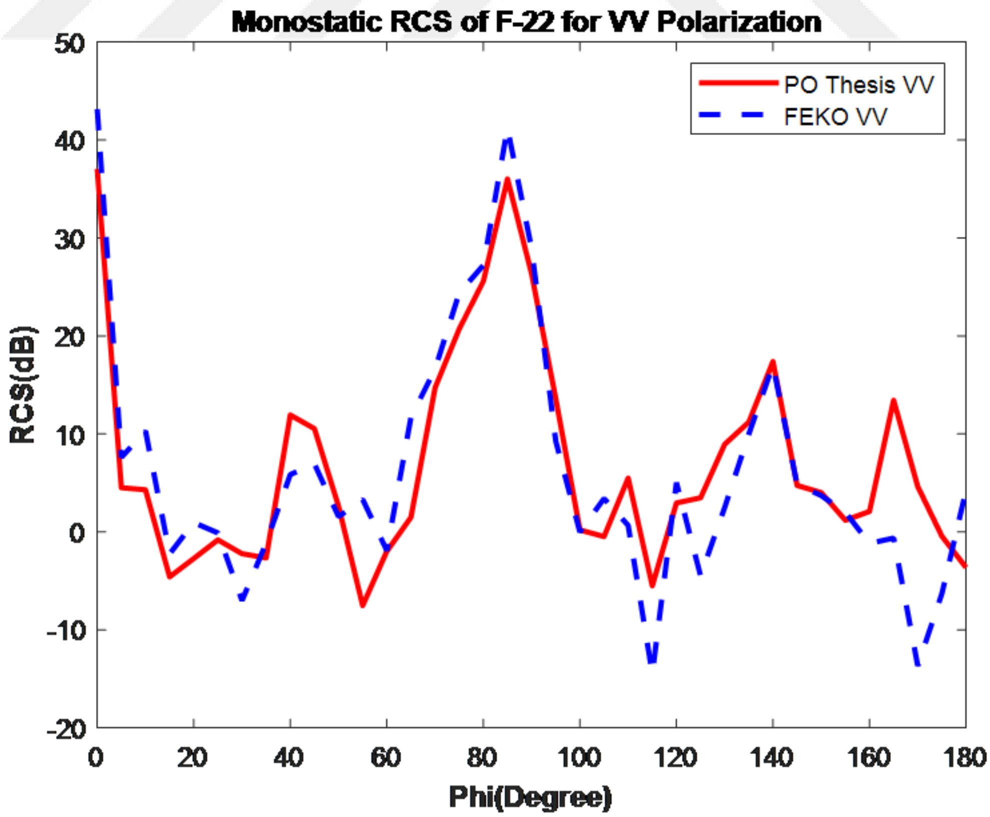

Figure 6.33 : Monostatic RCS of F-22 for VV polarization at different ϕ angles.

After validating the RCS analysis, the target was analyzed from a fixed point of view. For the range profile analysis, $\theta = 90^\circ$ and $\phi = 0^\circ$ were chosen. The surface currents from this viewpoint are shown in Figure 6.34.

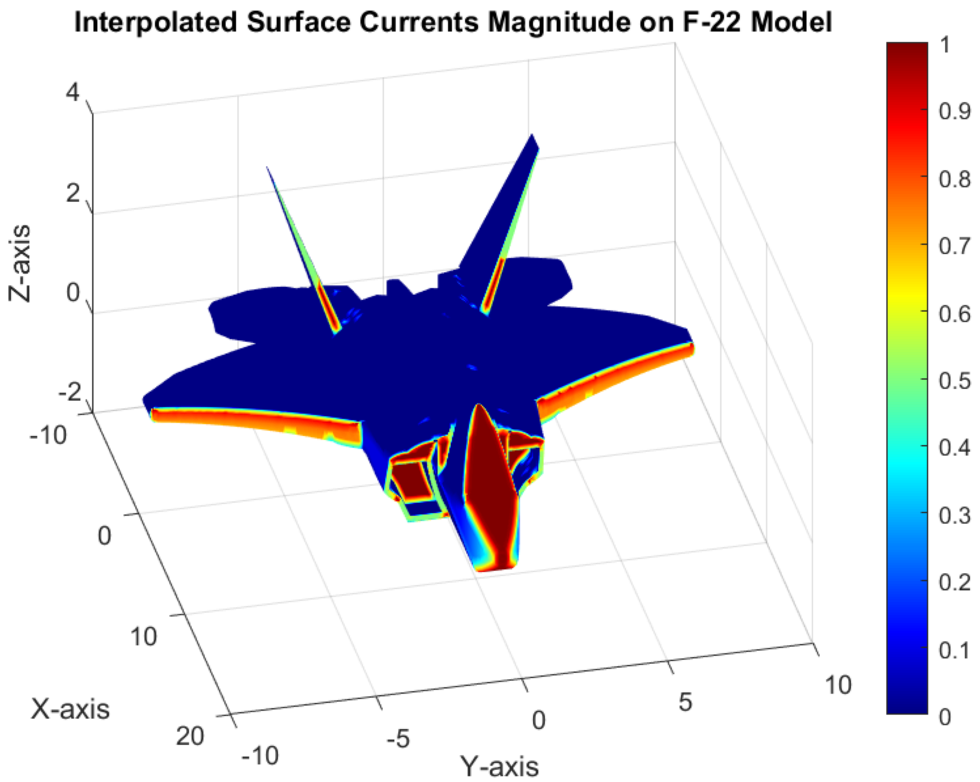

Figure 6.34 : Surface currents of F-22.

Ten radar pulses were generated and transmitted through the target. Using the RCS values of the illuminated target mesh elements, the reflected and received signals were obtained and are shown in Figure 6.35. For a detailed examination, the first pulse is separately shown in Figure 6.36, depicting the delay in the reflected signal and attenuation in the received signal.

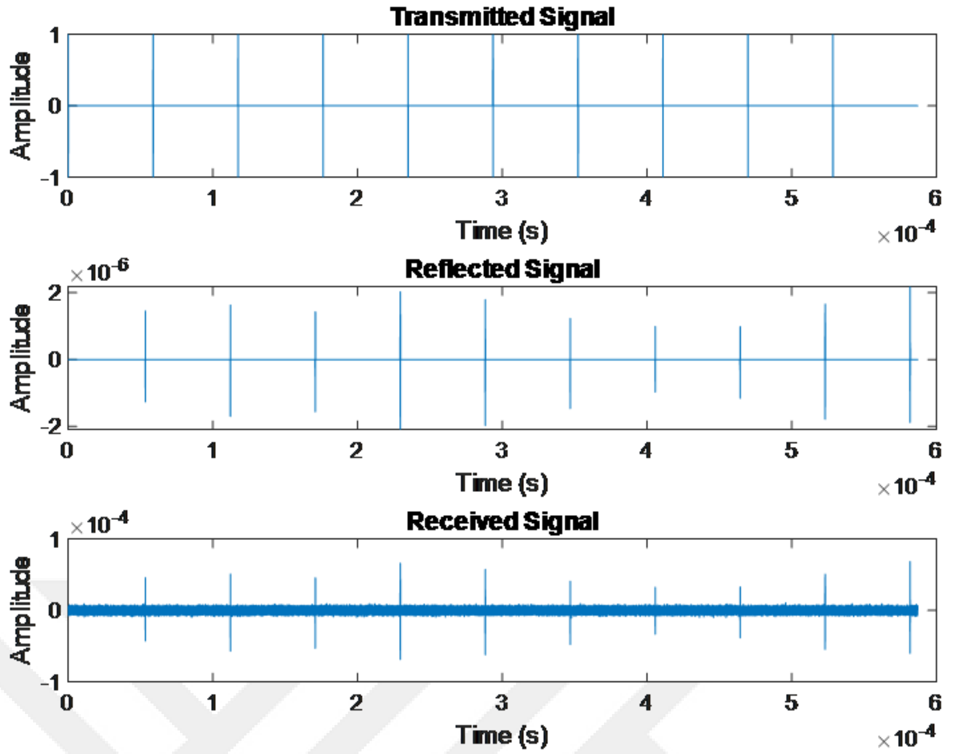

Figure 6.35 : Transmitted, reflected and received Pulses.

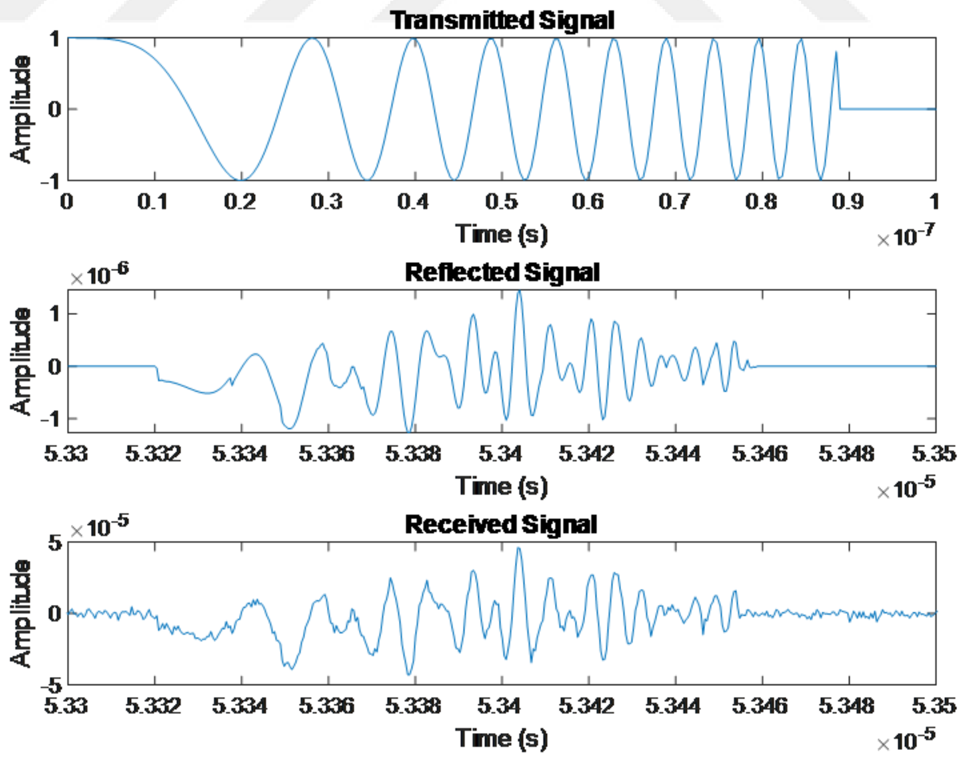

Figure 6.36 : First pulses that are transmitted, reflected and received.

The first two pulses at the detector are shown in Figure 6.37. As can be seen, only the portion of the signal exceeding the threshold is captured and transmitted to the receiver.

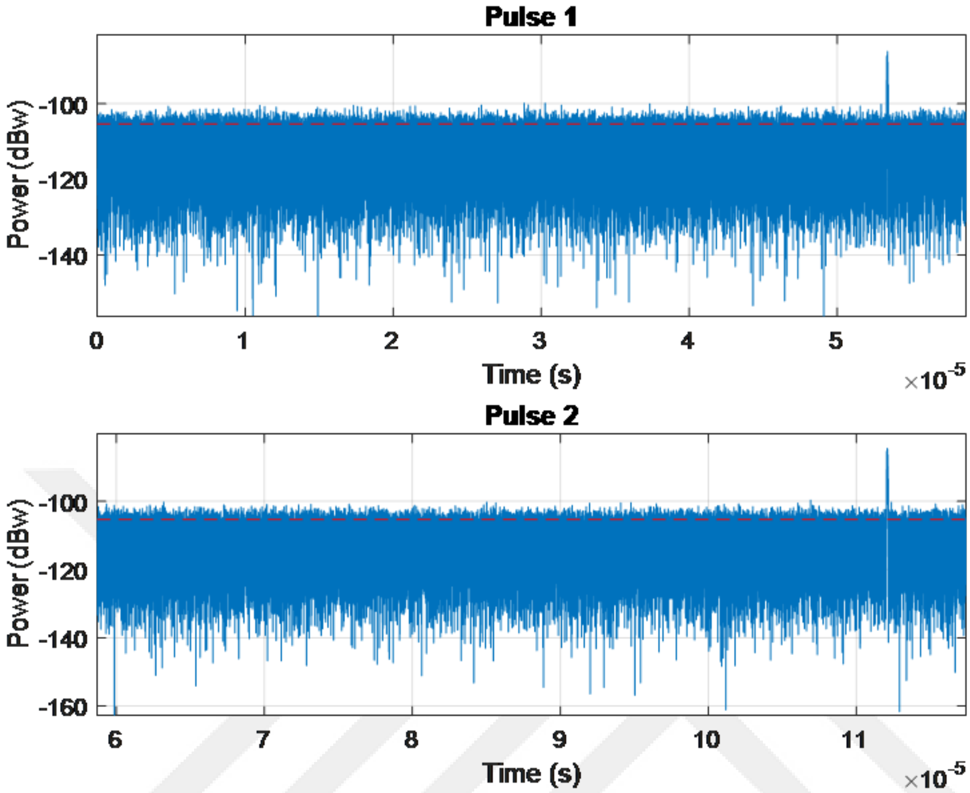

Figure 6.37 : The first two received pulses with applied threshold.

After the pulses are received, a matched filter is applied, and the threshold is calculated as -60 dBW. The matched filter responses of these pulses are shown in Figure 6.38. This process successfully eliminates noise components.

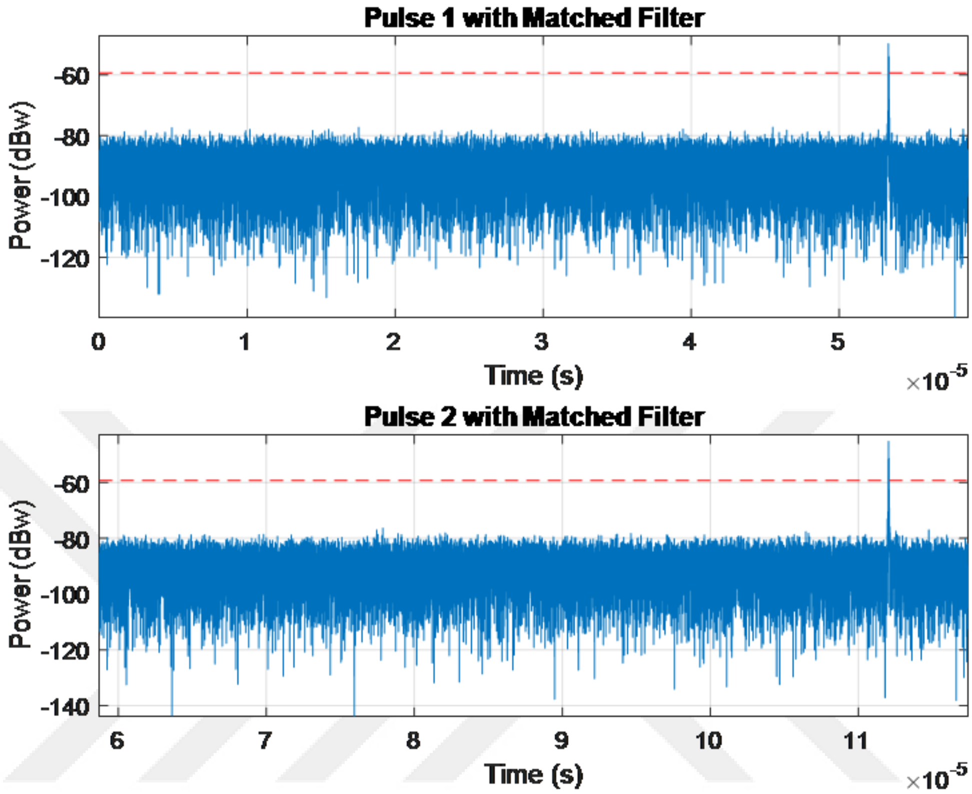

Figure 6.38 : Application of matched filter.

To eliminate the effects of varying ranges, range normalization was applied. The final signal graphs for the first two pulses are shown in Figure 6.39.

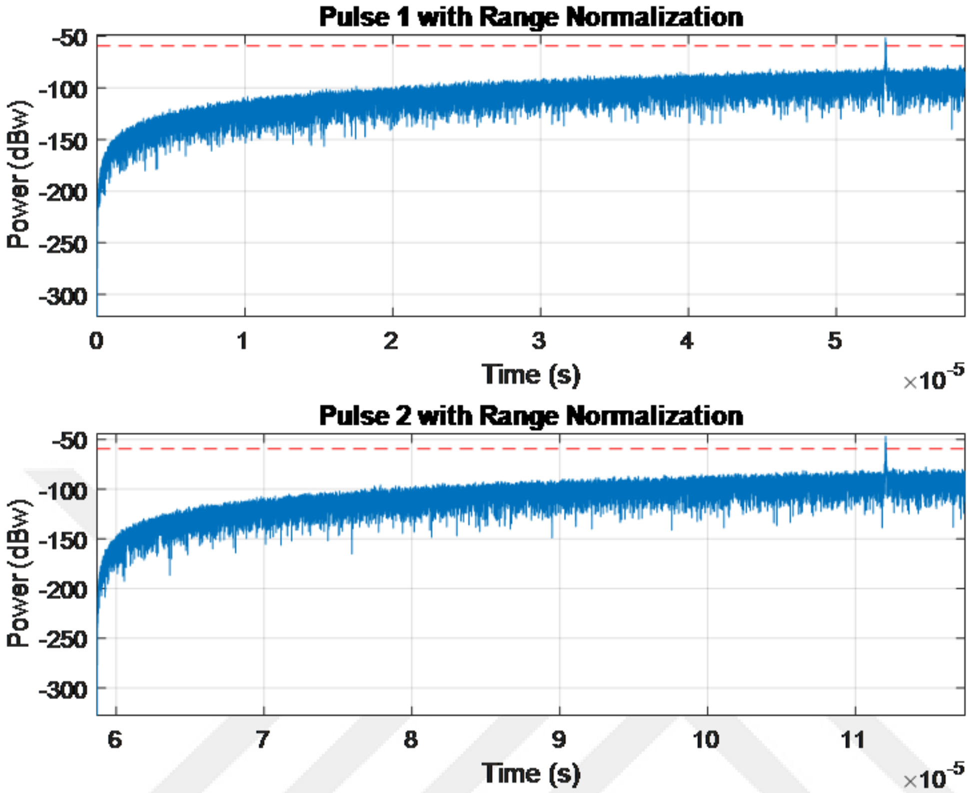

Figure 6.39 : Range normalization.

The coherent integration of the pulses was performed to gather all responses and create range profile data. The results of the integration are shown in Figure 6.40

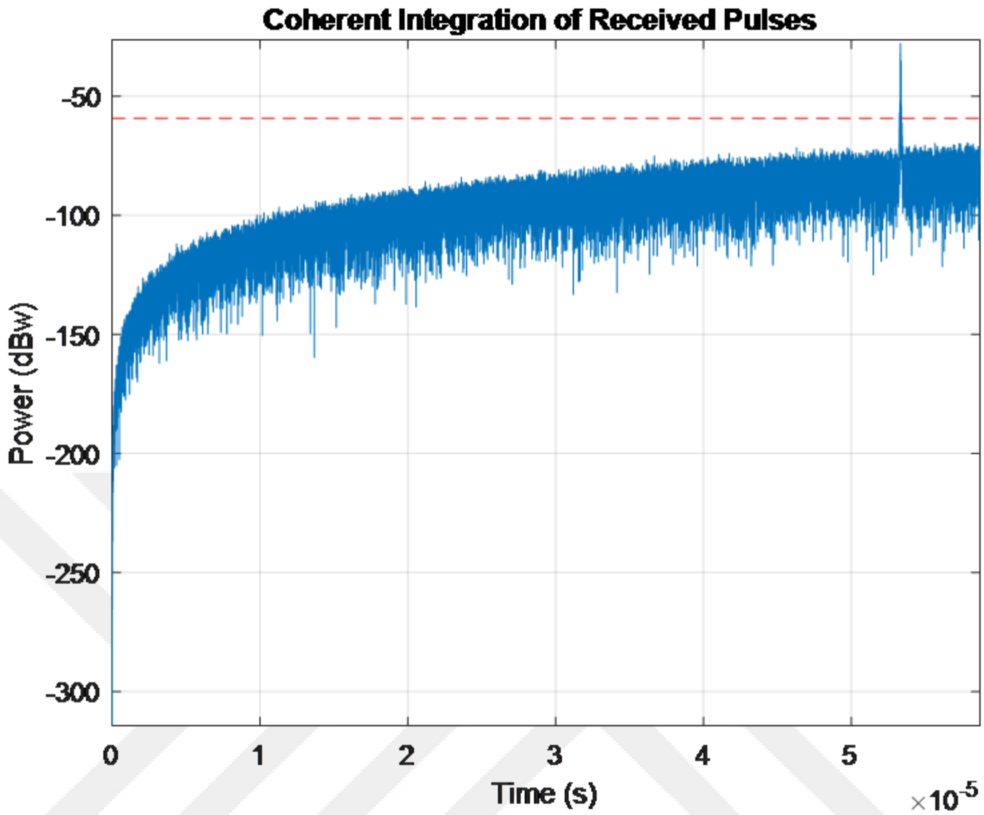

Figure 6.40 : Coherent integration of the pulses.

The detected peaks are shown in Figure 6.41. The range of the target was estimated based on the location of the largest peak in the range bins. The estimated target range is 7998.9 meters, compared to the actual target range of 7998.95 meters.

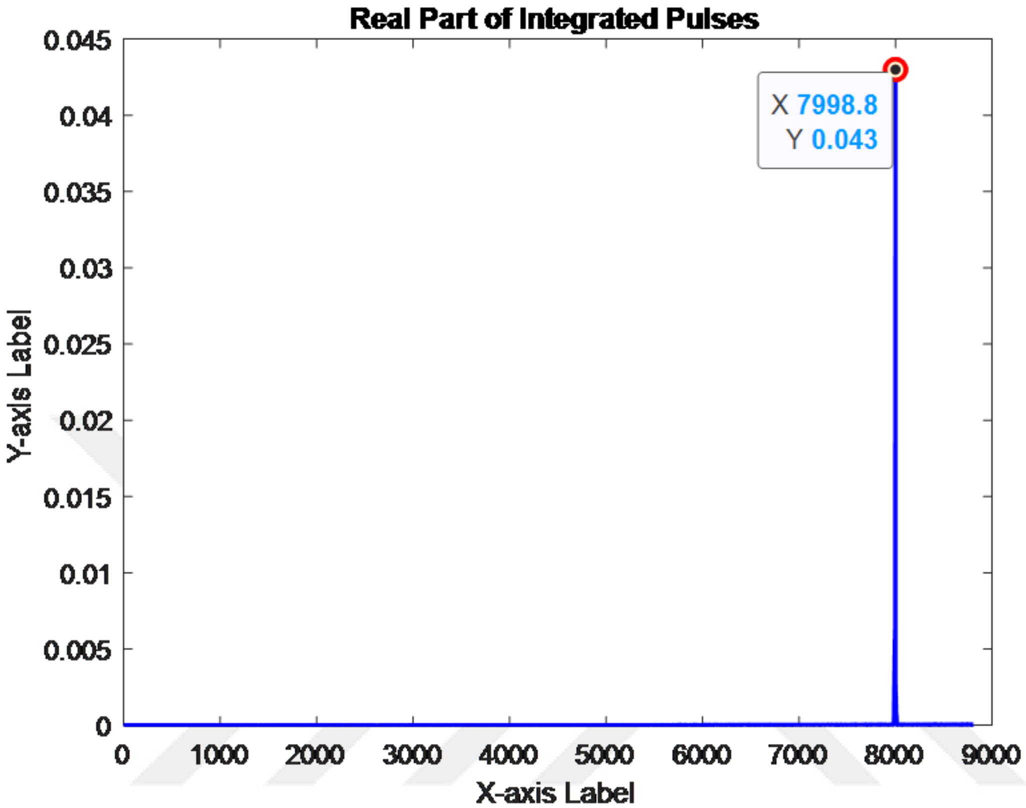

Figure 6.41 : Range estimation of F-22.

HRRP is shown in the Figure 6.42. The calculated physical size is approximately 19.25 meters, which aligns well with the actual size of 20 meters, considering the range resolution of 1 meter.

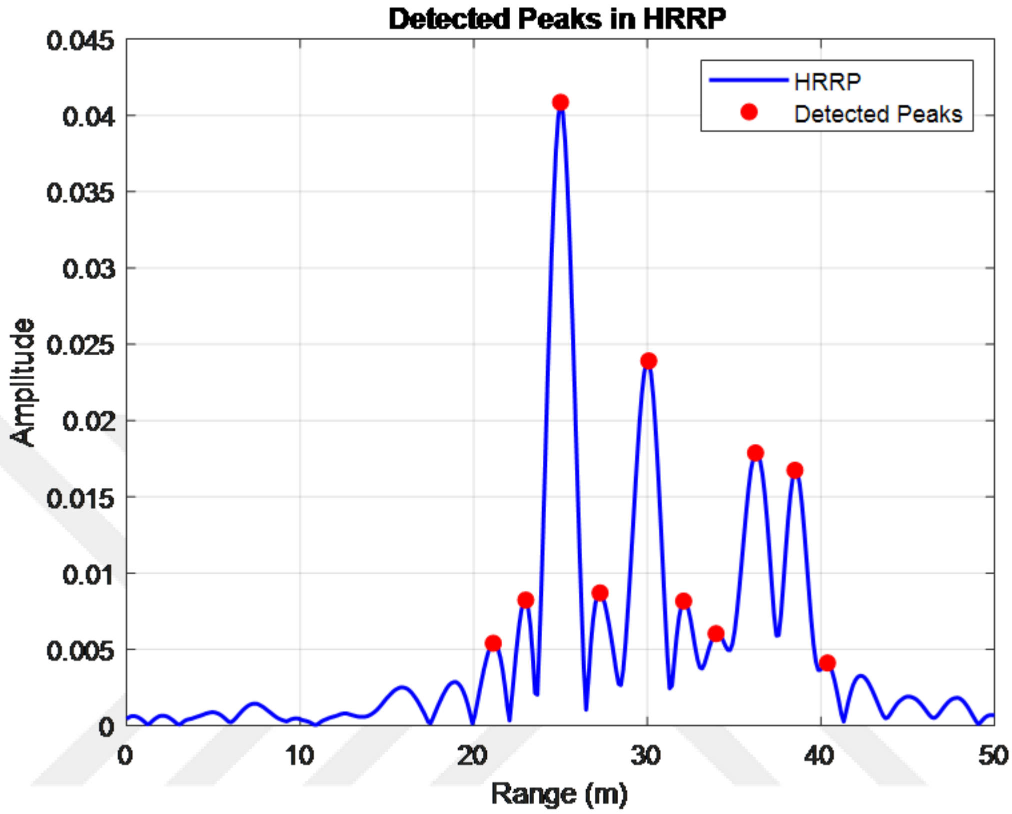

Figure 6.42 : High resolution range profile of the target.

6.2.2 Analysis for 4 GHz

For 4 GHz, two sets of analyses were performed to validate the RCS results. In the first analysis, the azimuth angle (θ) was fixed at 90°, while the elevation angle (ϕ) was varied from 0° to 180° in increments of 10°. The angular configuration for this analysis is illustrated in Figure 6.43.

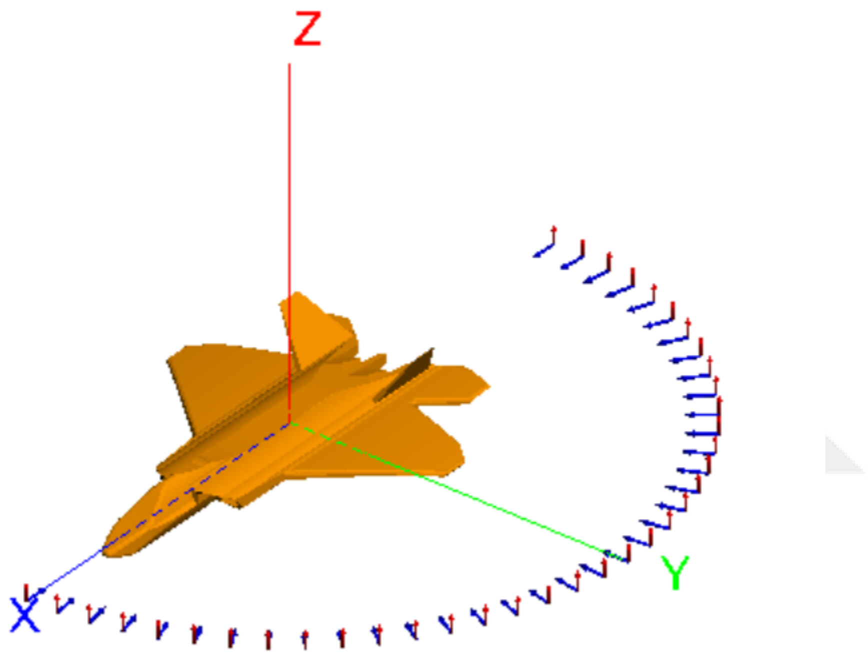

Figure 6.43 : ϕ=0°-180°, θ=90°.

The comparison of RCS results from the developed physical optics tool and the commercial software FEKO for VV and HH polarizations is shown in Figures 6.44 and 6.45, respectively. Both results demonstrate excellent agreement, validating the accuracy of the proposed approach.

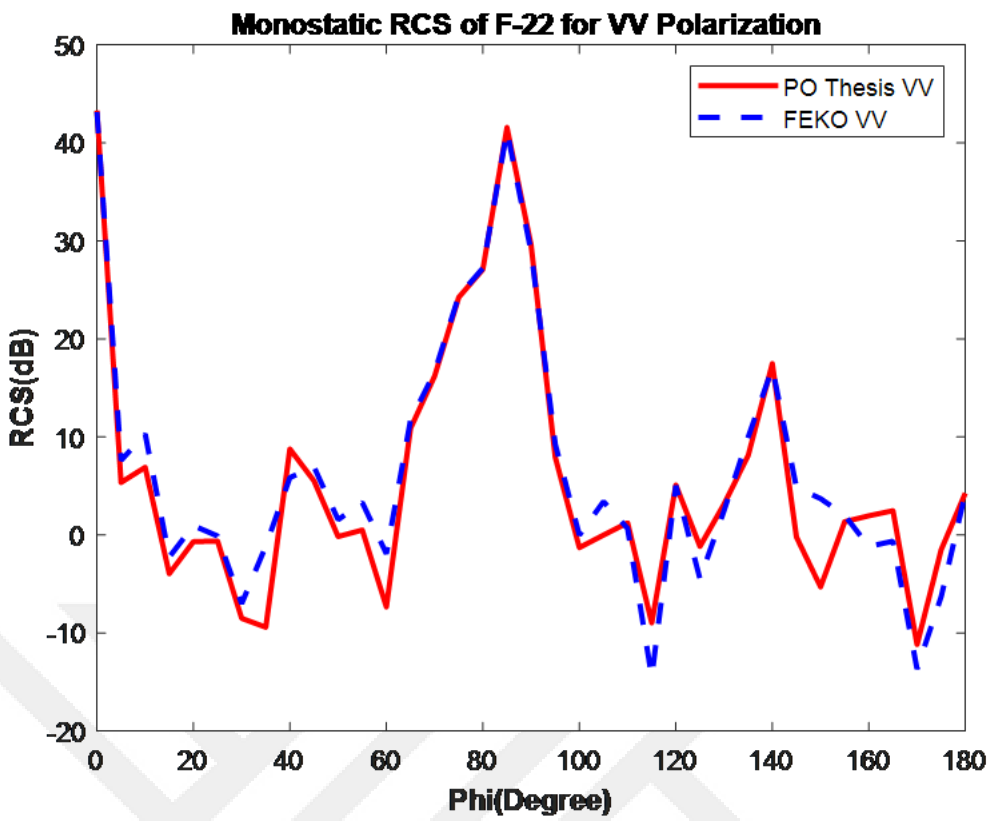

Figure 6.44 : Monostatic RCS of F-22 for VV polarization at different ϕ angles.

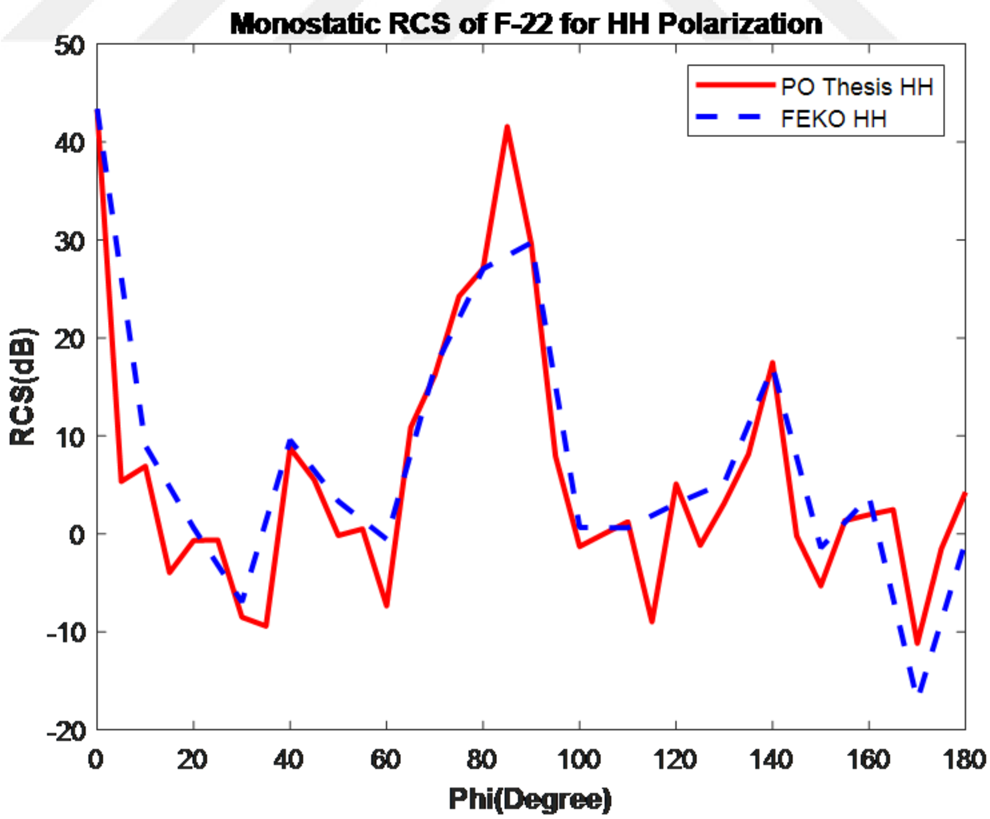

Figure 6.45 : Monostatic RCS of F-22 for VV polarization at different ϕ angles

The second analysis kept the elevation angle (ϕ) fixed at 90° while varying the azimuth angle (θ) from 0° to 180°. This angular configuration is presented in Figure 6.46.

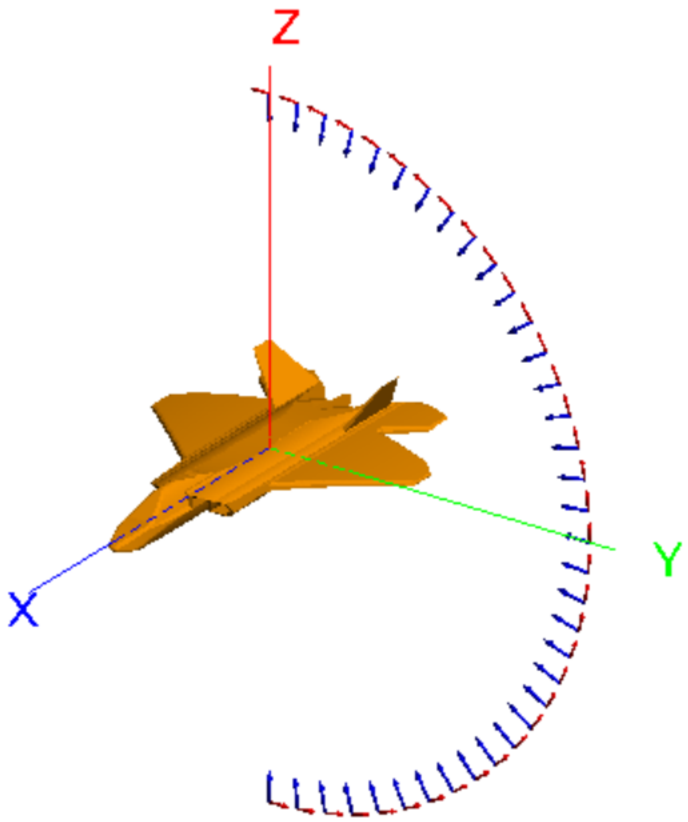

Figure 6.46 : ϕ=90°, θ=0° − 180°.

The results for VV and HH polarizations, shown in Figures 6.47 and 6.48, once again confirm the reliability of the proposed method.

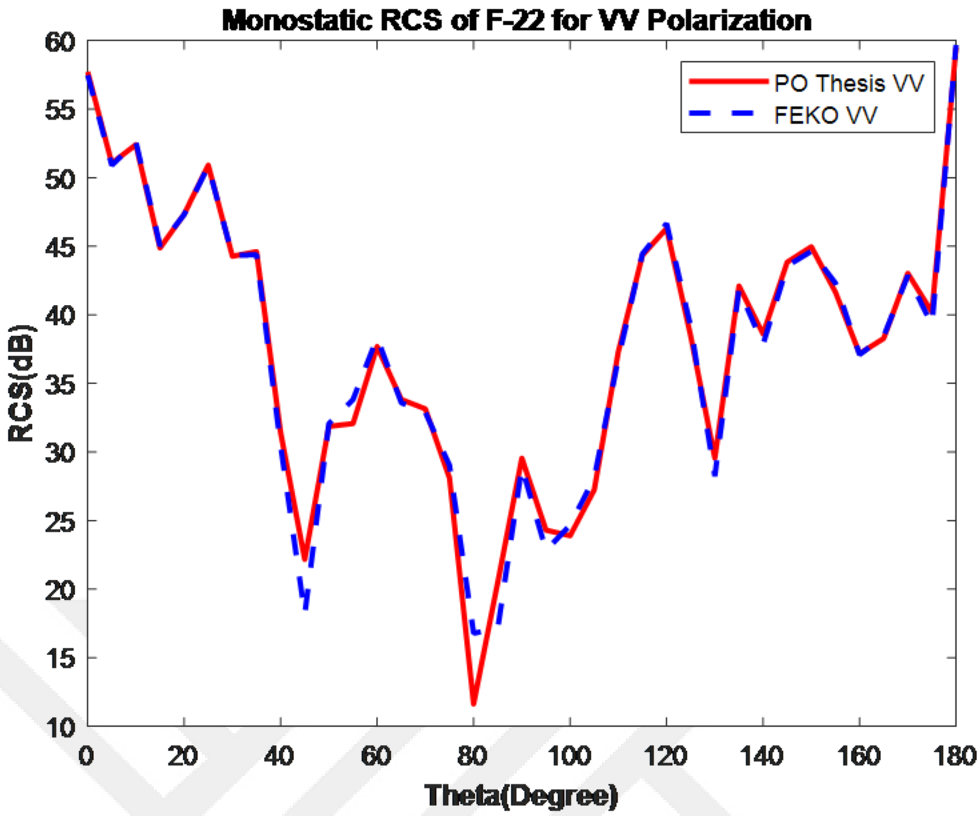

Figure 6.47 : Monostatic RCS of F-22 for VV polarization at different θ angles.

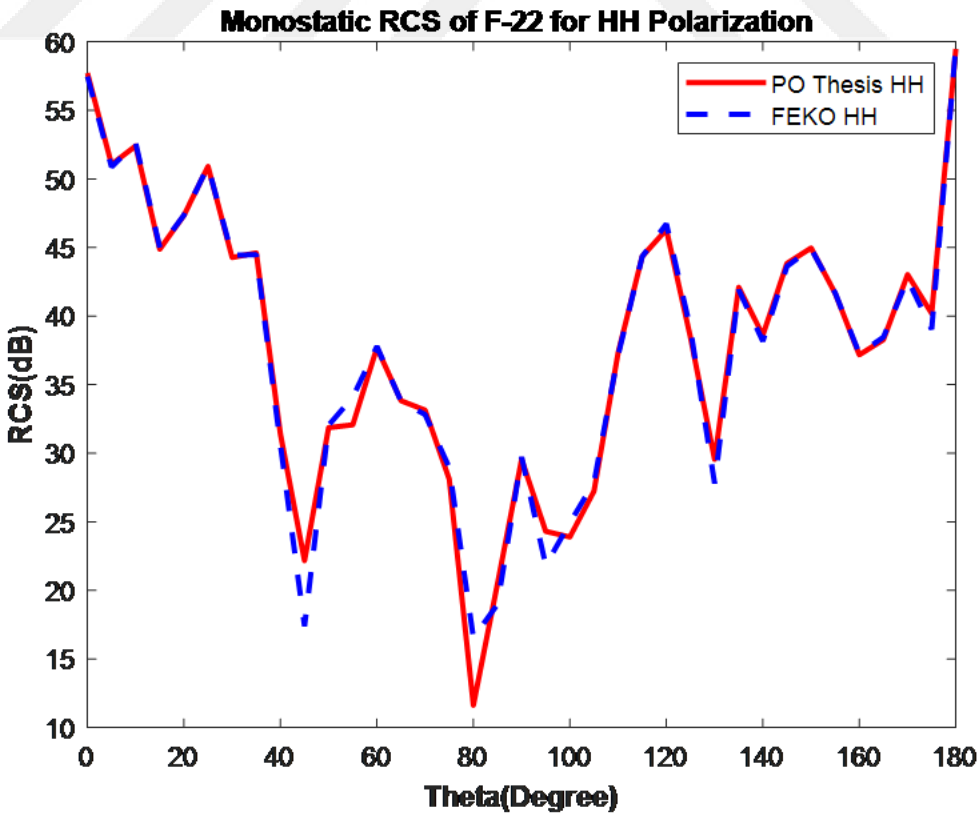

Figure 6.48 : Monostatic RCS of F-22 for VV polarization at different θ angles.

Following the RCS validation, the target was analyzed from a specific perspective with $\phi = 0°$ and $\theta = 90°$. The induced surface currents on the target, as seen from this viewpoint, are shown in Figure 6.49. These currents are essential for understanding how the target scatters electromagnetic waves.

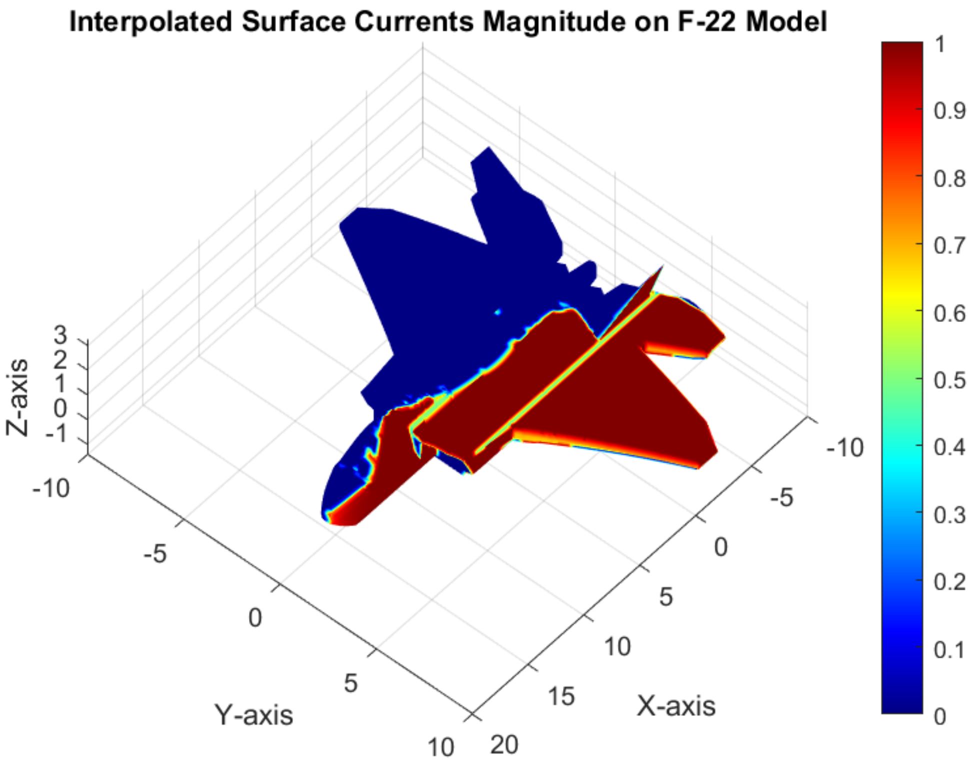

Figure 6.49 : Surface currents of F-22.

Five radar pulses were generated and transmitted toward the target. Using the RCS values of the illuminated mesh elements, the reflected and received signals were computed. These signals are illustrated in Figure 6.50. For a more detailed analysis, the first pulse is shown separately in Figure 6.51, highlighting the delay in the reflected signal and the attenuation in the received signal.

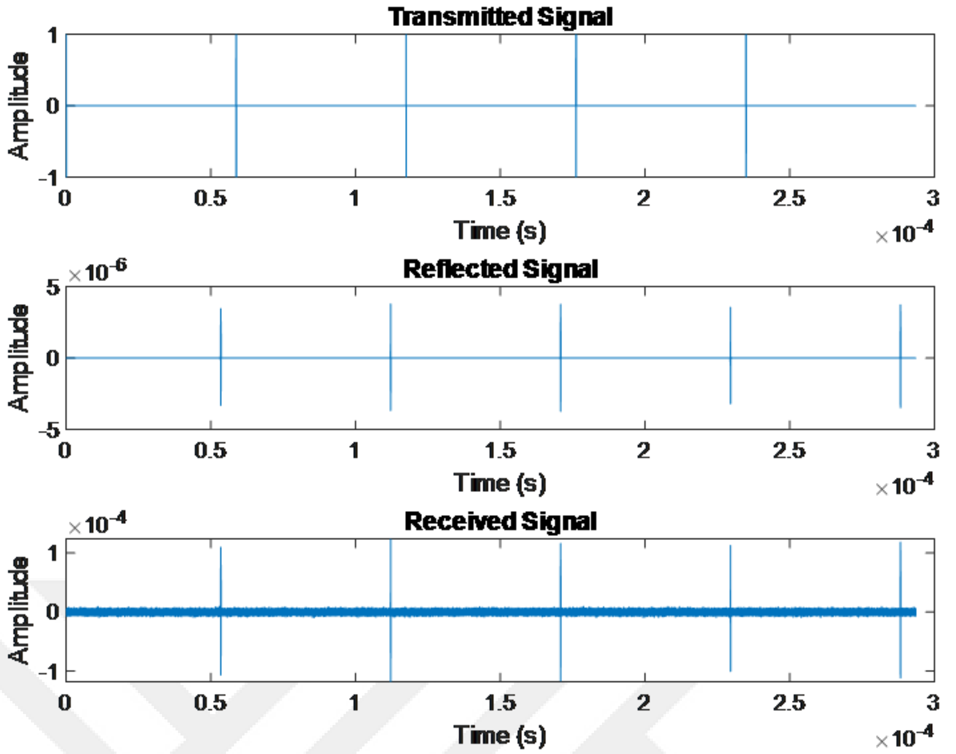

Figure 6.50 : Transmitted, reflected and received Pulses.

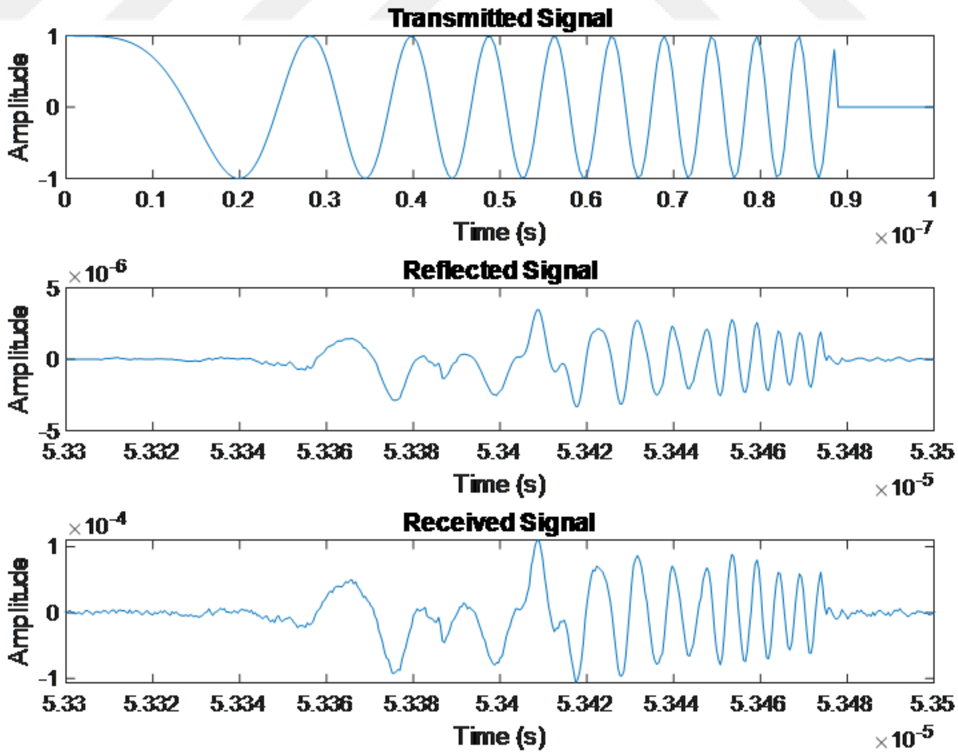

Figure 6.51 : First pulses that are transmitted, reflected and received.

The first two received pulses are presented in Figure 6.52, providing a closer look at the behavior of the received signal.

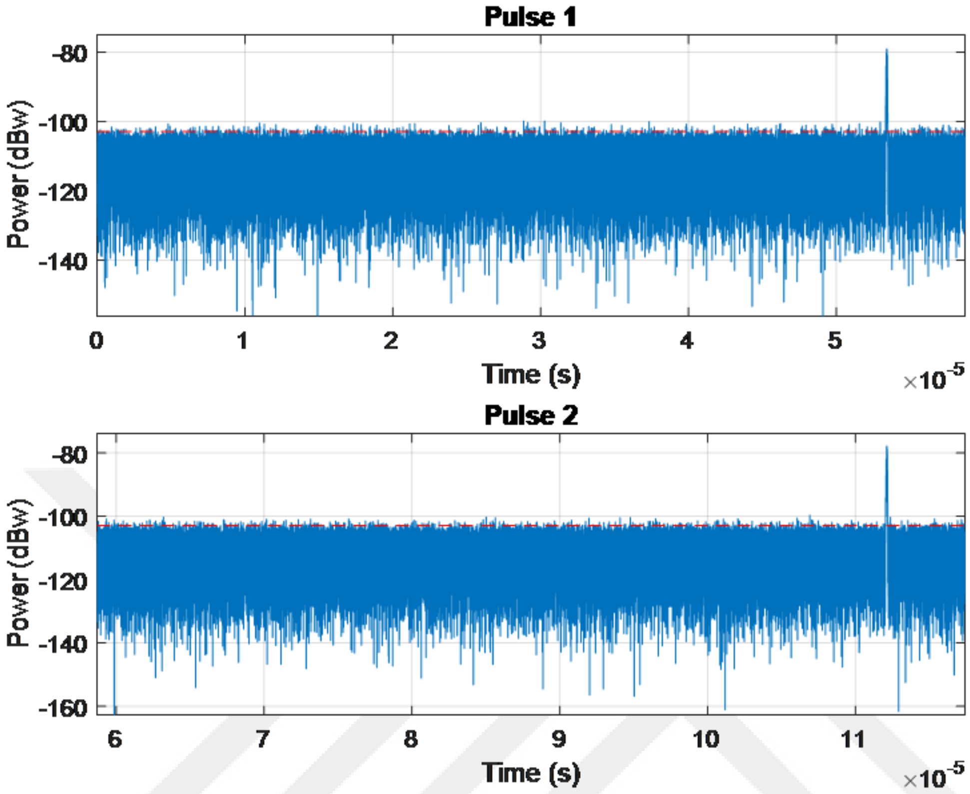

Figure 6.52 : The first two received pulses with applied threshold.

To enhance the signal-to-noise ratio (SNR), a matched filter was applied to the received pulses. This filter convolves the received signal with a time-reversed, conjugated copy of the transmitted waveform, improving the detection threshold to -60 dBW. The results of the matched filter are shown in Figure 6.53.

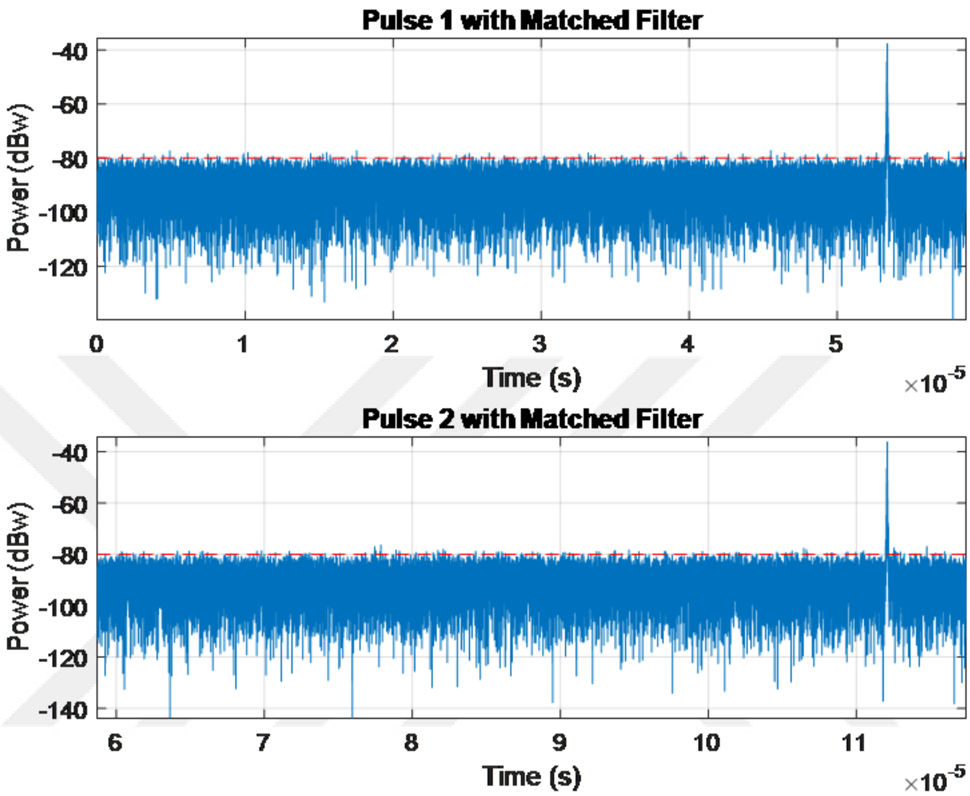

Figure 6.53 : Application of matched filter.

Since closer range bins produce stronger returns, range normalization was applied to equalize the signal strength across all ranges. The results of this normalization are shown in Figure 6.54.

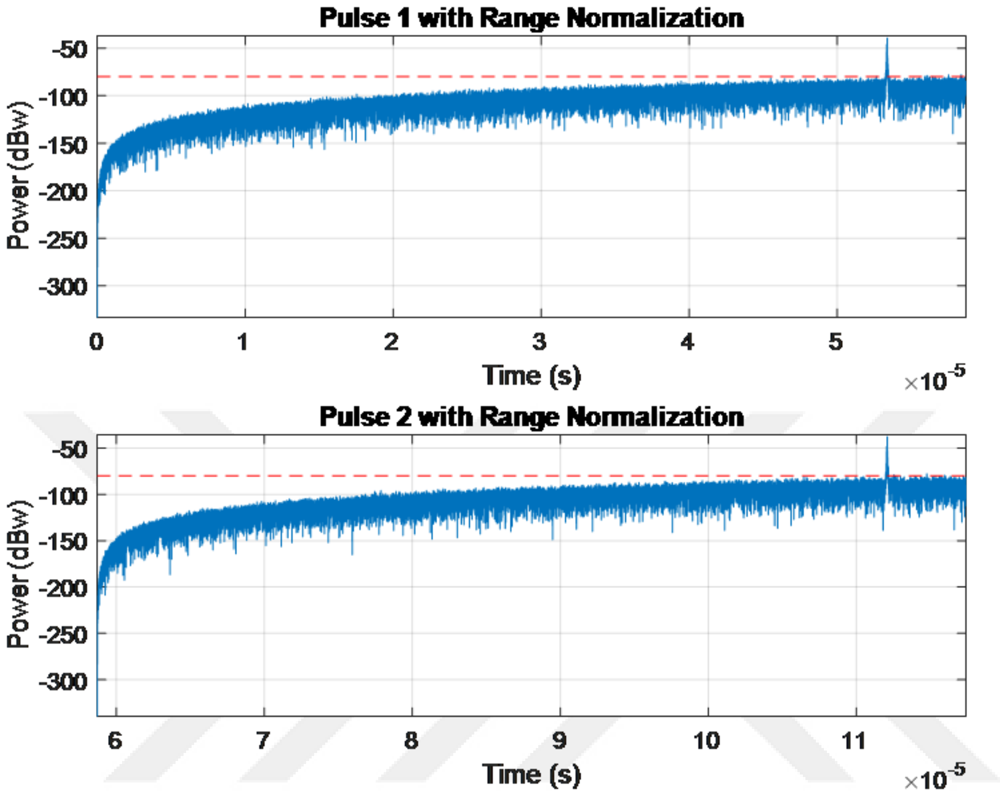

Figure 6.54 : Range normalization.

After normalization, coherent integration was applied to the received pulses to further enhance the SNR. The results of this integration are shown in Figure 6.55.

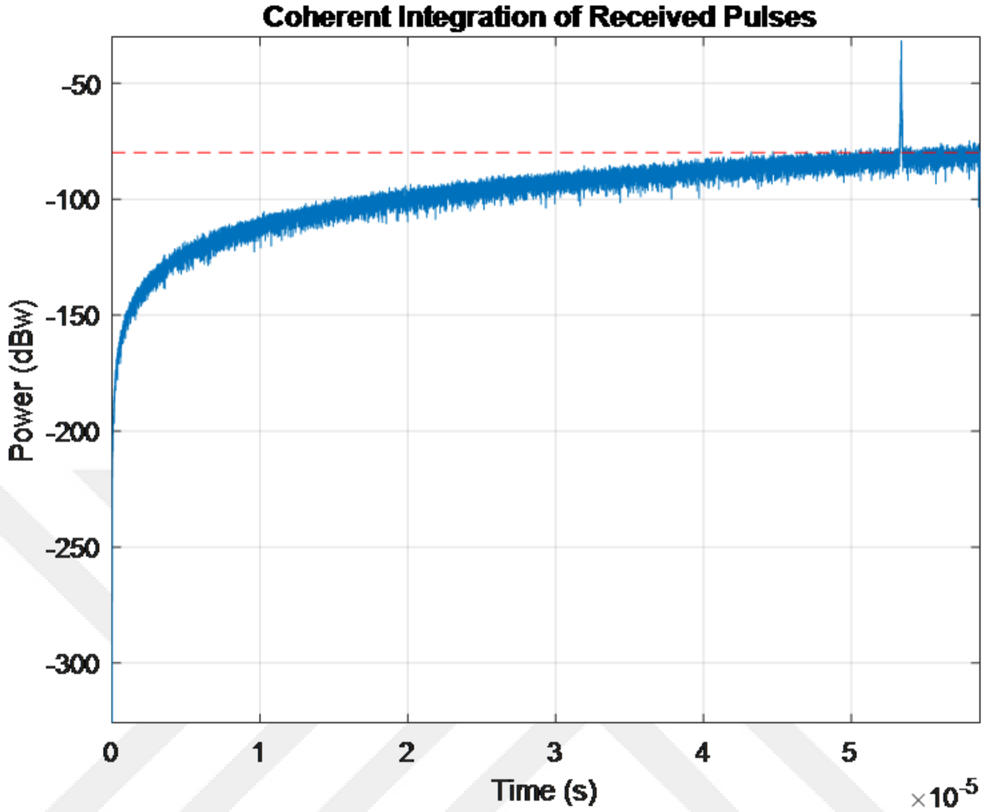

Figure 6.55 : Coherent integration of received pulses.

A High-Resolution Range Profile (HRRP), generated within a predefined range window using the integration result, is presented in Figure 6.56. Based on the location of the largest peak in the range bins, the target's range was estimated to be 8000 m, closely matching the actual range of 7998 m. The estimated physical size of the target is approximately 23.75 m, which aligns closely with the actual size of 25.86 m, considering the 1-meter range resolution.

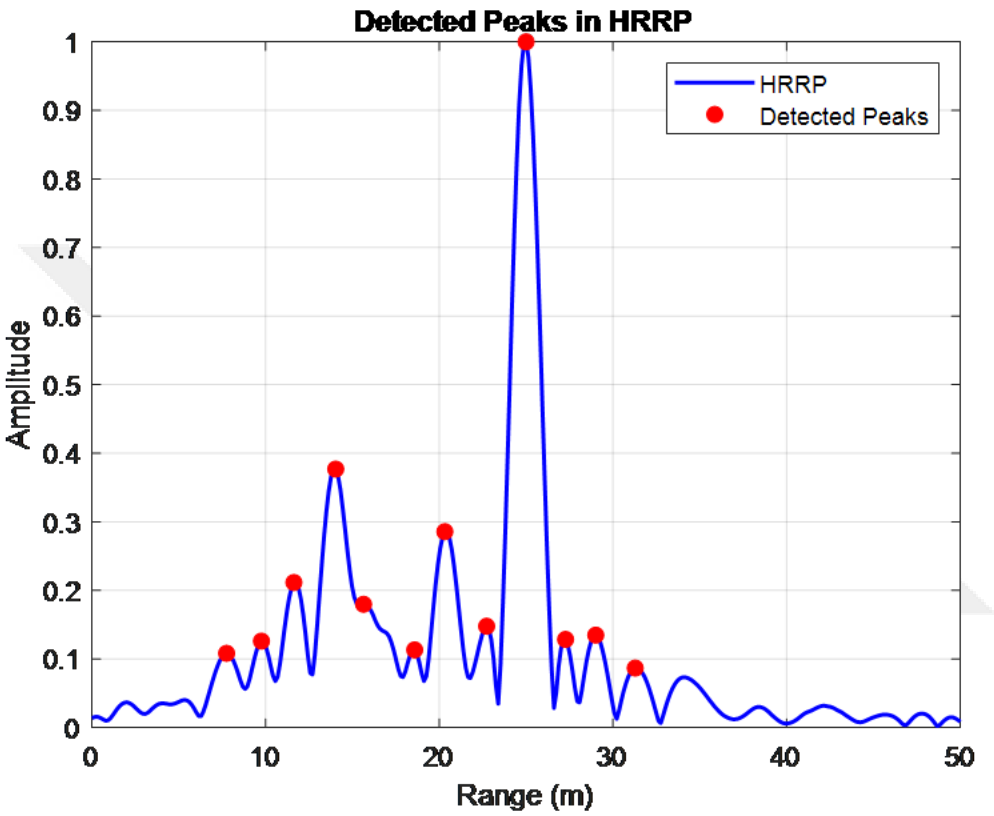

Figure 6.56 : High resolution range profile of the target.

6.3 Chengdu J-20

The Chengdu J-20 Aircraft, depicted in Figure 6.57, is characterized by its physical dimensions, including overall size, surface area, and the range of triangle areas used in the mesh. The detailed properties of the structure are listed in Table 6.5.

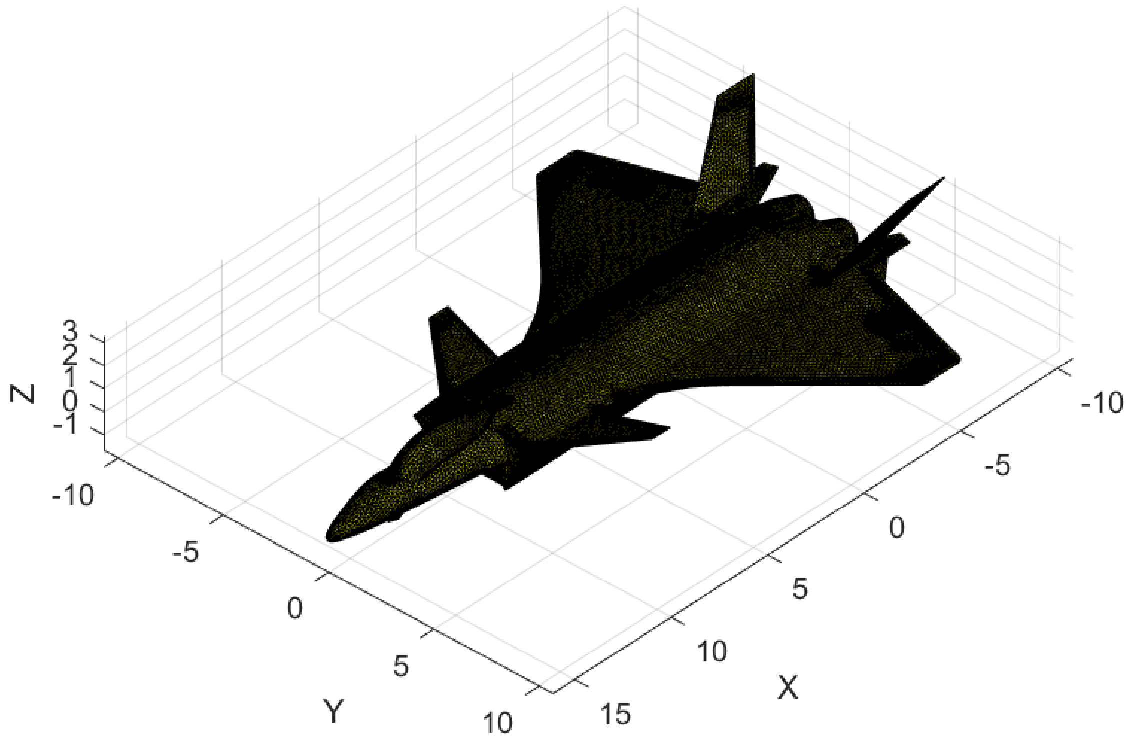

Figure 6.57 : Chengdu J-20 mesh

Table 6.5 : Chengdu J-20 model properties.

Parameter	**Value**
Model name	CHENGDU J-20 Aircraft
Number of triangles	71497
Number of points	34937
X Size	27.0111 m
Y Size	18.4174 m
Z Size	27.0111 m
Total area	555.1333 m^2
Max triangle area	0.01858 m^2
Min triangle area	$2.34535e-06 \times 10^{-5}$ m^2

Two distinct series of analyses were conducted to comprehensively evaluate the electromagnetic response of the Chengdu J-20 aircraft in 4 GHz. The first series maintained a constant azimuth angle θ at 90°, while varying the elevation angle ϕ from 0° to 180° in increments of 10°. Corresponding angles that are scanned are shown in Figure 6.58.

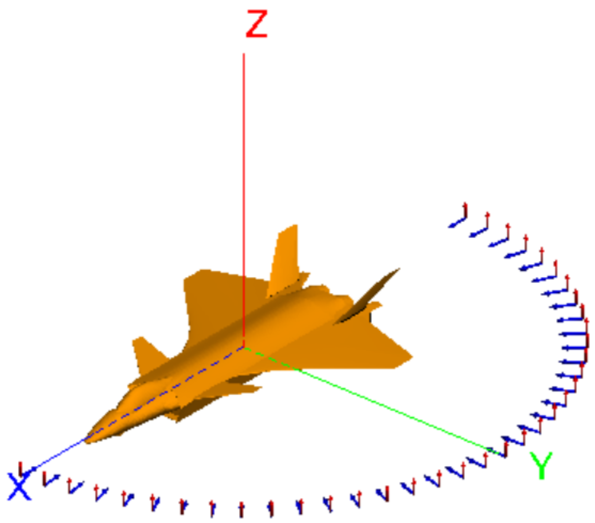

Figure 6.58 : ϕ=0°-180°, θ=90°.

The comparison of results of this analysis with FEKO are shown in Figure 6.59 for HH polarization and Figure 6.60 for VV polarization.

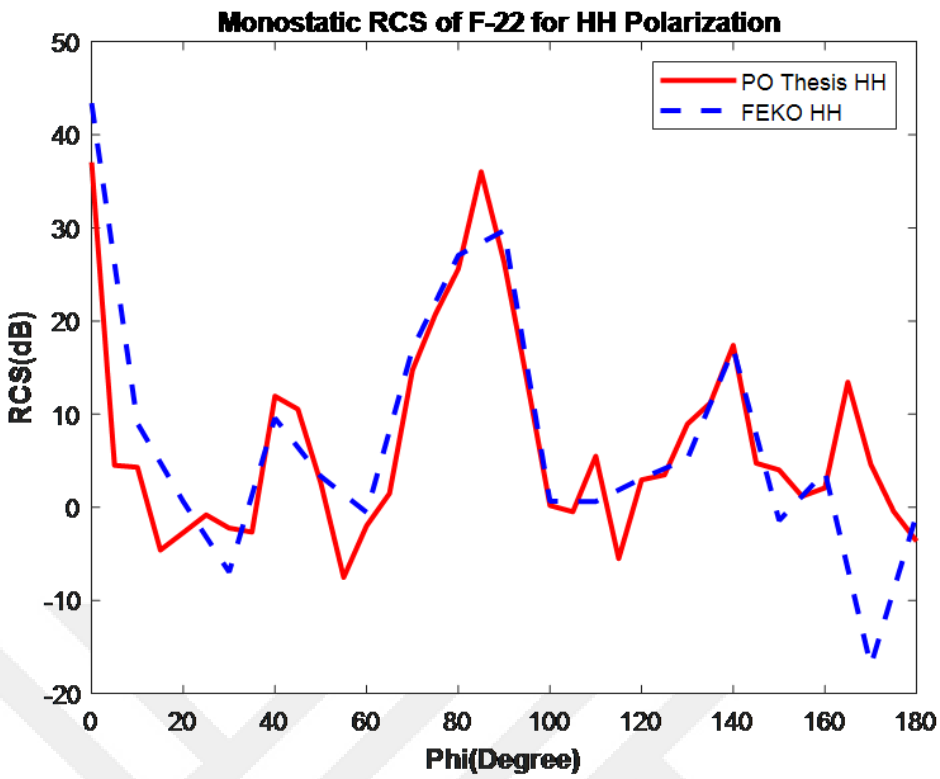

Figure 6.59 : Monostatic RCS of Chengdu J-20 for VV polarization at different ϕ angles.

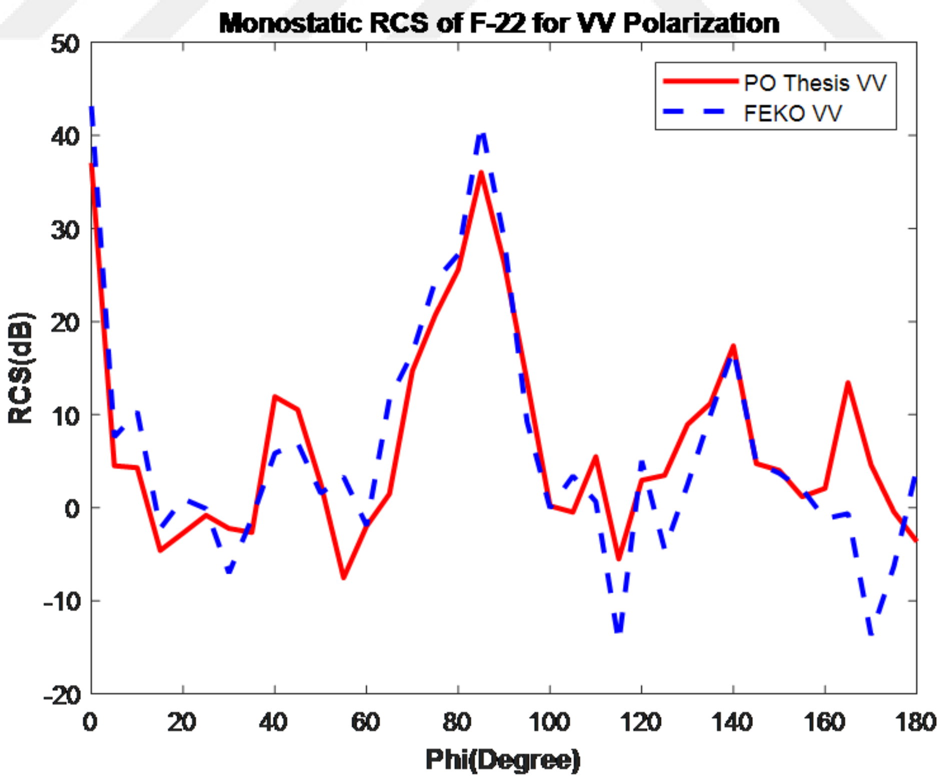

Figure 6.60 : Monostatic RCS of Chengdu J-20 for VV polarization at different ϕ angles.

The second series of analyses kept the *phi* fixed at 90° and varied the *theta*) in a similar manner from 0° to 180°. Corresponding angles that are scanned are shown in Figure 6.61.

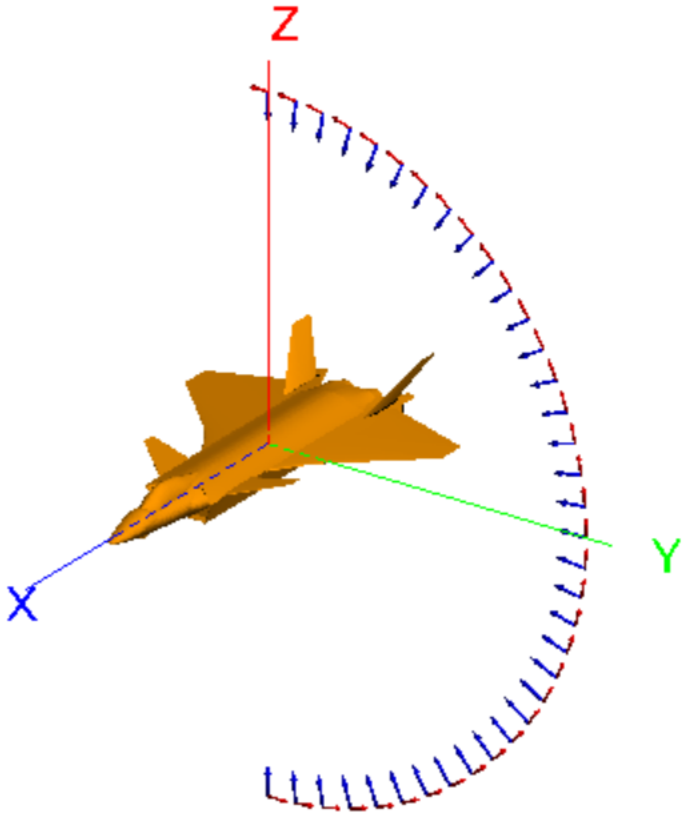

Figure 6.61 : ϕ=90°, θ=0° − 180°.

The comparison of results are shown in Figure 6.62 for HH polarization and Figure 6.63 for VV polarization. As it can be seen, results have great agreement.

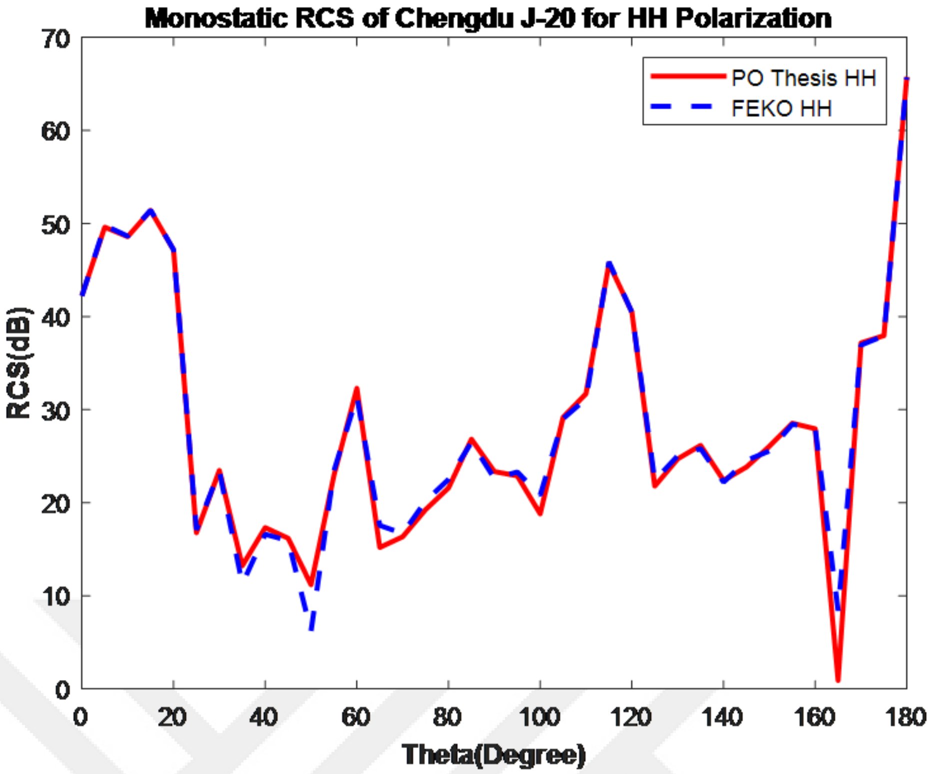

Figure 6.62 : Monostatic RCS of Chengdu J-20 for HH polarization at different θ angles.

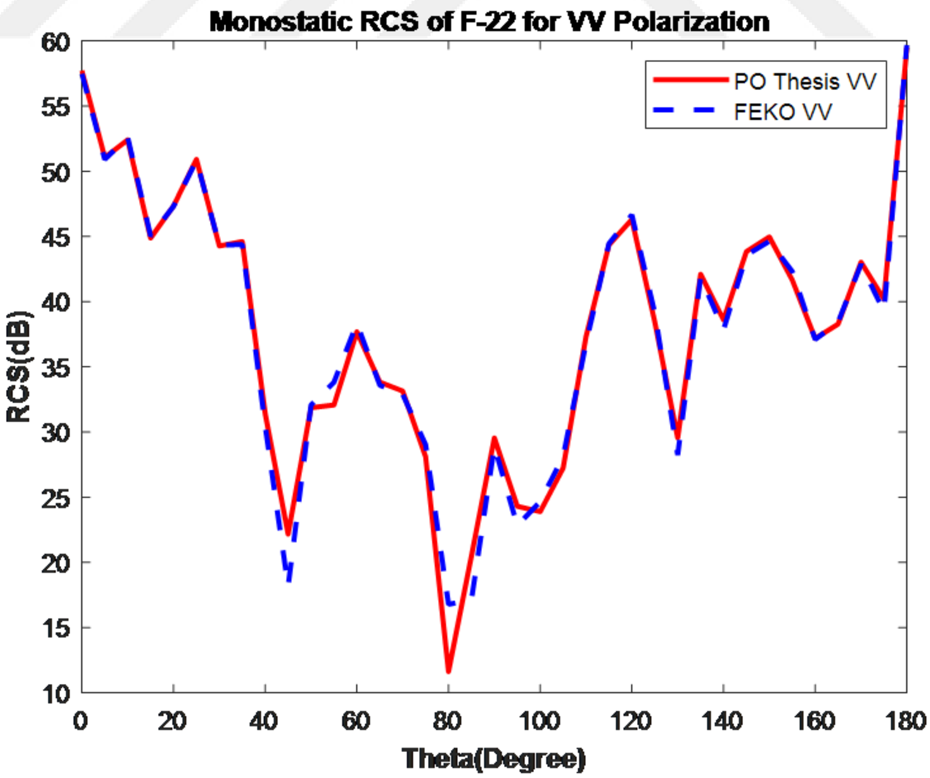

Figure 6.63 : Monostatic RCS of Chengdu J-20 for VV polarization at different θ angles.

To apply radar signal processing, target can be analysed from one point of view For the range profile analysis, θ =90° and ϕ =90° can be chosen. From this point of view, the surface currents are showed in the Figure 6.64.

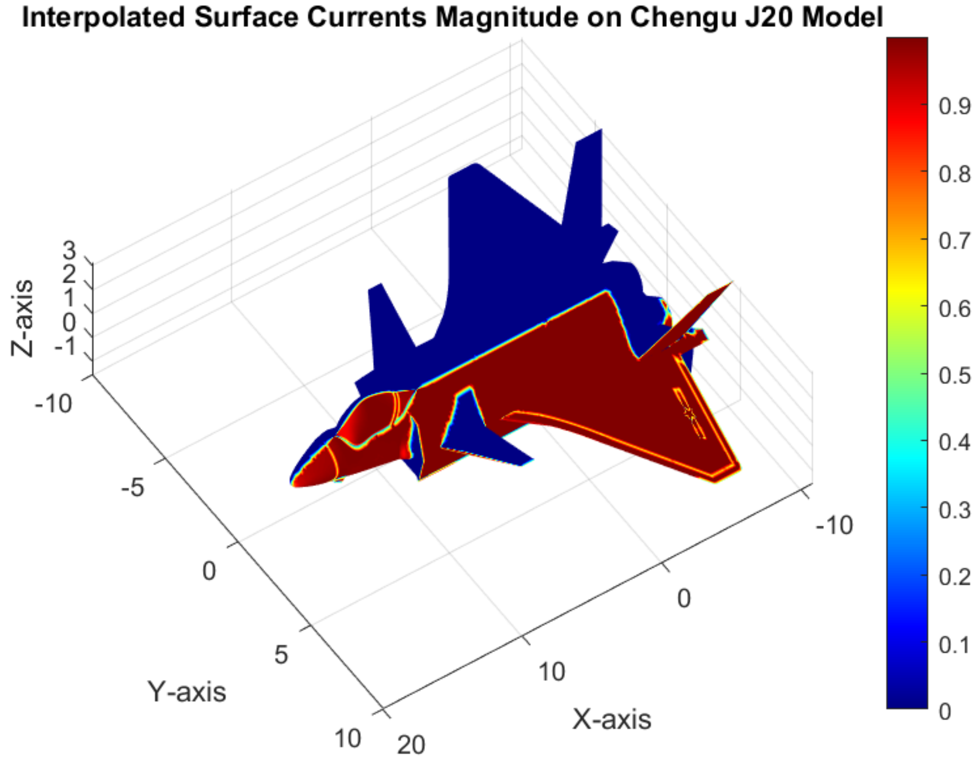

Figure 6.64 : Surface currents of Chengdu J-20.

Five radar pulses are generated as the previous analysis, and transmitted throug the target.Using the rcs values of the target mesh elements that are illuminated while looking from the relevant point of view, reflected and received signals are obtained and shown in the Figure 6.65. For the detailed examination, only the first pulses are also given in the Figure 6.66, which depict the delay at the reflected signal and attenuation at the received signal.

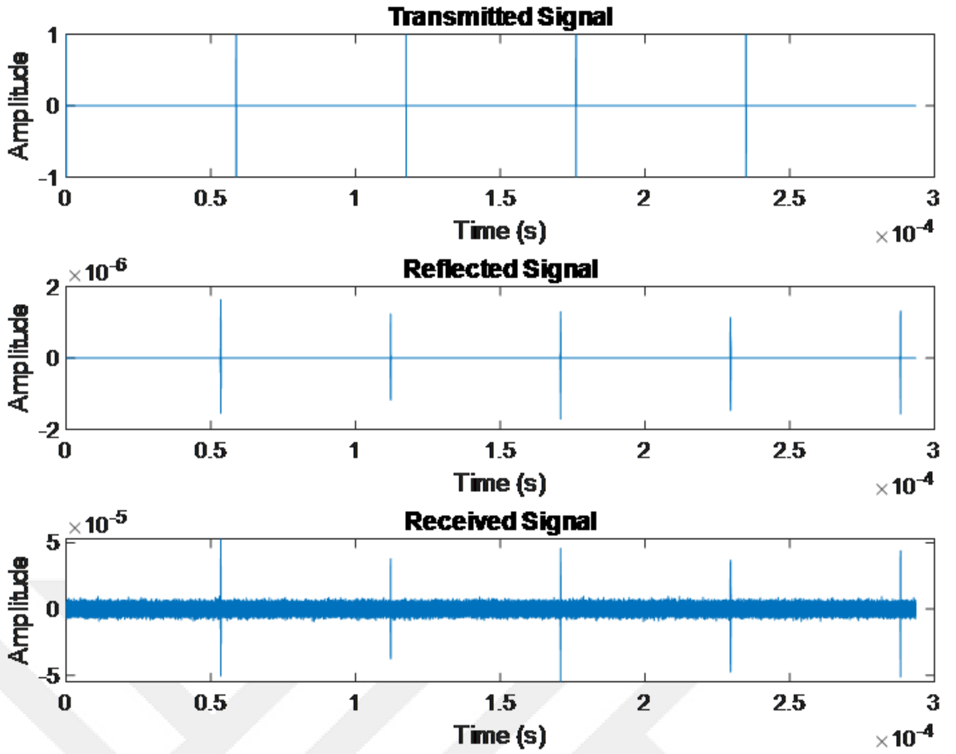

Figure 6.65 : Transmitted, reflected and received pulses.

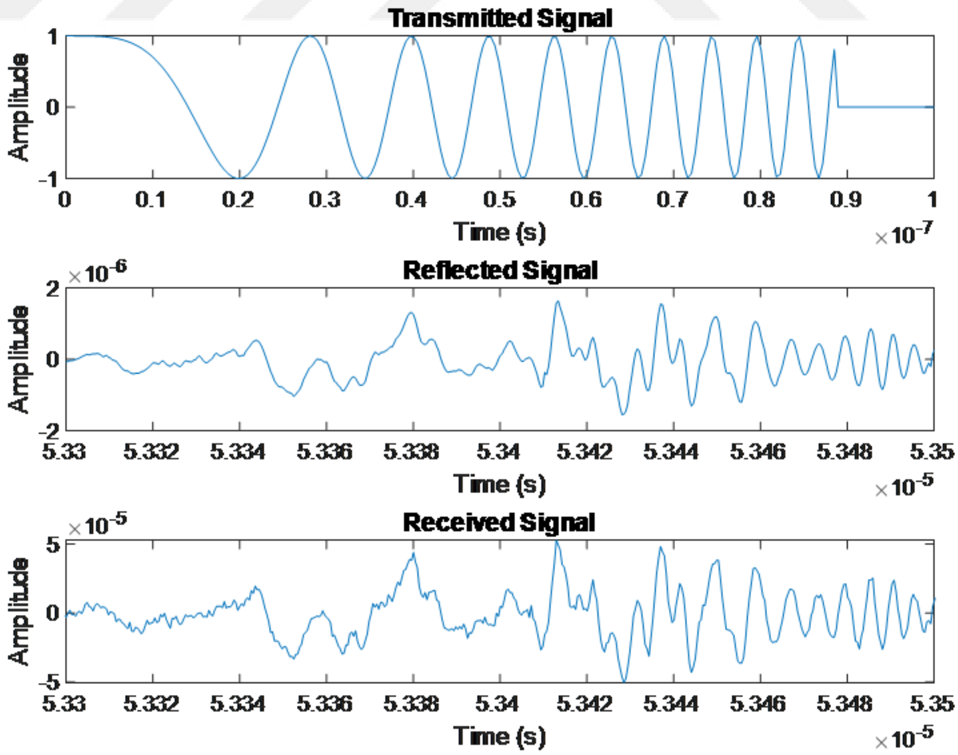

Figure 6.66 : First pulses that are transmitted, reflected and received.

First two pulses at the detector are given in the Figure 6.67, as it can be seen only the part that is higher than threshold is captured and transmitted through the receiver.

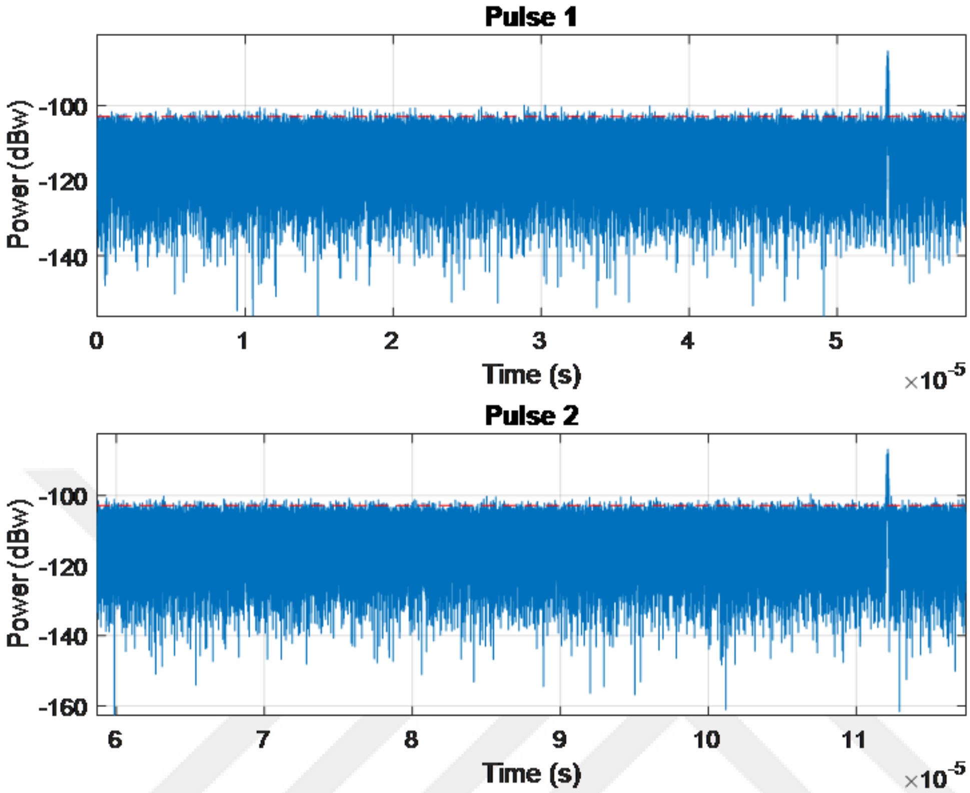

Figure 6.67 : The first two received pulses with applied threshold.

After the pulses are received, matched filter is applied and threshold is calculated as -80 dbW. Matched filter responses of this pulses are shown in the Figure 6.68. As a result of this process, the noise components are successfully eliminated.

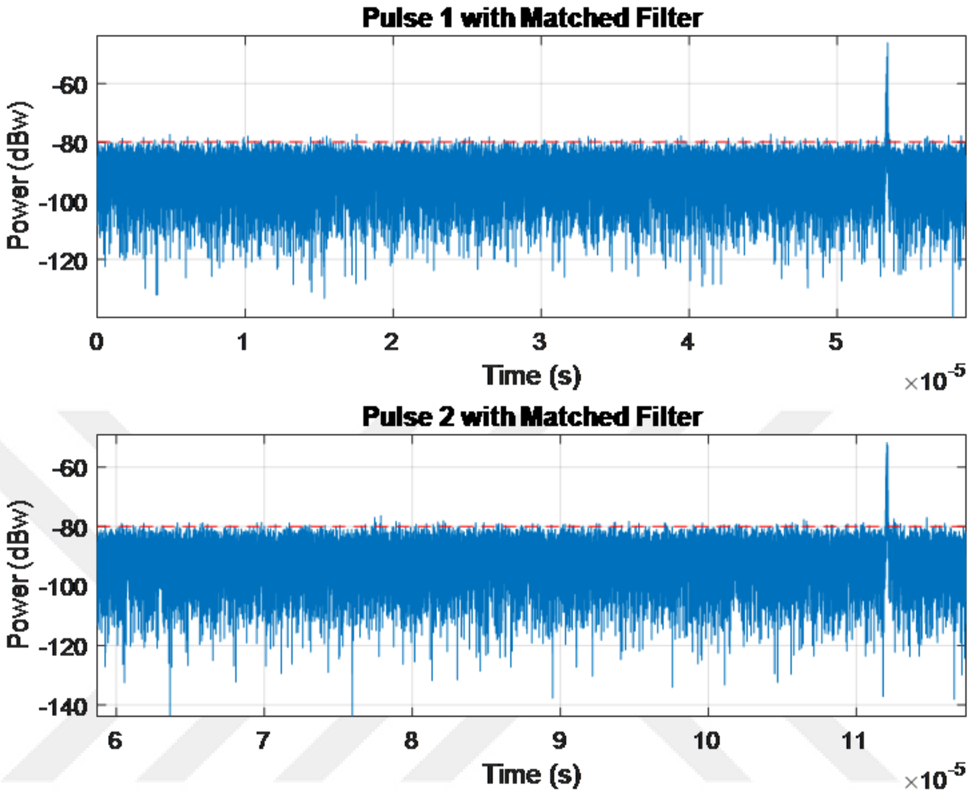

Figure 6.68 : Application of matched filter.

For eliminating the effects of the different ranges, range normalization process is taken. The final form of the signal graphs are given in the Figure 6.69 for first two pulses.

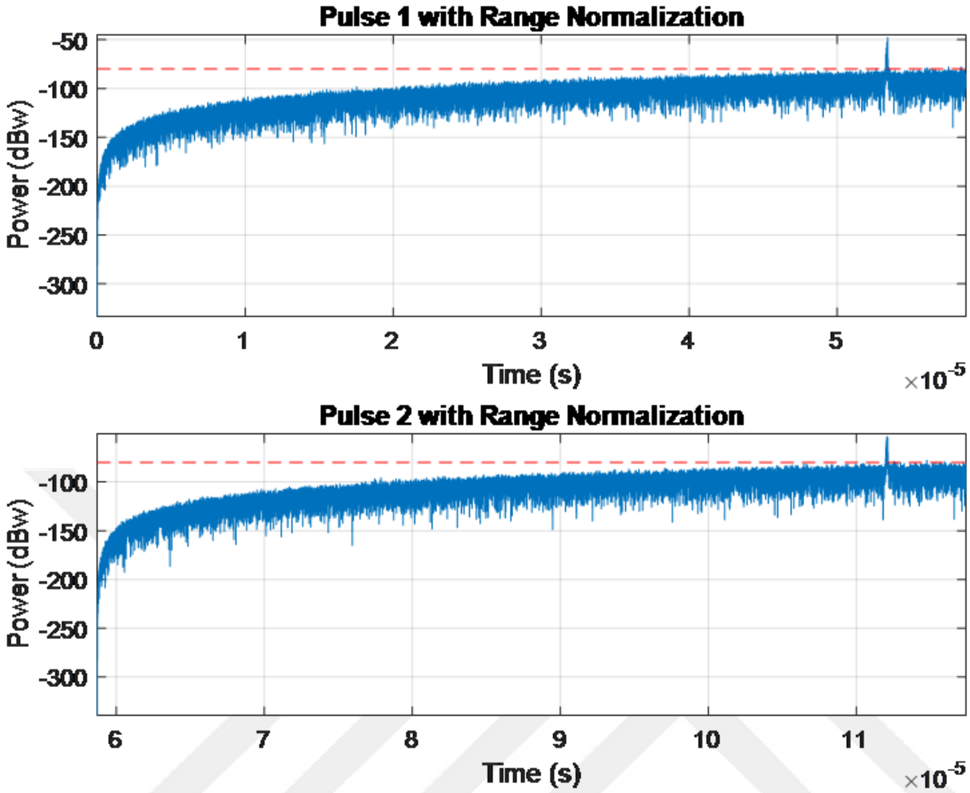

Figure 6.69 : Range normalization.

The coherent integration of the pulses are calculated to gather all responses and create a range profile data. The results of integration are shown in the Figure 6.70.

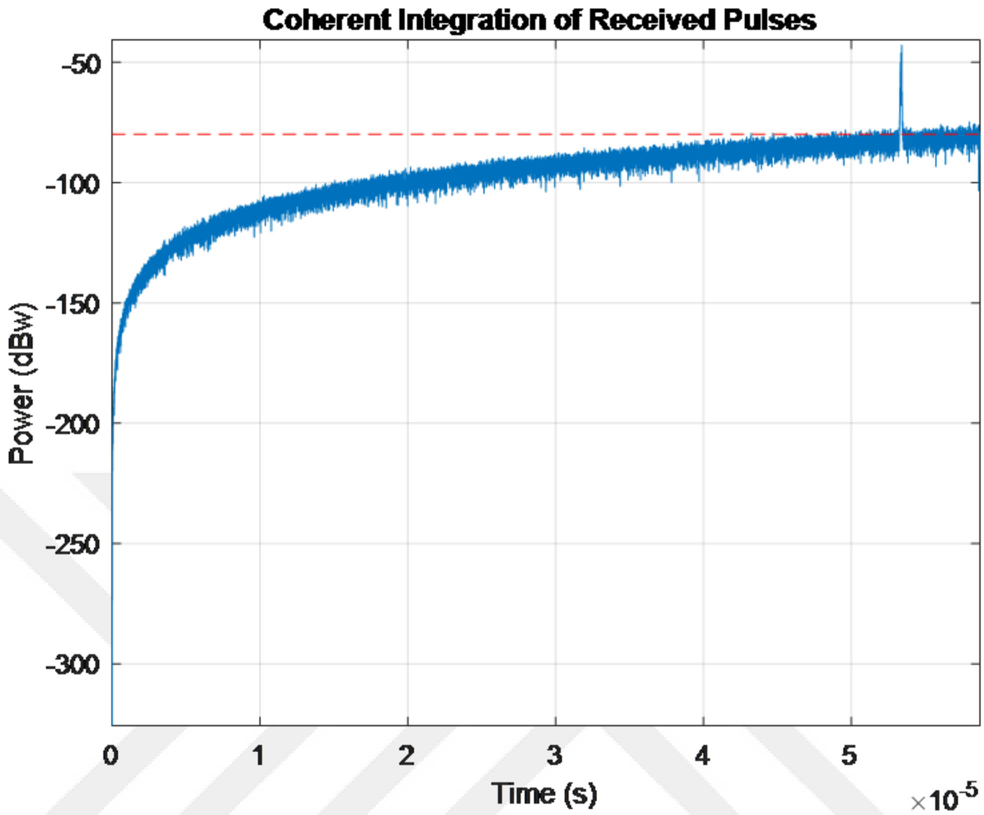

Figure 6.70 : Coherent integration of he pulses.

Range of the target is estimated based on the location of the largest peak in the range bins as shown in the Figure 6.71. The estimated target range is 7999.33 meters and real target range is 8001 meters.

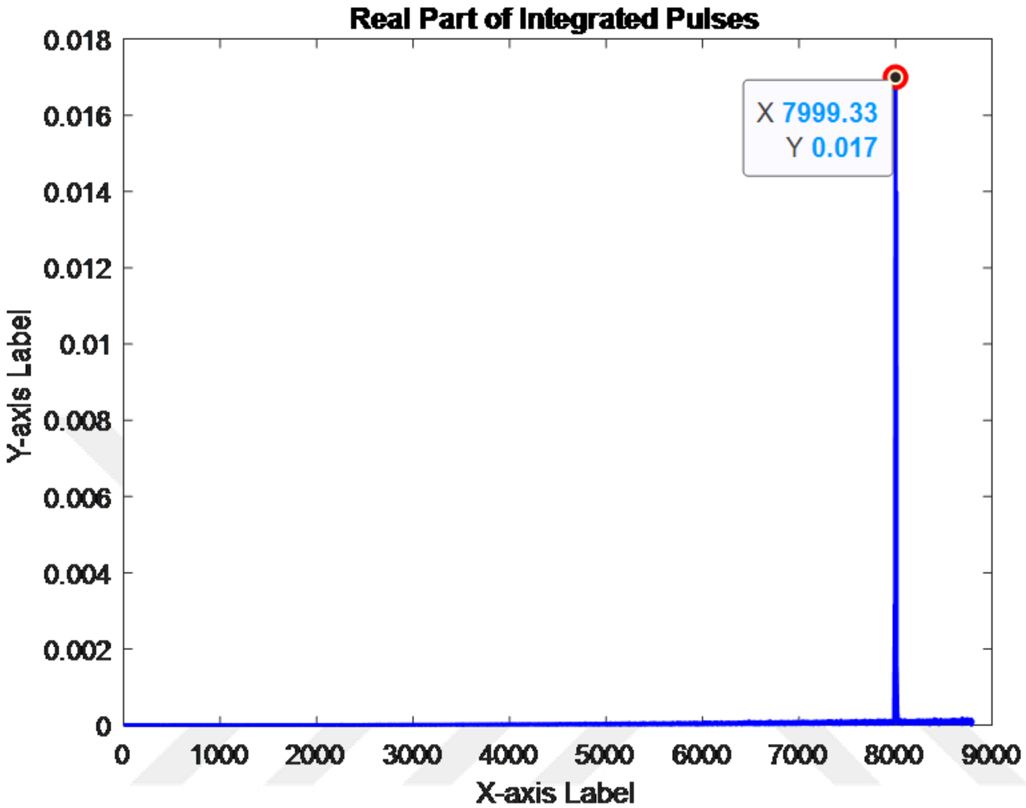

Figure 6.71 : Range estimation of Chengdu J-20.

The detected peaks are given in the Figure 6.72. The calculated physical size is approximately 17.246 meters. Which is a good result comparing with the actual size, 18.4174 meters, and considering 1 meters range resolution.

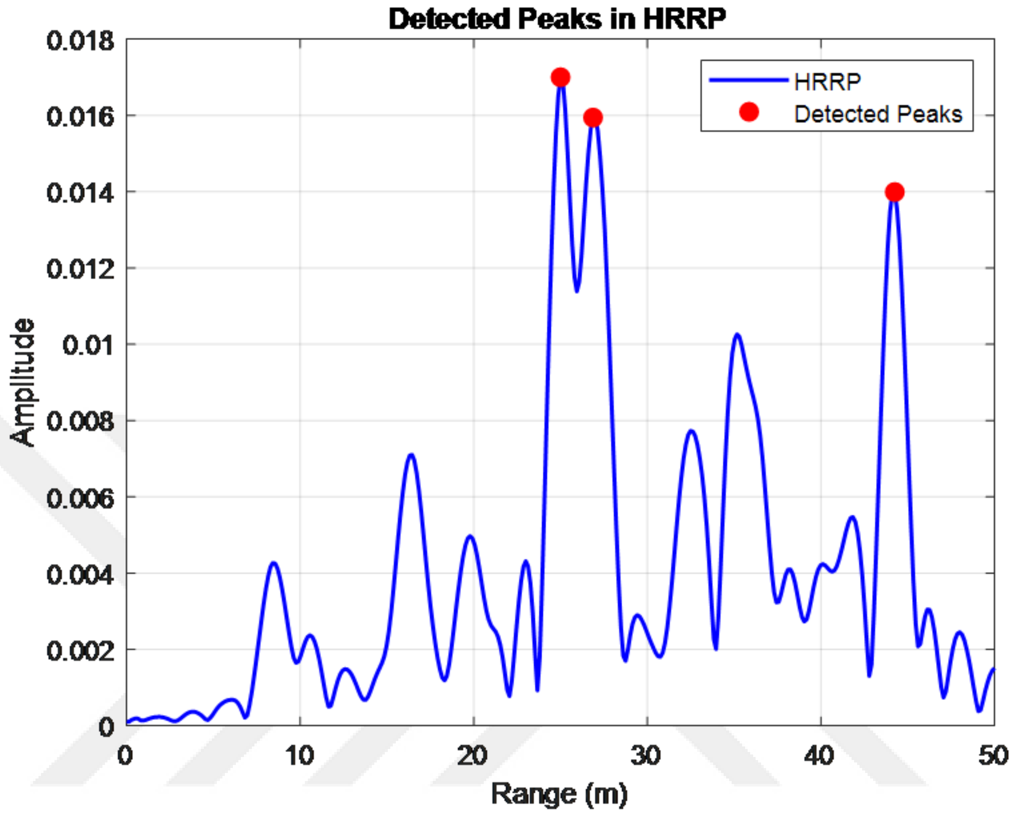

Figure 6.72 : High resolution range profile of the target.

7. CONCLUCION

This thesis presented a detailed exploration of Radar Range Profile calculations using Time Domain Processing integrated with the Physical Optics (PO) method. The study addressed the limitations of traditional RCS (Radar Cross Section) analysis by introducing advanced computational methods to model electromagnetic wave interactions with complex targets. Through the development of refined algorithms for mesh generation, shadowing analysis, and signal processing, the research achieved significant improvements in accuracy and computational efficiency. Simulations on real-world examples, including missile and aircraft geometries, validated the methodology's robustness in capturing intricate radar signatures. The integration of matched filtering and time-varying gain adjustments further enhanced the detection capabilities, ensuring consistent performance across varying ranges. The findings demonstrated the PO method's capability to efficiently and accurately predict RCS for high-frequency scenarios and complex geometries. The use of time-domain techniques allowed for detailed modeling of transient electromagnetic phenomena, addressing scenarios where traditional frequency-domain approaches are insufficient. This comprehensive approach revealed essential insights into the scattering, reflection, and shadowing behavior of targets under various conditions. Future work could build on this foundation by optimizing the computational algorithms, particularly for mesh refinement and shadowing calculations, to further enhance efficiency and scalability. Incorporating detailed material properties, such as anisotropic or frequency dependent characteristics, would provide a more comprehensive understanding of RCS. Experimental validation, through scale model testing or comparisons with real radar data, would help confirm the accuracy of the simulations in practical applications. Extending the methodology to civilian and space applications, such as satellite visibility studies or autonomous vehicle radar systems, could broaden its impact. Additionally, integrating machine learning algorithms could enable predictive modeling and uncover patterns in large datasets.

REFERENCES

[1] **Knott, E.F., Schaeffer, J.F. and Tulley, M.T.** (2004). *Radar cross section*, SciTech Publishing.

[2] **Chatzigeorgiadis, F.** (2006). *Development of code for a physical optics radar cross section prediction and analysis application*, Monterey, CA; Naval Postgraduate School.

[3] **Yamada, Y., Michishita, N. and Nguyen, Q.D.** (2014). Calculation and measurement methods for RCS of a scale model airplane, *2014 International Conference on Advanced Technologies for Communications (ATC 2014)*, IEEE, pp.69–72.

[4] **Ufimtsev, P.Y.** (2006). Improved physical theory of diffraction: Removal of the grazing singularity, *IEEE transactions on antennas and propagation*, *54*(10), 2698–2702.

[5] **Gorji, A.B., Janalizadeh, R.C. and Zakeri, B.** (2013). RCS computation of a relatively small complex structure by asymptotic analysis, *2013 International Symposium on Electromagnetic Theory*, IEEE, pp.1066–1069.

[6] **Deng, X., Gu, C., Yuan, J., Li, Z. and Zhou, Y.** (2010). Electromagnetic scattering by arbitrarily shaped PEC targets coated with magnetic anisotropic media using equivalent dipole-moment method, *2010 International Symposium on Signals, Systems and Electronics*, volume 2, IEEE, pp.1–4.

[7] **Liu, Z., Wang, J., Wang, M.s., Lu, Y., Chen, Y.** *et al.* (2019). Finite element method and charge coupling method for distortion field of AC transmission line, *2019 IEEE Sustainable Power and Energy Conference (iSPEC)*, IEEE, pp.1049–1053.

[8] **Balanis, C.A.** (2012). *Advanced engineering electromagnetics*, John Wiley & Sons.

[9] **Moreira, F.J. and Prata, A.** (1994). A self-checking predictor-corrector algorithm for efficient evaluation of reflector antenna radiation integrals, *IEEE Transactions on Antennas and Propagation*, *42*(2), 246–254.

[10] **Ji, J. and Wu, H.** (2015). Shadowing algorithm of facets in physical optics (PO) based on determinant, *Optik*, *126*(14), 1366–1368.

[11] **Stimson, G.W.** (1998). *Introduction to airborne radar*, Institution of Engineering and Technology.

[12] **Won, Y.S.**, **Kim, C.H. and Lee, S.G.** (2015). Range resolution improvement of a 24 GHz ISM band pulse radar—A feasibility study, *IEEE sensors journal*, *15*(12), 7142–7149.

[13] **Mahafza, B.R.** (2005). *Radar systems analysis and design using MATLAB*, Chapman and Hall/CRC.

[14] **Khalid, S.S. and Abrar, S.** (2013). Area under the ROC curve of enhanced energy detector, *2013 11th International Conference on Frontiers of Information Technology*, IEEE, pp.131–135.

[15] **Shnidman, D.** (2002). Determination of required SNR values [radar detection], *IEEE Transactions on Aerospace and Electronic Systems*, *38*(3), 1059–1064.

[16] **Orduyılmaz, A.**, **Kara, G.**, **Serin, M.**, **Yıldırım, A.**, **Gürbüz, A.C. and Efe, M.** (2015). Real-time pulse compression radar waveform generation and digital matched filtering, *2015 IEEE Radar Conference (RadarCon)*, IEEE, pp.0426–0431.

[17] **Wang, L.**, **Bao, X.**, **Liu, C.**, **Yan, W.**, **Jiang, B.**, **Wang, Y.**, **Si, L.**, **Schreurs, D.**, **Shi, Z. and Zhang, A.** (2024). Highly Compact Time-Domain Borehole Radar With Time-Varying Gain Equivalent Sampling, *IEEE Transactions on Microwave Theory and Techniques*.

[18] **Tien, V.V.**, **Hop, T.V.**, **Nhu, N.**, **Hoang, D.X. and Van Loi, N.** (2019). A staggered PRF coherent integration for resolving range-Doppler ambiguity in pulse-Doppler radar, *2019 20th International Radar Symposium (IRS)*, IEEE, pp.1–7.

[19] **Liu, Y.**, **Wang, J.**, **Cui, D. and Peng, S.** (2023). High-Resolution Range Profile Recognition of Midcourse Ballistic Targets Based on AMTrans, *2023 International Conference on Image Processing, Computer Vision and Machine Learning (ICICML)*, IEEE, pp.1–5.

CURRICULUM VITAE

Ece YAZAREL:

EDUCATION:

- **B.Sc.:** 2019, Istanbul Technical University, Electronic and Communication Engineering

PROFESSIONAL EXPERIENCE AND REWARDS:

- 2021-2022 Hardware Design Engineer at Arçelik
- 2022-2024 Electromagnetic Design Engineer at Turkish Aerospace

PUBLICATIONS, PRESENTATIONS AND PATENTS ON THE THESIS:

- **Yazarel E.**, Paker S. (2024). Time Domain Physical Optics for RCS Calculation. *3rd International Graduate Symposium - IGRS'24*, April 23 - May 1, 2024 Istanbul, Turkey. (Presentation Instance)